Technische Universität München

TUM School of Engineering and Design

Centralized Control of Grid-Connected High-Speed Switched Reluctance Motor Drive System

Ying Tang

Vollständiger Abdruck der von der TUM School of Engineering and Design der Technischen Universität München zur Erlangung eines

Doktors der Ingenieurwissenschaften (Dr.-Ing.)

genehmigten Dissertation.

Vorsitz:　　　　　　　Prof. Dr. Thomas Hamacher
Prüfende der Dissertation:
　　　　　　　1. Prof. Dr.-Ing. Dr. h.c. Ralph Kennel
　　　　　　　2. Prof. Dr.-Ing. Fengxiang Wang

Die Dissertation wurde am 13.07.2023 bei der Technischen Universität München eingereicht und durch die TUM School of Engineering and Design am 06.03.2024 angenommen.

Acknowledgment

This dissertation would not have been possible without the help of many people in many ways. It is also the result of encounters with people who shaped or, in some cases, changed the course of events in my career.

I would like to thank Prof. Dr.-Ing. Ralph Kennel for accepting me as a Ph.D. candidate at the Institute for Electrical Drive Systems and Power Electronics at Technische Universität München in 2017, otherwise this dissertation would not come true. I appreciate the freedom entrusted by him and his support throughout my doctoral period. It was a great privilege to research under his guidance.

I would like to express my special and deep gratitude to my mentor Prof. Dr.-Ing. Fengxiang Wang for recommending me to the institute. More than that, he supports me with all the best he can in technical and living aspects during my doctoral period. Without his support, my testbench could not be constructed and my research could not go on smoothly. His dynamism, vision, and motivation have deeply inspired me. It was a great honor to research under his guidance.

It is my great pleasure to work with my colleagues at EAL. Mr. Wei Tian, Mr. Xiaonan Gao, Mr. Qing Chen, and Mr. Haotian Xie. They support me in both my academic research and daily life in Germany. They offer their help whenever I need it. They are not just colleagues but very good friends of mine, with whom I spent many memorable moments in Munich. Thanks again for their generous help and care, they have made my doctoral period an invaluable experience. Also, many thanks to Anja Inzenhofer, Dr. -Ing. Julien Cordier, and Mr. Wolfgang Ebert for their kind help in the institute.

Last but also the most sincere gratitude goes to my dearest family. My parents and grandparents give me their love, heartwarming encouragement, and continuous support throughout my life, which grant me the courage to face challenges. In particular, I would like to express my deep thanks to my husband Yingjie He for his strong support and care, and his belief in me has kept my spirits and motivation high.

Germany, in Jan. 2023
Ying Tang

Abstract

High power factor offers significant advantages such as reducing required power capacity, energy losses, and system manufacturing cost. This dissertation aims to achieve the grid-side power factor correction while maintaining a satisfying motor regulation for grid-connected high-speed switched reluctance motor (SRM) drive system. In order to improve the regulation performance of SRM, a 4-level converter topology with double-voltage demagnetization mode is proposed to reduce the tailing time of demagnetization current, thereby increasing the utilization of inductance increasing region. Moreover, a centralized drive system that treats the front-end voltage-sourced rectifier (VSR) and the back-end SRM as a whole is proposed. A direct power connection between the VSR and SRM is built so that the whole system can be controlled by manipulating the instantaneous power flow. Without causing additional computational burden, the asymmetric space vector pulse width modulation is introduced for switching loss reduction. Although VSR and SRM can be regulated by one control strategy in the above centralized control system, the outer speed proportional-integral controller is still required to generate power reference for inner controller to track. To remove this cascade control structure, a cascade-free model predictive direct power control strategy that directly regulates the speed and power flows within a newly-defined cost function is proposed. By evaluating the cost function, the vector, which not only will generate a motor speed closer to the reference at the next instant but will generate an active power capable of further reducing that speed error for the future instant, is selected. Besides, the robustness against parameter mismatches has been considered for this model-based control strategy, so the Kalman filter is added to improve the overall system performance. Consequently, satisfying SRM regulation performance, grid-side power factor correction, and current harmonics restraint can be realized simultaneously in the proposed systems.

Kurzfassung

Hoher Leistungsfaktor bietet signifikante Vorteile wie die Reduzierung der erforderlichen Leistungskapazität, Energieverluste und Systemherstellungskosten. Ziel dieser Dissertation ist es, die netzseitige Leistungsfaktorkorrektur zu erreichen und gleichzeitig eine zufriedenstellende Motorregelung für netzgekoppelte Hochgeschwindigkeits-Antriebssysteme mit Geschaltete Reluktanzmaschine (SRM) aufrechtzuerhalten. Um die Regelleistung des SRM zu verbessern, wird eine 4-Stufen-Wandlertopologie mit Doppelspannungs-Entmagnetisierungsmodus vorgeschlagen. Dadurch reduziert sich die Dauer der Stromabnahme des Entmagnetisierungsstroms und weiterhin erhöht sich die Ausnutzung des induktivitätserhöhenden Bereichs. Darüber hinaus wird ein zentralisiertes Antriebssystem vorgeschlagen, das das aktive Frontend und das Backend-SRM als Einheit behandelt. Eine direkte Leistungsverbindung zwischen dem AFE und dem SRM wird aufgebaut, so dass das gesamte System durch Manipulieren des momentanen Leistungsflusses gesteuert werden kann. Ohne eine Rechenlast zu verursachen, wird der asymmetrische Raumzeigermodulation zur Reduzierung der Schaltverluste eingeführt. Obwohl das AFE und SRM durch eine Steuerstrategie in dem obigen zentralisierten Steuersystem geregelt werden können, ist ein äußerer Proportional-Integral-Regler für die Geschwindigkeitsregelung immer noch erforderlich, um eine Sollleistung zu erzeugen, damit der innere Regler nachgeführt werden kann. Um diese Kaskadenregelungsstruktur zu beseitigen, wird eine kaskadenfreie modellprädiktive Direktleistungsregelungsstrategie vorgeschlagen, die die Geschwindigkeit und die Leistungsflüsse innerhalb einer neu definierten Kostenfunktion direkt regelt. Durch Auswertung der Kostenfunktion wird ein Vektor ausgewählt, der nicht nur im nächsten Moment eine Motordrehzahl näher an der Referenz erzeugt, sondern auch eine Wirkleistung erzeugt, die in der Lage ist, den Drehzahlfehler für den zukünftigen Zeitpunkt weiter zu reduzieren. Außerdem wurde die Robustheit gegenüber Nichtübereinstimmung der Parameter für diese modellbasierte Steuerstrategie berücksichtigt, sodass ein Kalman-Filter hinzugefügt wird, um die Leistung des gesamten Systems zu verbessern. Folglich können durch das vorgeschlagene System gleichzeitig eine zufriedenstellende Motorregelung, netzseitige Leistungsfaktorkorrektur und Einschränkung von Stromharmonischen realisiert werden.

Contents

CHAPTER 1

Introduction

1.1 Electric motor types

Induction motor (IM) and permanent magnet synchronous motor (PMSM) dominate in the motor drive systems used in industrial, residential, commercial, and transportation applications. Fig. 1.1 shows the typical structure of these two motors and compares them with that of switched reluctance motor (SRM). All of these three motors have a stator, winding, and rotor, but SRM becomes prominent in terms of its simple structure [2, 3].

PMSM has been widely adopted due to its high power density and high efficiency [4, 5]. The permanent magnets (PMs) on rotor provide an independent source of magnetic flux, and by applying a careful design for the location and arrangement of the magnets, the output torque at higher speeds can even be improved by utilizing the reluctance torque, thereby achieving high torque density and high efficiency. As the speed increases, field weakening control should be applied to adjust the angle of stator current vector to counteract part of the magnetic field built by PM, which helps extend the speed range under the limited terminal voltage [6]. To keep a reliable operation, the PMs must have enough coercivity to make sure it can not be demagnetized during the field weakening.

When compared to PMSM, IM has lower construction cost because of the lack of PM. Die-casting of aluminum rotor bars is also a low-cost process. The self-starting capability is one of the main reasons why IM is widely used in industry. Both PMSM and SRM require a power converter, control algorithm, and position feedback or estimation, but three-phase IM can start from alternating current (AC) supply without a power converter, control algorithm, or position feedback. However, due to the induced currents on the rotor conductors, there are non-negligible rotor copper losses in the induction machine, especially for high-power applications, which brings challenges for cooling. For IM with die-casted aluminum rotor bars, the losses can be more significant, because of the low electrical conductivity of aluminum.

IM have dominated motor drive applications due to their low-cost manufacturing and self-starting capabilities [7]. However, with the increasing demand for higher efficiency, IM should
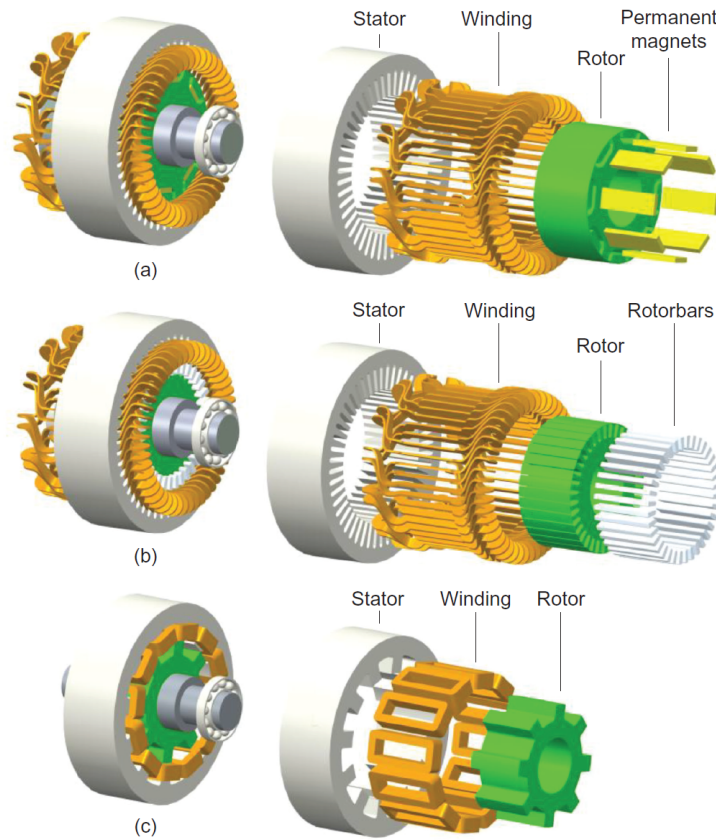
Figure 1.1: Typical structure of electric machine types [1]. (a) Interior PMSM. (b) IM. (c) SRM.

be designed with lower losses and they need to be operated with adjustable speed drives. These factors reduce its cost advantage. Today, PMSM has been used more and more frequently in various applications due to their lower losses and increased system efficiency through the use of adjustable speed drives. However, as demand increases, price fluctuations of rare earth materials, supply chain issues, and environmental concerns have become major issues for permanent magnet motors.

SRM has a simple, low-cost, and robust construction [8]. The stator is made of a salient pole laminated core with concentrated windings, while the rotor also has a salient pole structure, but without windings or permanent magnets, which makes SRM more suitable for running in high-speed conditions. The high-speed operation performance of PMSM is seriously limited by the rotor displacement and rotational stress. When the rotor is rotating at high speeds, centrifugal forces dominate and high stresses occur on the magnet slots and the bridges (the sections between the magnet slot and the air gap in rotor core). These parts have to be carefully designed so that they can handle the centrifugal forces and saturate quickly to avoid flux leakage. SRM will not have such type of problem due to its simple rotor structure, which makes SRM a better candidate for high-speed operation. SRM is also more suitable for running in high-temperature conditions. For PMSM, the magnetic properties of PMs are highly dependent on the operating temperature [9]. The flux density and coercivity of NdFeB magnet reduce as the temperature increases, thereby affecting the output torque and demagnetization. PMSM using NdFeB mag-

nets are usually designed to make sure the magnet temperature can stayed around 100°C during the continuous operation. However, the rotor of SRM is only made of laminated steel, and the surface insulation on electric steels, which is designed to reduce eddy current losses, can handle temperatures in the range of 200°C–400°C [10]. SRM has been adopted in some industrial pumps, vacuum cleaners, and agricultural and mining vehicles. The small market share of SRM originates from its noise, vibration, torque ripple, and challenges in design and optimization due to their nonlinear characteristics. Nowadays, these challenges have been gradually solved in terms of motor designs and control strategies to match the requirements for a wide application range.

1.2 Advantages and disadvantages of SRM

The advantages of SRM are listed as follows:

- No PMs on rotor
  There is no magnet on rotor in the conventional SRM, which means it can withstand high temperature and operate in extreme conditions.

- No windings on rotor
  One important aspect of the SRM is the simple rotor with no windings, which indicates lower rotor losses and less heat dissipation. This is very attractive, because it is hard to remove heat from the rotor.

- Concentrated windings on stator
  SRM has phase windings concentrated around individual stator poles, which is easy to be manufactured, and the short end-turns of the concentrated winding reduces the end-winding losses since there is no cross-coupling between windings and the total stack length will be lower.

- Fault tolerant drive
  It is very easy for multi-phase SRM to realize the fault-tolerant operation. Due to the low cross-coupling effects between phases, SRM is stated as fault tolerant.

- No shoot-through fault
  The upper and lower switches on the same phase leg in the converter of PMSM and IM cannot be activated at the same time, or the direct current (DC) link will be short-circuited. For SRM, the upper and lower switches are electrically isolated from each other by motor winding, which naturally avoids the shoot-through fault condition.

The first two aforementioned advantages are conducive to the high-speed and high-temperature operation of SRM. On the one hand, since there is no PM and windings on rotor, the risk of the rotor disintegration under high centrifugal force in high-speed operation can be reduced. On the other hand, this rotor structure makes SRM competitive in high temperature and other harsh environments, due to the absence of temperature-vulnerable PMs. Compared with PMSM, SRM does not need PM and initial magnetization. Compared with IM, SRM does not need die-casting (in squirrel-cage IM) or additional winding process (in wound-rotor IM) for rotor conductors. Thus, SRM can be easily made at much lower cost.

The disadvantages of SRM is also apparent, which are listed as follows:

- High windage loss
  Although the salient structure of SRM brings advantages, the concave part between rotor poles leads to high windage losses, especially in high-speed operation.

- High torque ripple
  Because of the characteristic torque production principle, SRM has high torque ripple under the pulsive stator magnetic field, which will correspondingly bring about high noise and unnecessary vibration. Therefore, high-performance torque control scheme should be applied to improve the overall SRM drive system performance.

- Synchronized commutation with rotor position
  The initial rotor position should be known by an absolute encoder, or the rotor should be rotated to a pre-known position in order to control the current during the inductance increasing region of each phase. This means the controller needs rotor position, which either can be given by position sensors (encoder, hall elements, resolver, etc.) or by a position sensorless method.

1.3 Power quality improvement methods for grid-connected SRM drive
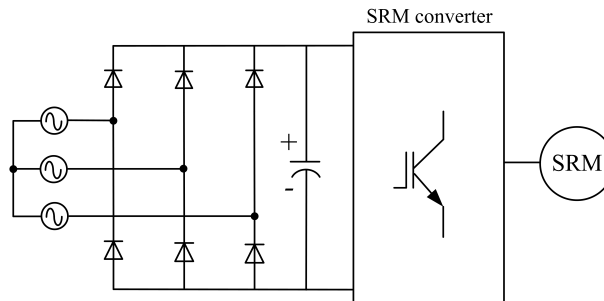
Figure 1.2: SRM drive system based on DBR.

SRM converter needs DC power for operation, and to generate DC power from AC power source, the diode bridge rectifier (DBR) shown in Fig. 1.2 is conventionally adopted. The DBR generates odd non-triplen harmonics in the AC-side current, namely the 1st, 5th, 7th, 11th, 13th, etc. harmonics, and the DC output may contain even the third harmonic: 0th, 6th, 12th, 18th [11], etc. Due to the forced transfer of current from one diode to the next, DBR is a non-linear load for the AC source. When a pair of diodes (one from the upper arms, the other from the lower arms) is on, the output DC voltage is equal to the largest one of the AC-side line voltages. In this case, the largest AC-side line voltage supplies power to both the capacitor and the DC-link load. When all the diodes are off, the DC-link load is supplied by the capacitor energy, and the output DC voltage, i.e., the capacitor voltages, decreases exponentially. Hence, the AC-side current in DBR will be discontinuous and non-sinusoidal, which indicates high current total harmonic

distortion (THD). Furthermore, the motor drive is an inductive load for DBR, so when the motor drive is connected to the end of the DC-link, the voltage is ahead of the current wave, which leads to the phase shift. As a consequence, the high current THD and phase shift inevitably bring about the low grid-side power factor.

AC-side power quality is a high priority for electrical equipment. Some investigations have been conducted to make improvements on AC-side current harmonics and power factors for SRM drive system. In [12], a new drive topology is formed by adding a power switch and a fast recovery diode into the DBR-fed single-phase asymmetrical half-bridge (ASHB) converter. The diode bridge and the DC-link capacitor, which are directly connected in conventional DBR topology, are separated to be the front end and back end in the new topology. Therefore, the absolute value of AC voltage is directly applied to winding terminal during its source current excitation mode, and the back-end DC-link capacitor can be charged either by the demagnetization current of SRM or by AC voltage source. The conduction duration of a newly-added power switch is carefully calculated to make sure the average voltage provided to winding terminal for excitation is constant. However, the instantaneous voltage provided to winding terminal is different for the same electrical position of different strokes, thus producing different current profiles during each excitation. Therefore, though this solution is low-cost and power factor can be improved, the current harmonics are still high.
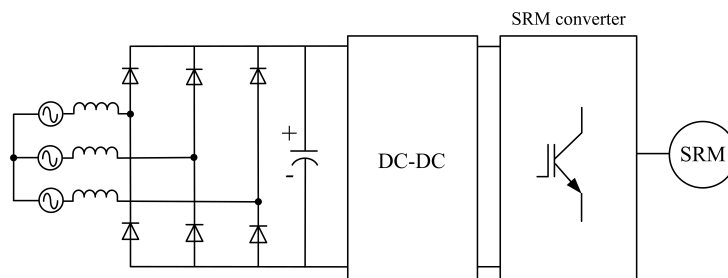
Figure 1.3: SRM drive system based on DBR and DC-DC converter.

The power factor correction converter [13] that consists of a DBR and a DC-DC circuit (shown in 1.3) is largely applied in AC-DC system, such as uninterruptible power supply [14], LED drive [15], motor drive [16], and battery charger [17], to optimize input current harmonics limited by IEC standard. In [18], a modified quasi Z-source converter, a type of DC/DC circuit, is developed to connect between DBR and SRM converter for magnetization voltage regulation and power factor correction. The demagnitization port in this topology is decoupled from the magnetization port and boosted further to reduce demagnetization time, and a peak current control, which coordinates with the voltage controller, is used to correct the AC-side power factor. However, the effect of power factor correction is not satisfying. In [19], a single-phase three-level DC-DC boost converter with dual output is adopted to improve the power factor. The DC-link voltage is controlled through the amplitude of inductor current, and the sinusoidal AC current is realized while synchronizing the phases of inductor current and AC voltage. Since the split-DC converter is adopted as the back-end of the DC-DC boost converter for SRM drive, an additional controller for the balancing of DC-link capacitors must be added to ensure the regular operation of the back-end SRM converter. [20] adopts a single-phase two-level DC-DC boost converter to generate an adjustable DC-link voltage for SRM converter while improving the line drawn power quality for AC side. Its voltage control scheme and current control scheme for the

inductor are basically the same as that in [19], except that it does not need capacitor balancing control. For higher power applications, the three-phase AC source is a natural selection [21–23], and the three-phase single-switch switch-mode rectifier is very attractive [24] in practical applications. In [25], the single-switch DC-DC boost converter is applied in a SRM drive system fed by three-phase AC source. However, the magnetization port and demagnetization port are heavily coupled through shared switches in both [20] and [25], and the experimental AC-side power factors are not satisfying even the current harmonics have been intentionally reduced in the current harmonic cancellation scheme. In [26] and [27], the Cuk converter and modified Cuk converter-fed SRM drive are developed, respectively. The topology in [27] is derived from the single-phase three-level Vienna, and each of the two Cuk converters operates separately for two half-cycles of the AC source. In [28], a converter combining the Cuk and SEPIC circuit together is constructed to provide two balanced output voltages and one neutral point for the SRM split-DC converter. The converter is designed to operate in the discontinuous conduction mode for power factor correction, and SRM is regulated by controlling the adjustable DC-link voltage. But, its DC-link voltage is not fully utilized for excitation, which increases the voltage rating of power switches of SRM converter unnecessarily.

In [29], a three-phase Vienna converter, which directly converts the AC source to DC source and generates a three-level output at DC link, is adopted to drive SRM. Even if the current THD is significantly reduced, just like other power converters with three-level output, the capacitor balancing control also should be considered in order to realize high-performance drive.
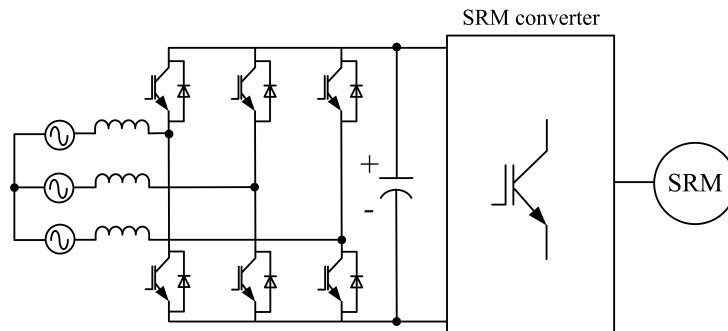
Figure 1.4: SRM drive system based on VSR.

The SRM drivers in the aforementioned topologies cannot directly return energy from the machine to the source due to the current limitation of the diode bridge, so only a limited amount of returned energy is stored in the DC-link capacitor and reused. To overcome this limitation, an additional circuit, such as a dump resistor, is used to dissipate the excess energy generated by the motor during regenerative braking. This helps to prevent the voltage rise on DC link, thus protecting other power electronics components. However, this also results in some energy being lost as heat in the dump resistor, leading to lower efficiency. The SRM drive system fed by the active front end (VSR) shown in Fig. 1.4 can directly transfer the power from the machine side to the AC power supply [30, 31]. This drive system consists of two power conversion stages. The bidirectional power converter in the first stage is composed of six switching blocks, each of which is realized by paralleling one power switch with a diode for one switching block. The power switch bears the positive voltage, and the diodes block the negative voltage excursion. The peak currents are determined primarily by the phase current of SRM, and its voltage ratings

are dependent on the designed DC-link voltage. The second power stage is the commutation stage, through which each phase winding of SRM is energized by the DC-link voltage. The topology for the second power stage can be in various forms according to different system requirements, and the peak currents through the devices are determined primarily by the load of motor.

1.4 Contributions

This dissertation focuses on the centralized control of the VSR-fed high-speed SRM drive system, and its main contributions are as follows:

1) Realize bidirectional power flow.

SRM converter needs DC power for operation. Conventionally, the DBR is adopted to drive the SRM converter, which is shown in Fig. 1.5(a). Although the adoption of the DBR reduces system cost, a large amount of reactive power and current distortion is induced into the grid, which is incredibly harmful to the system. The reactive power leads to additional wattage losses along the lines, increased costs for energy and installation, reduced kVA capacity, and reduced available active power transmitted. High current distortion not only causes overheating and failure at operating conditions below their ratings but also results in decreased power factor. The drive system shown in 1.5(b) inserts a DC-DC converter between the DBR and SRM converter to realize the power factor correction during SRM operation. Although the power quality can be significantly improved, the bidirectional power flow is disabled due to the unidirectional current flow of DBR. If the power from back end cannot flow into the AC side in deceleration process, the DC-link voltage will suffer from the sudden increase. Though the brake resistor can be used on DC link to consume those power to keep a stable DC-link voltage, the size of system will be increased and the energy utilization will be reduced. The above problems can be solved by adopting a DC power source to drive the SRM converter (shown in Fig. 1.5(c)), but this type of system is expensive. In the drive system shown in Fig. 1.5(d), the DC power source that realizes the conversion from AC to DC is replaced by an VSR. This system, which is researched in this dissertation, not only can achieve satisfying power quality but enables bidirectional power flow, so that the power can be injected into the AC side when motor decelerates.

2) Realize a centralized power control strategy.

Several drive systems with improved AC-side power quality are proposed in recent years to drive the SRM. In these systems, the front-end converter and back-end SRM are two separate modules with their respective control schemes, as shown in Fig. 1.6(a). The control scheme of the front-end converter regulates the AC-side power quality, and the control scheme of the SRM drive regulates the motor speed. Nevertheless, as shown in Fig. 1.6(b), this dissertation focuses on treating the front-end converter and the back-end SRM as a whole in a centralized control strategy. Specifically, a direct connection of power between the adopted front-end converter and back-end SRM is built, and the SRM is controlled by manipulating the instantaneous active power flow in the system, and enhanced AC-side power quality is achieved by manipulating the reactive power. Therefore, one control scheme is enough to realize SRM regulation, AC-side power factor correction, and current harmonics restraint simultaneously.

3) Propose a new drive topology with double-voltage demagnetization mode.

A drive topology composed of a T-type single-phase three-level voltage-sourced rectifier
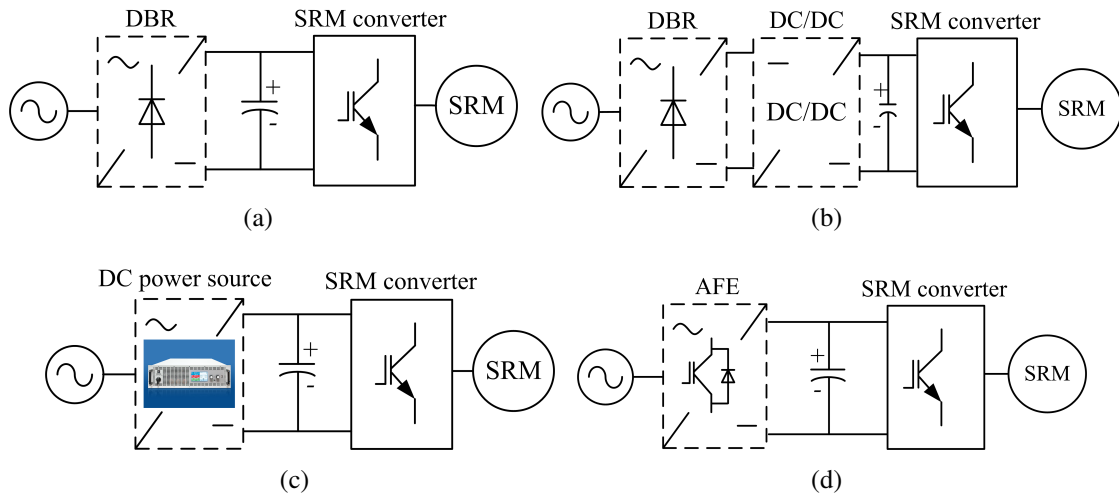
Figure 1.5: SRM drive system. (a) Conventional drive system based on DBR. (b) Conventional drive system based on DBR and DC-DC converter. (c) Conventional drive system based on DC power source. (d) Researched drive system.
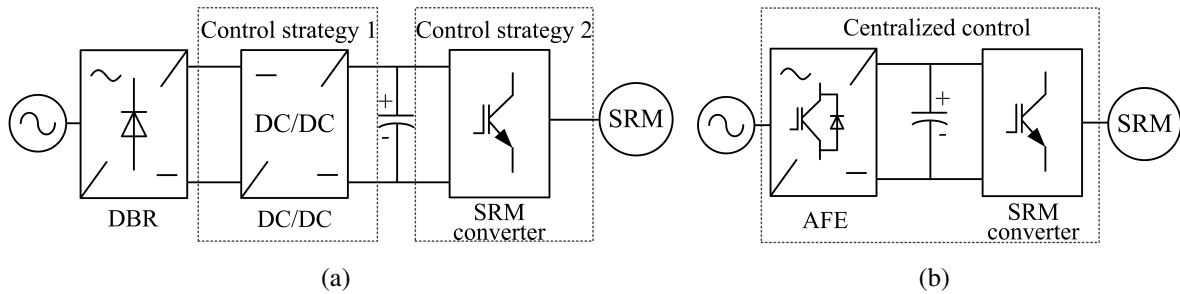
Figure 1.6: Control structures of SRM drive systems with power quality improvements. (a) Existing SRM drive system. (b) Proposed SRM drive system.

(VSR) and a 4-level SRM converter is proposed. Compared with the conventional split-DC converter, the 4-level SRM converter of the proposed drive topology adopts one more switch and one more diode for each phase, but two more operation modes are formed. With the double-voltage demagnetization mode of the 4-level SRM converter, the tailing time of demagnetization current is significantly reduced, which increases the utilization of inductance increasing region. All the operation modes of this converter can be implemented successfully, even in the multi-phase excitation region.

4) Improve system efficiency by the asymmetric space vector pulse width modulation (A-SVPWM).

The A-SVPWM reduces the switching frequency by rearranging the execution order of the selected base vectors of conventional center-aligned SVPWM (C-SVPWM), but the applied converter voltage vector is the same for A-SVPWM and C-SVPWM. Therefore, without causing additional burden on the controller, A-SVPWM can reduce the switching loss by reducing the frequency of switching action, thereby improving the system efficiency.

5) Get rid of the cascade control structure.

Although the grid-connected high-speed SRM drive can be controlled by the centralized control strategy, as proposed previously, an outer speed proportional-integral (PI) controller is always required to generate power reference for inner controller to track, which limits the control performance. Instead of adopting this cascade control structure, a cascade-free model predictive direct power control (MP-DPC) strategy that directly regulates the speed and power flows within a newly-defined cost function is proposed. By evaluating the cost function, the strategy selects the vector which not only will generate a motor speed closer to the setpoint at instant $k+2$, but will generate an active power capable of further reducing that speed error for the future instant. Consequently, well-regulated motor speed, balanced capacitor voltage, and controllable power flow can be achieved within one cost function simultaneously.

6) Robustness improvement against parameter mismatches.

In the model-based control strategy, the mathematical model for prediction is accurate when actual values of inductor and resistor are adopted. However, it is actually the nominal values that are involved in the prediction since the actual values are unknown, and it is also possible that the actual values change during the operation. As the parameter variation occurs in the system model, the error of the predicted value is generated and control performance correspondingly deteriorates. To cope with this issue, the observer-based method is added to the proposed strategy for robustness improvement.

1.5 Outline

The outline of this dissertation is as follows:

In Chapter 2, the operation principle and modelings of SRM are described. The typical SRM structure, power converter topologies, and current regulation techniques of SRM are firstly illustrated. Then the researched high-speed two-phase SRM is introduced in detail in terms of the modified rotor structure, torque profile, and windage loss. The experimental waveforms of the conventional grid-connected SRM drive system based on DBR is presented to show its high pollution of current harmonics and reactive power.

In Chapter 3, a single-phase three-level VSR-fed 4-level converter is proposed to drive high-speed SRM, which significantly reduces the tailing time of demagnetization current by increasing the utilization of inductance increasing region. Moreover, a current control scheme is proposed, which regulates the SRM and power factor by the d-axis and q-axis component of grid-side current, respectively.

In Chapter 4, a centralized predictive deadbeat power control (P-DBPC), which builds a direct connection of power between the front-end VSR and back-end SRM, is proposed to simplify the grid-connected high-speed SRM drive system. Besides, an A-SVPWM method is introduced for switching loss reduction.

In Chapter 5, a cascade-free control strategy is developed to further remove the conventional cascade control structure from the system. Without the outer speed controller, this strategy directly regulates the speed and power flows within a newly-defined cost function.

At last, the whole work is summarized in Chapter 6.

CHAPTER 2

Principle and operation of SRM system

The key to understanding the principle of SRM is its structure, which is introduced firstly in this chapter, and the way of machine operation is inferred. Then, several conventional SRM converters and control techniques that can give full play to the characteristics of SRM are described. Besides, a modified high-speed two-phase SRM, namely, the research target of this dissertation, is described in terms of its structure, torque curve, and windage loss. Finally, the grid-connected SRM drive system based on DBR is explained in detail in terms of experimental waveform and data.

2.1 Modelings of SRM

The number of stator poles and the number of rotor poles are two basic SRM parameters, from which the crucial parameters, such as the number of phases and number of torque pulsations, can be derived. In a SRM, a complete electrical cycle is defined when a rotor pole moves from the position where a certain stator pole is in the middle of two consecutive rotor poles to the next similar position. In other words, for a certain stator pole, the electrical cycle repeats itself by the number of rotor poles in one revolution of the rotor (namely, 360° in mechanical degree). The stator poles belonging to the same phase are connected together and share the same electrical cycle. This means that they are energized and de-energized at the same time during one electrical cycle. As a result, they will produce torque pulses simultaneously in one mechanical revolution. However, for stator poles belonging to other phases, their electrical cycles will be phase-shifted with respect to each other. This means they will produce torque pulses at different time instants within one mechanical revolution. Consequently, the total number of torque pulsations or strokes in one mechanical revolution can be calculated by considering the number of phases and the number of rotor poles in the SRM. If there are m phases, each phase will produce one torque pulsation per electrical cycle. Therefore, the total number of torque

pulsations in one mechanical revolution is given by:

$$N_{pul} = mN_r \tag{2.1}$$

where N_r denotes the number of rotor poles.

SRM has salient poles both on the stator and the rotor. This salient structure is essential for the torque production mechanism of SRM. In this salient structure, the air-gap length changes along with the relative position between the rotor and stator poles. Fig. 2.1 [32] presents the static profile of phase flux linkage under a constant current excitation. It can be seen that the relative distance between the rotor and stator poles is at the largest value when the stator pole is located between two rotor poles, and this position is defined as unaligned position. On the contrary, the relative distance between the rotor and stator poles is at the smallest value when the rotor pole is aligned with the stator poles, and this position is defined as aligned position. Since the reluctance of a magnetic path is proportional to the air-gap length, the flux linkage is at its maximum at aligned position and at its minimum at the unaligned position. Besides the position, winding current also affects the flux linkage. The flux linkage profiles at different rotor positions are presented in Fig. 2.2(a). As the applied current goes higher, the incremental increase in the flux linkage will decrease due to the saturation. Fig. 2.2(b) shows the flux linkage characteristics in Fig. 2.2(a) in a different way. In this case, the flux linkage waveforms are plotted as a function of current at different rotor positions. Notably, at the aligned position, the flux linkage does not increase linearly with current because of magnetic saturation. In contrast, at the unaligned position, the magnetic saturation is not noticeable even at high currents, due to the large air-gap length.
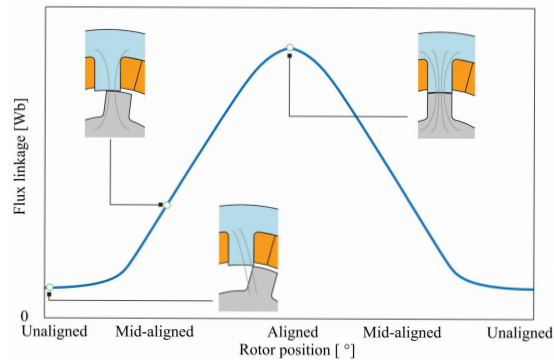
Figure 2.1: Phase flux linkage under a constant current excitation.

Continuous rotation of SRM can be realized by exciting the phase winding on stator poles sequentially, and the phase should be demagnetized before the rotor passes the aligned position to avoid the long tailing current. The structure of a 12/8 SRM presented in Fig. 2.3 is taken as an example to explain the phase excitation sequence. Fig. 2.3(a) shows the rotor position when phase A is at the unaligned position, and this position is designated as 0° (electrical angle) by convention. Hence the aligned position shown in Fig. 2.3(c) corresponds to 180° (electrical angle). From the position in Fig. 2.3(d), if the rotor keeps rotating by 11.25° in mechanical degree, it completes another 90° (electrical angle), and phase A will be again at the unaligned position, but the stator poles of phase A will be between different rotor poles as compared to the unaligned position in Fig. 2.3(a). It can be observed from above that the excitation sequence

Figure 2.2: Phase flux linkage profile. (a) At different positions. (b) At different currents.

relies on the rotation direction. For this 12/8 SRM, the phase should be excited in the sequence of phase A-C-B to realize the clockwise rotation, and the excitation sequence of A-B-C should be adopted to realize the counterclockwise rotation.

2.1.1 Rotor position in SRM

The rotor position can be calculated through the speed as follows:

$$\theta_r(k) = mod(n_r(\frac{360°}{60})T_sk) + \theta_{ini}, 360°) \tag{2.2}$$

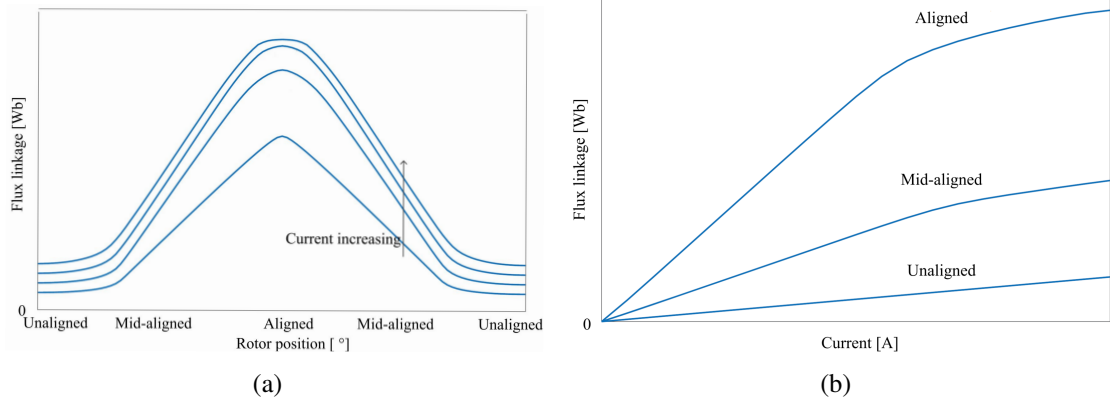where n_r the rotation speed in revolutions-per-minute, T_s is the discrete time step, k is the step number, and θ_{ini} is the initial rotor position. Since one rotation is $360°$, $\frac{360°}{60}$ converts n_r in revolutions-per-minute to degrees-per-second.

2.1.2 Voltage in SRM

SRM is solely excited by the winding on stator. Due to the salient structure of SRM, the air-gap between rotor and stator poles changes based on the relative position of the rotor and the stator, which means the phase inductance in SRM is dependent on rotor position. Therefore, the flux linkage expression of SRM can be given as follows

$$\psi_m = L_m(\theta_r)i_m \tag{2.3}$$

where ψ_m denotes the phase flux linkage, i_m denotes the phase current, L_m denotes the phase inductance, and θ_r denotes the rotor position. The voltage equation is written as

$$v_m = i_m r_m + \frac{d\psi_m}{dt} \tag{2.4}$$

where v_m denotes the terminal voltage of phase winding, and r_m denotes the winding resistance. Inserting (2.3) into (2.4) gives

$$v_m = i_m r_m + L_m(\theta_r)\frac{di_m}{dt} + i_m\frac{dL_m(\theta_r)}{dt} = i_m r_m + L_m(\theta_r)\frac{di_m}{dt} + i_m\frac{dL_m(\theta_r)}{d\theta_r}\frac{d\theta_r}{dt}. \tag{2.5}$$
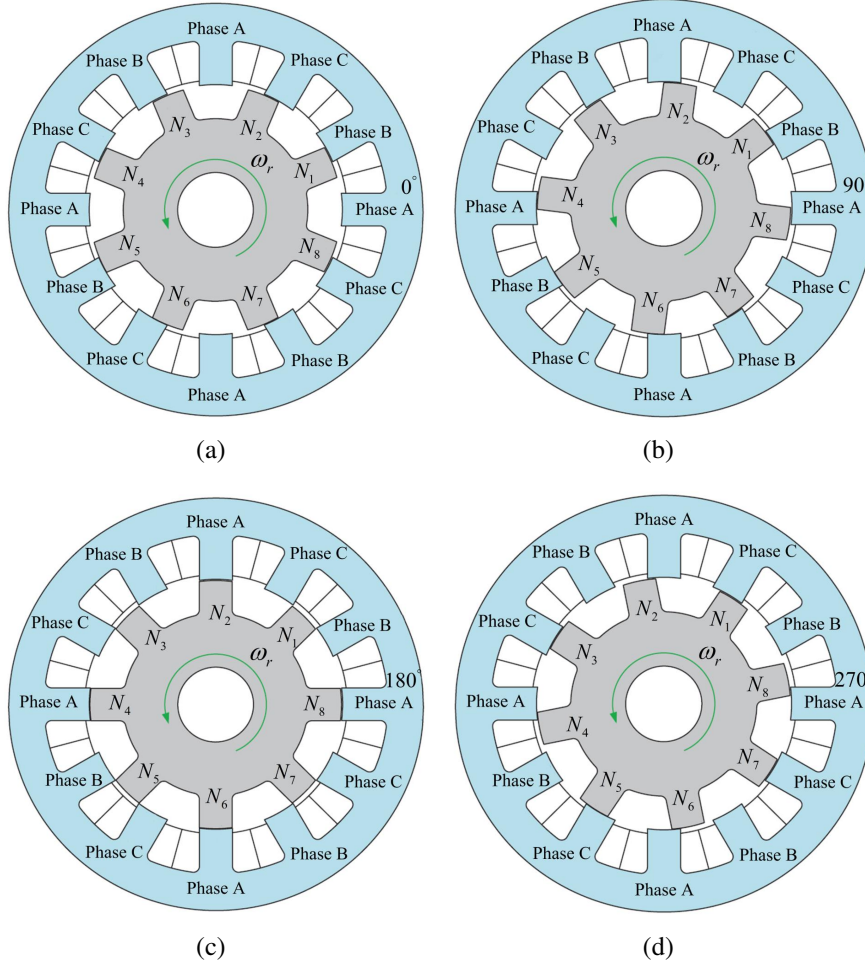
Figure 2.3: Electrical angles at different rotor positions with respect to phase A: (a) At 0°. (b) At 90°. (c) At 180°. (d) At 270°.

Since the angular velocity can be calculated by dividing the rotor position by time, i.e., $\omega_r = \frac{d\theta_r}{dt}$, (2.5) can be simplified as

$$v_m = i_m r_m + L_m(\theta_r)\frac{di_m}{dt} + i\frac{dL_m(\theta_r)}{d\theta_r}\omega_r. \tag{2.6}$$

The speed-dependent term in above expression is called back-electromotive force (back-EMF), and it represents the air-gap power that will be converted into mechanical power.

2.1.3 Power and torque in SRM

The power expression in SRM can be derived by multiplying both sides of (2.6) by phase current

$$i_m v_m = i_m^2 r_m + i_m L_m(\theta_r)\frac{di_m}{dt} + i_m^2\frac{dL_m(\theta_r)}{d\theta_r}\omega_r. \tag{2.7}$$

Under the assumption that the machine is working in the magnetic linear region, the second term on the right-hand side of above expression can be expanded further by using the product

rule for differentiation

$$i_m L_m(\theta_r)\frac{di_m}{dt} = \frac{d}{dt}\left(\frac{1}{2}L_m(\theta_r)i_m^2\right) - \frac{1}{2}i_m^2\frac{dL_m(\theta_r)}{d\theta_r}\frac{d\theta_r}{dt}. \tag{2.8}$$

This third term in above expression can be simplified again by including the rotational speed:

$$i_m L_m(\theta_r)\frac{di_m}{dt} = \frac{d}{dt}\left(\frac{1}{2}L_m(\theta_r)i_m^2\right) - \frac{1}{2}i_m^2\frac{dL_m(\theta_r)}{d\theta_r}\omega_r. \tag{2.9}$$

Substituting (2.9) into (2.7) gives another form of power equation

$$i_m v_m = i_m^2 r_m + \frac{d}{dt}\left(\frac{1}{2}L_m(\theta_r)i_m^2\right) + \frac{1}{2}i_m^2\frac{dL_m(\theta_r)}{d\theta_r}\omega_r. \tag{2.10}$$

It can be seen that the input electrical power is converted to electrical, magnetic, and mechanical power on the right-hand side. The electrical power is dissipated as heat in terms of copper losses. The magnetic power is stored as magnetic field energy in the magnetic core. The remaining power is air-gap power, which is converted into mechanical power and transferred into torque production. Since torque is the quotient of power and angular velocity, i,e., $\tau_{e,m} = \frac{p_{m,em}}{\omega_r}$, the electromagnetic torque can be extracted from (2.10) as follows

$$\tau_{e,m} = \frac{1}{2}i_m^2\frac{dL_m(\theta_r)}{d\theta_r}. \tag{2.11}$$

It can be seen that the direction of torque is independent of the polarity of the current since torque is related to the square of the current. The rate of change of inductance caused by the saliency in the geometry is the primary torque production mechanism in SRM. As stated above, (2.11) is the torque expression when SRM operates in the linear region of the magnetization curve. The general torque equation for SRM is derived using magnetic co-energy W_e', which is applicable for both magnetically linear and saturated regions:

$$\tau_{e,m} = \left.\frac{\partial W_e'(i_m, \theta_r)}{\partial \theta_r}\right|_{i=const}. \tag{2.12}$$

2.2   SRM converter topologies

2.2.1   ASHB converter

The winding current of each phase needs to be conducted in turn as the rotor position changes so that the stator magnetic flux path can rotate along the air gap for continuous torque production. Therefore, a power converter is requisite for SRM to switch on and off the phase current accurately. For SRMs, the ASHB converter is widely adopted because of its control flexibility. Fig. 2.4 presents the circuit diagram of an ASHB converter for one phase, which consists of two power switches and two diodes.

For magnetization mode, the ASHB converter applies the full DC-link voltage to winding by switching on the power switches S_1 and S_2, as shown in Fig. 2.4(a), and the winding current

increases dramatically, especially at the position around the unaligned angle. For demagneti-
zation mode, S_1 and S_2 are switched off at the same time stamp, as shown in Fig. 2.4(c). In
this mode, due to the stored energy in the phase, diode D_1 and D_2 become forward biased, and
negative DC-link voltage is applied to phase winding. The winding current continues to flow
through the diodes, which is supplied back onto DC link until it reaches zero. For freewheeling
mode, only one pair of switch and diode is on, as shown in Fig. 2.4(b). The phase winding is
not connected to the DC link, so no energy flows back to the DC link. Since the voltage across
the phase terminals is zero and the phase is shorted, the current only consumes by winding re-
sistance, which indicates a relatively slower decreasing rate compared to the demagnetization
mode in Fig. 2.4(c). It can be seen from above that the unidirectional current flow is applied
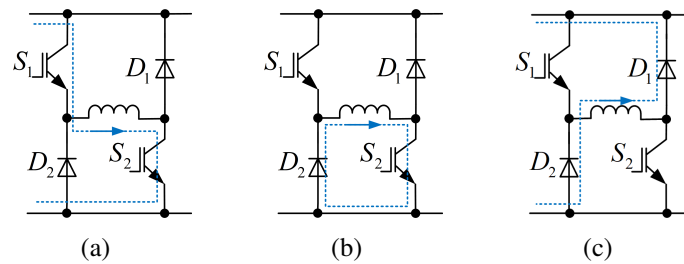

Figure 2.4: Conduction modes of ASHB converter. (a) Magnetization. (b) Freewheeling. (c)
Demagnetization.

to motor winding in ASHB converter, and the winding current of each phase can be electrically
isolated from each other in this type of converter. Hence, the way to obtain the topology for
multi-phase SRM is to duplicate the single-phase ASHB topology in Fig. 2.4 on the DC link.

2.2.2   (N+1)-switch converter

The phase winding of SRM does not need to be conducted during the whole electrical cycle.
Therefore, some of the power switches and diodes can be shared between different phase wind-
ings to reduce the number of power devices. Considering the total number of switches in the
topology is one plus the number of phases, the converter that will be described here is called (N
+ 1)-switch converter.

Fig. 2.5 presents the (N + 1)-switch converter for a three-phase SRM. Four switches and four
diodes are adopted to control the three phases, and the reduction of the number of switches is
realized by sharing a switch between two phases. An obvious drawback of this converter is that
it cannot independently control each phase. For instance, when phase B needs to be excited
before phase A current falls to zero, S_2 is in on-state if this switching pattern is implemented,
which will delay the current decreasing time of phase A and generates negative torque. Alter-
natively, the turn-off position of phase A or the turn-on position of phase B can be delayed to
avoid the overlap, both of which reduce the output power. Furthermore, compared to the ASHB
converter, the current ratings of the shared devices increase because of the conduction overlap.

The converter in Fig. 2.5 is developed into the four-phase converter shown in Fig. 2.6 to
further improve the current control performance. Compared to the (N + 1)-switch converter, the
converter shown in Fig. 2.6 uses more switches and diodes, but the conduction overlap can be

eliminated since only one phase current flows through each device at any time. In this converter, phase A and C share D_2 and S_2, and winding B and D share D_5 and S_5. Phase A and B that have the chance of simultaneous conduction share no common switch and diode. Therefore, each phase current can be independently controlled.

Another example of a (N + 1)-switch converter is shown in Fig. 2.7. Since switch S_1 and diode D_1 are shared by all three phases, the current ratings of switch S_1 and diode D_1 are also higher. Besides, similar to the converter shown in Fig. 2.5, the phase currents also cannot be controlled independently.

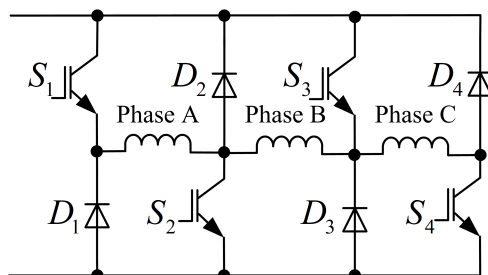Figure 2.5: (N + 1)-switch converter for the three-phase SRM.
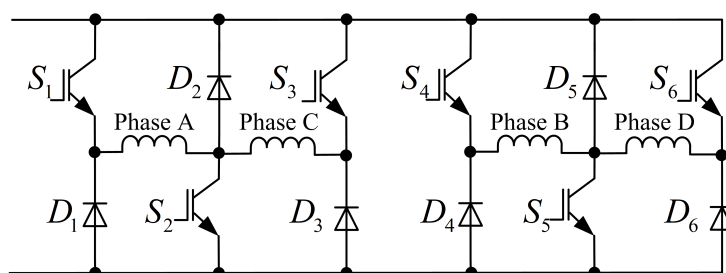

Figure 2.6: A converter with shared devices for the four-phase SRM.
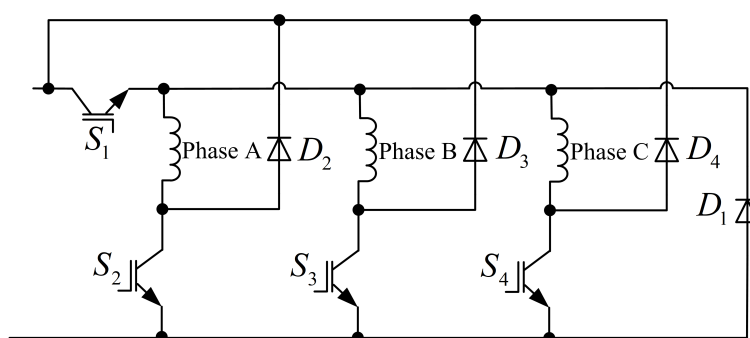

Figure 2.7: An alternative (N + 1)-switch converter.

2.2.3   N-switch converter

The split-DC converter, which uses the same number of switches as the number of phases, is shown in Fig.2.8. Each phase of it has one switch and one diode, and there are two capacitors

on DC link. If phase A needs to be magnetized, S_1 is turned on, and the voltage of upper capacitor is applied to phase A. If phase A needs to be demagnetized, S_1 is turned off, and the decreasing current flow through D_1 into the midpoint of the two capacitors. Hence, a negative capacitor voltage is applied to phase A. If phase B needs to be magnetized, S_2 is turned on, and the voltage of lower capacitor is applied to phase B to build up the winding current. If phase B needs to be demagnetized, S_2 is turned off, and the winding current is decreased through D_2, during which process the voltage of upper capacitor is applied reversely to phase B. Generally, the upper and lower capacitor voltage will be balanced to be the same, and both of them equal the rated operating voltage of the winding terminal voltage of SRM. While fewer power devices are adopted, the voltage rating of diode has to be doubled in order to operate the same SRM as the aforementioned converters.
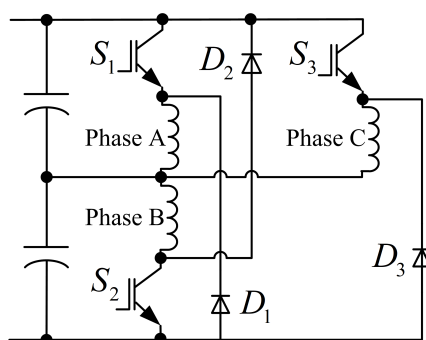
Figure 2.8: Split-DC converter.

2.2.4   Other converter topologies

The converter with higher demagnetization voltage, which is shown in Fig. 2.9, is proposed in [33] to achieve faster commutation as well as higher output power. This converter is derived by adding a buck-boost converter to the ASHB converter. The switch S_m the inductor L_m and the diode D_m compose the buck-boost converter. The voltage of the upper auxiliary capacitor can be controlled by adjusting the duty cycle of the switch S_m. When switches S_1 and S_2 are on, the voltage on the lower main capacitor is applied to the winding of phase A. When switches S_1 and S_2 are off, diodes D_1 and D_2 are forward-biased, and the voltages on the two capacitors are applied to the winding for demagnetization. Therefore, the current falls faster compared to the conventional ASHB converter, which ensures faster commutation.

The power converter capable of generating more than two voltage levels for SRM is called a multi-level converter. The asymmetric three-level neutral point diode clamped (NPC) converter [34] is shown in Fig. 2.10. The various voltage levels obtained in this converter facilitate the fine current tuning, thereby enhancing the control accuracy.

It can be observed that two capacitors are connected to the neutral point of DC link, and each of them has half of the DC-link voltage. The diode D_3 and D_4 are clamped to the neutral point, which helps apply different voltage levels across winding terminal. Totally, there are nine operation modes for each phase leg, which will be explained as follows (phase A is taken as an example):

Figure 2.9: A converter with higher demagnetization voltage.

Mode 1: All switches are in the on-state. The DC-link voltage is applied to the phase winding and current flows through S_1, S_2, S_3, and S_4. D_1, D_2, D_3, and D_4 are blocked. Since no current flows into the neutral point, neutral point voltage u_n is unchanged in this mode, and the phase voltage equals v_{dc}.
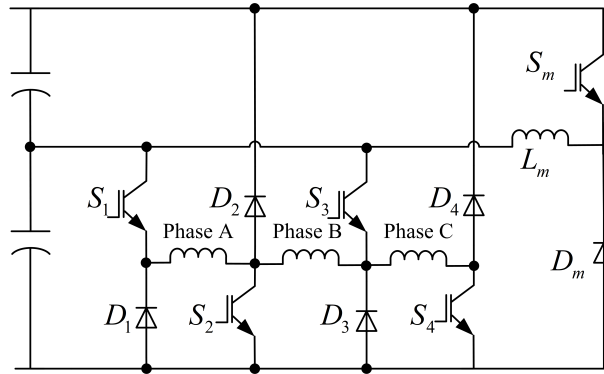
Mode 2: S_1, S_2, and S_3 are in the on-state; S_4 is in the off-state. D_1, D_2, and D_3 are blocked. The phase current flows through S_1, S_2, S_3, and D_4. Therefore, the capacitor voltage difference, which is defined as the voltage difference between the upper and lower capacitors on DC link, decreases since the winding current flows into neutral point. The phase voltage equals $0.5v_{dc}$.

Mode 3: S_1 and S_2 are in the on-state; S_3 and S_4 are in the off-state. Current flows through S_1, S_2, and the freewheeling diode D_2. Diodes D_1, D_3, and D_4 are blocked. No current is injected into the neutral point, which indicates an unchanged neutral point potential, and phase voltage equals 0.

Mode 4: S_1 is in the off-state; S_2, S_3, and S_4 are in the on-state. D_1, D_2, and D_3 are blocked. Current flows through D_4, S_2, S_3, and S_4. The capacitor voltage difference increases since the winding current flows out of neutral point. The phase voltage equals $0.5v_{dc}$.

Mode 5: S_1 and S_4 are in the off-state; S_2 and S_3 are turned on. Current flows through S_2, S_3, D_3, and D_4, and D_1 and D_2 are blocked. The neutral point potential is unchanged, and phase voltage equals 0.

Mode 6: S_1, S_3, and S_4 are off; S_2 is in the on-state. Current flows through D_4, S_2, and D_2. D_1 and D_3 are blocked. Current flows out from the neutral point, thereby increasing the capacitor voltage difference. The phase voltage equals $-v_{dc}/2$.

Mode 7: S_1 and S_2 are off; S_3 and S_4 are on. Current flows through S_3, S_4, and the freewheeling diode D_1. Diodes D_2, D_3, and D_4 are blocked. Since no current flows into the neutral point, u_n is unchanged in this mode. The phase voltage equals 0.

Mode 8: S_1, S_2, and S_4 are off; S_3 is on. Current flows through D_1, S_3, and D_3. D_2 and D_4 are blocked. Current is injected into the neutral point, thereby decreases u_n. The phase voltage is around $-v_{dc}/2$.

Mode 9: All the switches are off. Current flows through the freewheeling diodes D_1 and D_2. D_3 and D_4 are blocked. In this case, u_n is unchanged , and the phase voltage is 0.

Power, voltage and current rating, application requirements, cost, etc. are the aspects that need to be considered in selecting a converter topology, in order to ensure the overall performance of SRM system.
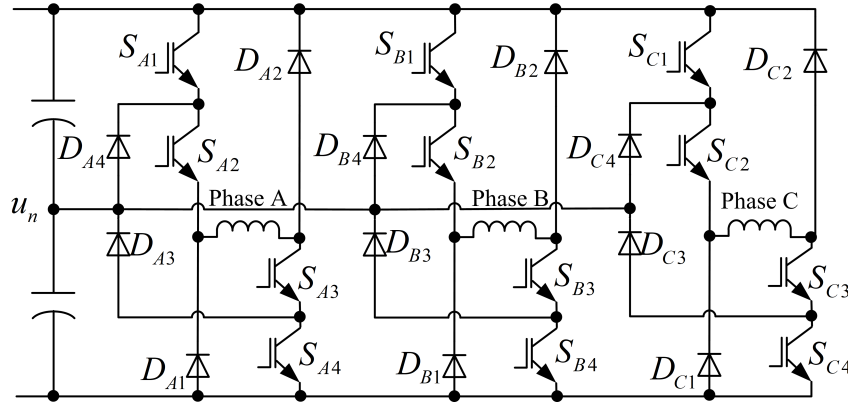
Figure 2.10: Asymmetric NPC three-level converter.

2.3   Current regulation techniques

The ASHB converter shown in Fig. 2.4 is taken as an example to describe the current regulation techniques of SRM.

2.3.1   Single pulse control

The flux in SRM is not constant but must be established from zero every stroke. Specifically, the build-up of flux needs to be initiated at a proper time stamp when the rotor poles are approaching the stator poles of the phase that is due to be excited, which ensures the full utilization of the inductance increasing region for torque generation. The demagnetization of the flux should also start at a proper time stamp to ensure the winding current will not go into the inductance decreasing region to avoid the negative torque. Therefore, the turn-on angle and turn-off angle of each phase winding are two crucial parameters for SRM regulation.

For single pulse control, both power switches are switched on at $\theta_{m,on}$, as shown in Fig. 2.4(a), and both are switched off at $\theta_{m,off}$, as shown in Fig. 2.4(c). Since full DC-link voltage is applied to winding terminal, this control method is suitable for high-speed operation with high back-EMF.

Neglecting r_m in (2.4) gives

$$\psi_m = \psi_{m,ini} + \int \frac{v_m}{\omega_r} d\theta_r \tag{2.13}$$

where $\psi_{m,ini}$ is the pre-existed flux linkage and $\psi_{m,ini} = 0$ for excitation process. Thus, the built-up of flux-linkage can be expressed as follows when $\theta_r \epsilon \left[\theta_{m,on}, \theta_{m,off}\right]$

$$\psi_m = \frac{v_m}{\omega_r} \left(\theta_r - \theta_{m,on}\right) \tag{2.14}$$

It can be found that the flux linkage rises at a constant rate of $\frac{v_m}{\omega_r}$ during the excitation. When the phase winding is switched off, the flux linkage starts to decrease at a constant rate of $-\frac{v_m}{\omega_r}$ since a reversed terminal voltage is applied to the winding, and the flux linkage can be expressed as

$$\psi_m = \psi_{m,ini} + \int \frac{-v_m}{\omega_r} d\theta_r \tag{2.15}$$

where $\psi_{m,ini} = \frac{v_m}{\omega_r}\left(\theta_{m,off} - \theta_{m,on}\right)$ for demagnetization process. Hence, the flux-linkage can be expressed as follows when $\theta_r \in [\theta_{m,off}, \theta_{m,zero}]$ ($\theta_{m,zero}$ denotes the position when the winding current drops to zero)

$$\psi_m = \frac{v_m}{\omega_r}\left(2\theta_{m,off} - \theta_{m,on} - \theta_r\right) \tag{2.16}$$

If $\theta_r \in [\theta_{m,zero}, \theta_{m,on}]$, $\psi_m = 0$ since there is no voltage at the winding terminal.

The profiles of voltage, flux linkage, current, and inductance in single pulse control are shown in Fig. 2.11. Generally, a pair of turn-on angle and turn-off angle suitable at one speed will not be the optimal one to run the SRM at other speeds, since the torque profile changes due to the saturation in high-speed operation. In order to improve the torque quality, the torque ripple has to be minimized. The minimum torque ripple is not always achievable because there are constraints on phase current and conduction angles. Furthermore, the objective of minimizing torque ripple has to be balanced with the objective of maximizing output torque. In [35], a conduction angle optimization method based on simulation is introduced. A model that calculates the dynamic torque profile of the machine for the given conduction angles is requisite and the firing angles are taken as variables. The root mean square (RMS) value of torque ripple, average torque, etc. are taken as the objectives to select the optimum conduction angles. The reference speed and commanding current, which represent the operating conditions, are inputs for the SRM drive model.
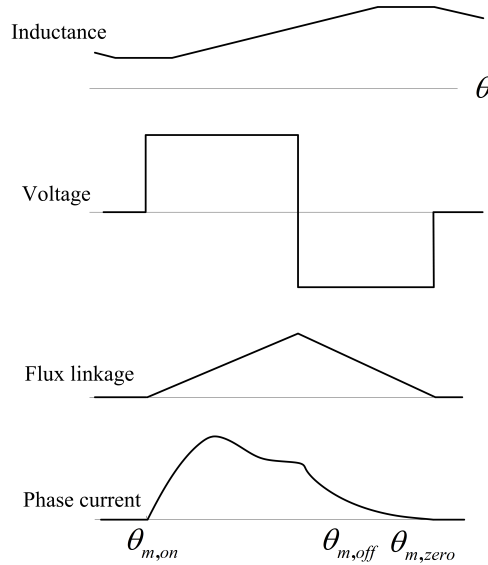

Figure 2.11: Single pulse control.

2.3.2   Current chopping control

Current chopping control, which chops the phase current by PWM signals, is suitable for SRM to operate at low speed. The peak current at low speeds must be controlled at the command value $i_{m,ref}$ in order to maintain the smooth operation of SRM. This is accomplished by switching the DC-link voltage according to the PWM signals, and there are mainly three ways to generate the PWM signals.

- Hysteresis current control. In order to track the current command $i_{m,ref}$, the hysteresis current controller generates the switching signals to switch the DC-link voltage and regulate the phase current. To maintain the phase current roughly at some constant value $i_{m,ref}$, a hysteresis band is defined by $I_{m,upper}$ and $I_{m,lower}$. These values are calculated in light of current command, $i_{m,ref}$ and the tolerance β, which is set to be a percentage of the current command. Two conduction modes can be used to respond to the switching signals. One is the soft chopping, in which the terminal voltage of SRM alternates between the DC-link voltage and zero during the conduction period (as shown in Fig. 2.12(a)). The conduction pattern of soft chopping is a combination of the magnetization mode shown in Fig. 2.4(a) and the freewheeling mode shown in Fig. 2.4(b). When feedback current is lower than $I_{m,lower}$, both the two power switches on the path from winding to DC power source are switched on, and only one is switched off when the feedback current is higher than $I_{m,upper}$, and both are switched off when the rotor angle position reaches the turn-off angle. The conduction pattern of hard chopping is a combination of the magnetization mode shown in Fig. 2.4(a) and the demagnetization mode shown in Fig. 2.4(c). When the feedback current is lower than $I_{m,lower}$, both the two power switches on the path from winding to DC power source are switched on, and both are switched off when feedback current is higher than $I_{m,upper}$, and both are switched off when the rotor angle position reaches the turn-off angle.
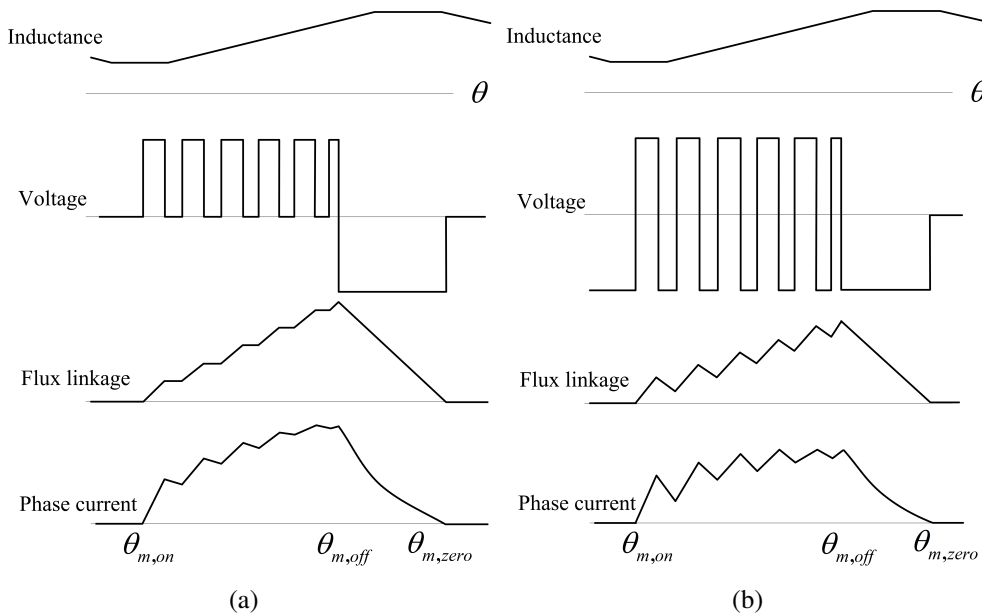
Figure 2.12: Chopping methods. (a) Soft chopping. (b) Hard chopping.

- Current controller. The current controller generates the duty cycle for PWM signals so that the current command set by the speed controller can be tracked. The generated duty cycle must be limited inside the range of [0, 100%] to ensure a reasonable PWM signal. Same as the hysteresis control, current controller can adopt either soft chopping or hard chopping to respond to the PWM signals. One PWM signal is sufficient to control the two power switches simultaneously for hard chopping. But, compared with hard chopping, soft chopping has less switching loss and current ripple.

- Speed controller. The speed controller directly generates the duty cycle for PWM signals to track the speed command. Same as before, both soft chopping and hard chopping can be adopted to respond to the PWM signals. Since there is no current limitation in this type of single control loop system, the hardware current limitation based on comparator chip must be adopted.

2.4 The researched high-speed two-phase SRM
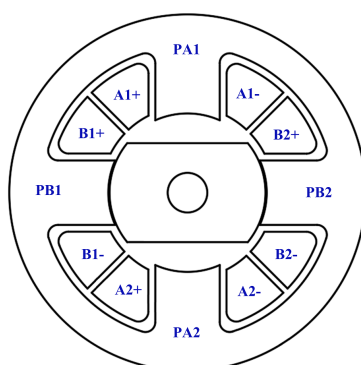
Figure 2.13: Cross-section of conventional 4/2 SRM.
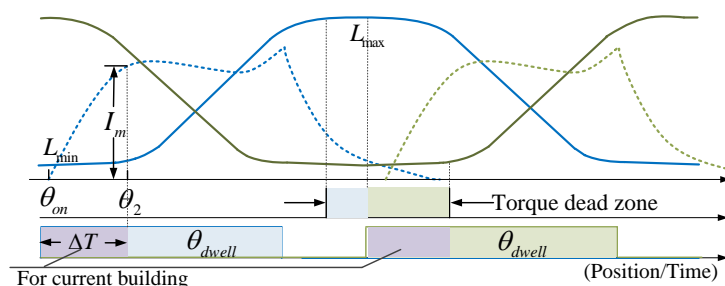
Figure 2.14: Characteristic profiles of conventional 4/2 SRM.

Considering self-start, bi-directional rotation, and smooth torque profile, three or four-phase SRMs are most frequently used. However, high-frequency switching loss and relatively expensive converter make them lose the competitive edge in high-speed operation. As for single-phase SRM, although it is a low-cost drive system with low switching frequency, it can not get a satisfying torque profile due to the intrinsic structural problem [36, 37]. Two-phase SRM can

realize self-start and eliminate torque dead zone by optimizing the rotor shape. Hence, it is an appropriate research target for high-speed operation compared with other topologies. The cross-section and characteristic profiles of the conventional 4/2 SRM are shown in Fig. 2.13 and Fig. 2.14, respectively. Because the electromagnetic torque is proportional to the inductance slope, the flatness of torque profile is tightly tied to the width of the minimum and maximum inductance region, which means the torque dead zone can be easily formed around the aligned and unaligned position. As can be seen from Fig. 2.14, although there is conduction overlap between phase A and B, the torque dead zone is still formed since the current supplied in the region around the unaligned position is just used for fast current building, not for torque generation. This situation can be more serious with the increase of the current due to the saturation since the larger the current is, the broader the torque dead zone and the higher the torque ripple will be.

Torque ripple is the inborn problem caused by the structural and working principle of SRM. There are many researches regarding how to improve the torque profiles of three and four-phase SRM. Several segmental rotors corresponding to different magnetic flux paths [38–40] have been proposed to increase output torque ability by shorting the flux path. To reduce the complexity of the rotation part in above geometries, SRM with the segmental stator [41, 42] are proposed while maintaining comparative torque density. Nevertheless, most of them rely on the balance cooperation between multiple poles, which cannot be applied to two-phase SRM. The idea in [43] modifies the stack length of the rotor of a two-phase SRM according to the rotor position while keeping the air-gap length at a constant value. In [44], the asymmetrical rotor with one step is designed to eliminate the torque dead zone for the two-phase SRM, but the step design is fulfilled by blind multi-parameter optimization. To save labor and get an ideal torque profile, an iteration process based on finite element method (FEM) and MATLAB is proposed in [45]. The torque ripple in that paper has been reduced dramatically with curvilinear rotor pole shape, yet the difficulty in manufacture is a fatal defect. In the following content, a two-phase high-speed SRM with modified rotor for torque ripple reduction and torque dead zone elimination will presented in detail.

2.4.1   Toque dead zone elimination

The torque dead zone are the inborn problems existing in high-speed 4/2 SRM, and the structural optimization is a ideal way to solve them radically. Though the optimized structures vary greatly in design, a unified torque optimization criterion can be derived as follows.

As has been given in (2.12), the instantaneous electromagnetic torque $(\tau_{e,m})$ of SRM can be calculated from the partial derivative of the co-energy with respect to rotor position while holding the current constant. Therefore, the average electromagnetic torque can be expressed as:

$$\begin{aligned}
\tau_{avg} &= \frac{\int_{\theta_u}^{\theta_a} \tau_{e,m} d\theta_r}{(\theta_a - \theta_u)} \\
&= \frac{\int_{\theta_u}^{\theta_a} \left(\left.\frac{\partial W_e'(i_m,\theta_r)}{\partial \theta_r}\right|_{i_m=const} \right) d\theta_r}{(\theta_a - \theta_u)} \\
&= \frac{\left. W_e'(i_m,\theta_r)\right|_{i_m=const}\Big|_{\theta_u}^{\theta_a} + \left.\varphi_m(i_m)\right|_{i_m=const}}{(\theta_a - \theta_u)} \\
&= \frac{\left(\left. W_e'(i_m,\theta_a)\right|_{i_m=const} - \left. W_e'(i_m,\theta_u)\right|_{i_m=const} \right) + \left.\varphi_m(i_m)\right|_{i_m=const}}{(\theta_a - \theta_u)}
\end{aligned} \tag{2.17}$$

where θ_a, θ_u are the fully aligned and unaligned position, respectively, and $\varphi_m(i_m)$ is the function of i_m. It can be found that the average torque just hinges on the co-energy difference between aligned and unaligned position at a constant current. Because the reluctance of air-gap is much bigger than that of the ferromagnetic material, almost all the energy is stored in air-gap. The inductance can be an intuitive value for the description of torque. In the assumption of a linear magnetic system, the above average torque can be rewritten as below:

$$\tau_{avg} = \frac{\frac{1}{2}i_m^2 \left. (L_{m,a} - L_{m,u})\right|_{i_m=const} + \left.\varphi_m(i_m)\right|_{i_m=const}}{(\theta_a - \theta_u)} \tag{2.18}$$

where $L_{m,a}$ and $L_{m,u}$ represent the inductance at aligned and unaligned position respectively. It can be found that although the outline shape of the rotor might be modified with infinite changes during the optimization process, the output average torque can be guaranteed easily by setting the inductance at aligned and unaligned position to appropriate values. Combining (2.17) and (2.18) gives

$$\tau_{avg} (\theta_a - \theta_u) = \frac{1}{2}i_m^2 \left. (L_{m,a} - L_{m,u})\right|_{i_m=const} + \left.\varphi_m(i_m)\right|_{i_m=const} = \int_{\theta_u}^{\theta_a} \tau_{e,m} d\theta. \tag{2.19}$$

It can be found from (2.19) that for different rotor shapes, despite the average torque changes due to the enlarged motoring region $[\theta_a, \theta_u]$ in the deformed inductance profile, as long as the inductance value $L_{m,a}$ and $L_{m,u}$ are fixed, the integral of instantaneous torque during the motoring region is a constant. Furthermore, if $L_{m,a}$ and $L_{m,u}$ are fixed, rotor shape optimization cannot increase the output energy, but it indeed assists with torque ripple reduction by making the torque distribute uniformly among the whole motoring region.

For SRM, the most common method used to eliminate the torque dead zone is to narrow the blank torque region between two sequent conducting phases by designing an asymmetrical shape of rotor, during which process a desired electromagnetic torque can be obtained. The geometries of the conventional and modified rotor structure are presented in Fig. 2.15, and their corresponding torque and inductance profiles are presented in Fig. 2.16. Two steps are added to expand the inductance increasing region, resulting in a more uniform torque distribution. In contrast with conventional rotor, the torque profile of the asymmetric rotor with steps has been apparently flattened. Despite the average torque of optimized rotor decreases compared with that of the conventional rotor, the motoring region of the optimized rotor has been extended dramatically to eliminate the torque dead zone.

(a)   (b)
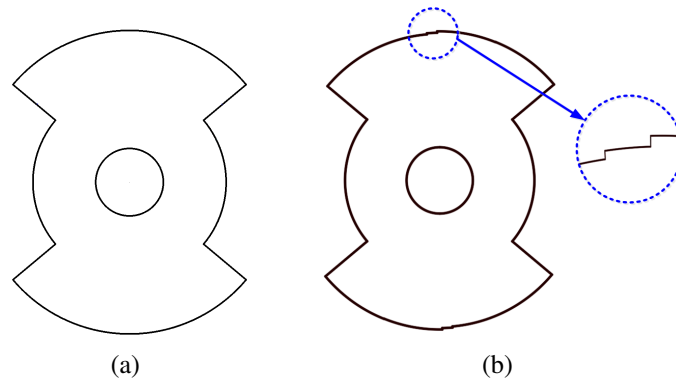
Figure 2.15: Rotor structure. (a) Conventional rotor structure. (b) Stepped rotor structure.
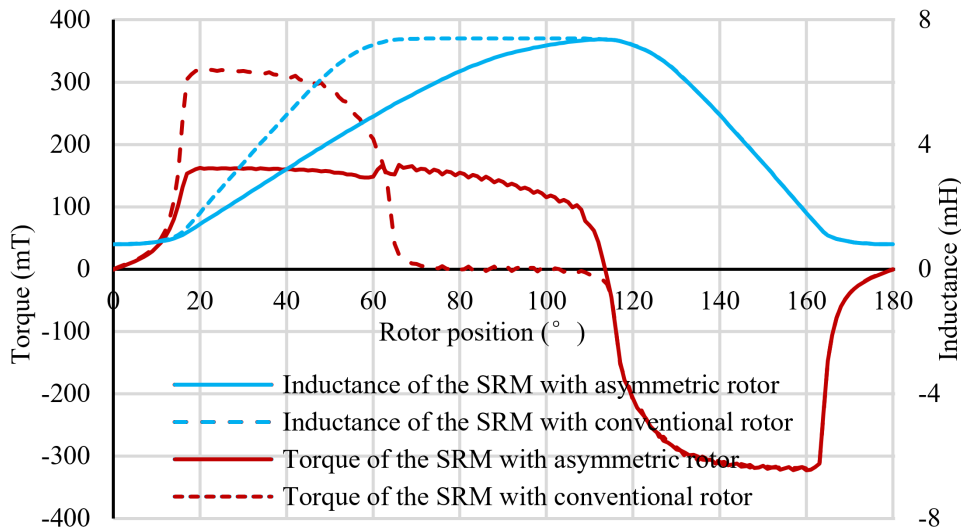
Figure 2.16: Torque and inductance profiles.

2.4.2   Windage loss

One challenge uniquely faced by a high-speed motor is the aerodynamic losses generated by the uneven surface of stator and rotor. Nevertheless, the rotor and stator of SRM must have sufficient saliency due to its torque generation principle. Thus, the proportion of windage loss to total loss is quite large for high-speed SRM compared with other types of motors. The key of windage loss reduction lies in smoothing the structure outline without generating too much extra negative effect. Some methods are proposed to reduce windage loss by optimizing the rotor. For example, in [46–48], a very thin circular bridge made from magnetic material are designed to form a round smooth outside surface for rotor. Despite it does take effect in decreasing windage loss, the reduction in torque generation brought by the magnetic rib is non-ignorable. Moreover, to avoid the increase of minimum inductance, the ribs on the rotor have to be as thin as possible, which makes the unavoidable consideration for their mechanical strength and manufacturing complexity. In [49], the torque reduction can be avoided by making use of the induced flux brought by the eddy current on the aluminum screen, but it is a fairly complex structure.

For the 4/2 high-speed SRM researched in this dissertation, a cylindrical rotor is formed by padding the concave sections between rotor poles, which greatly contributes to the reduction of turbulent flow pattern without introducing effect on electromagnetic aspect. Fig. 2.17(a) shows the three-dimensional (3D) structure of the SRM with stepped rotor before padding. It can be seen that a crucial challenge faced by this high-speed SRM is the high windage loss caused by the salient geometry and high rotational speed. Fig. 2.17(b) presents the modified cylindrical rotor. In this structure, the concaves between adjacent salient rotor poles are padded with high-thermal conductivity resin. These two resin blocks are fixed tightly into the concaves and for the sake of security, the ends of resin block are secured once again by the resin end ring to meet the mechanical strength requirement.
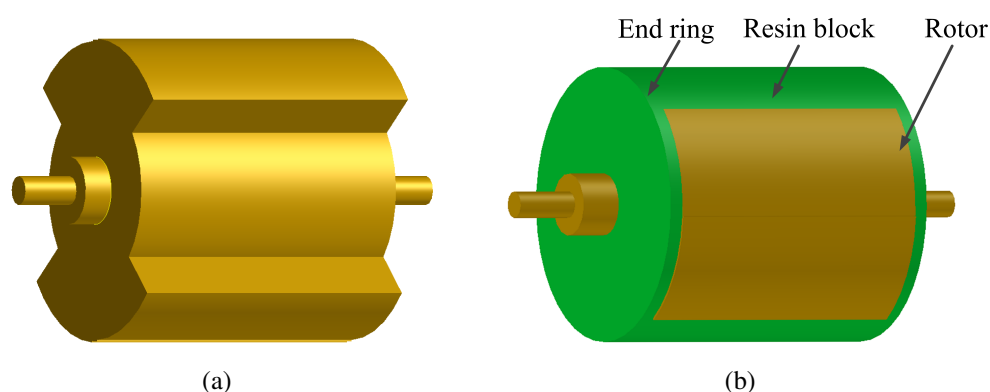

Figure 2.17: Rotor structure. (a) Stepped rotor. (b) Modified cylindrical rotor with high-thermal conductivity resin.

The windage loss is susceptible to the velocity distribution in the air-gap, the geometry of the fluid channel, the flow rate of cooling air, and the property of cooling air. The velocity distribution in the air-gap depends on three factors: the tangential flow caused by the electromagnetic torque, the axial flow of cooling air caused by axial ventilation, and the Taylor vortex caused by high-speed centrifugal force. When the air velocity in motor is low, the air flow pattern can be considered laminar flow. Whereas, in high-speed SRM, with the high linear velocity and the salient structure of rotor, the turbulent model should be introduced. In turbulent flow, the fluid in the air-gap can be divided into three layers as presented in Fig. 2.18: the viscous bottom layer near the stator and rotor surface and the complete turbulent layer. Note should be paid that it is in the viscous sublayer that the energy exchange process happens and the windage loss is generated. To predict the windage loss in the fluid channel of SRM, the analytical techniques in [50], [51] employ the mathematical equation which relies on a series of empirically determined constants and the assumption of a cylindrical stator bore. Two-dimensional computational fluid dynamics (CFD) method in [52] can obtain a more accurate result, yet the model is still built based on a cylindrical stator bore. There always exists a big air pocket in the stator slot since the stator slot fill factor is less than 0.4 considering the installation of the concentrated winding and the saturation of the motor. Although cylindrical stator bore can be achieved by incorporating specially-designed non-magnetic slot closures, or by encapsulating the entire stator, the side effect such as the complex stator construction and bad cooling environment are severe problems, so the cylindrical stator bore is rarely used in practical system.

Stator surface _____   Stator surface _____

                        Viscous sublayer   Viscous sublayer

-------------------------------- Turbulent layer   -------------------------------- Turbulent layer

-------------------------------- Viscous sublayer   -------------------------------- Viscous sublayer

Rotor surface _____   Rotor surface _____

                (a)   (b)
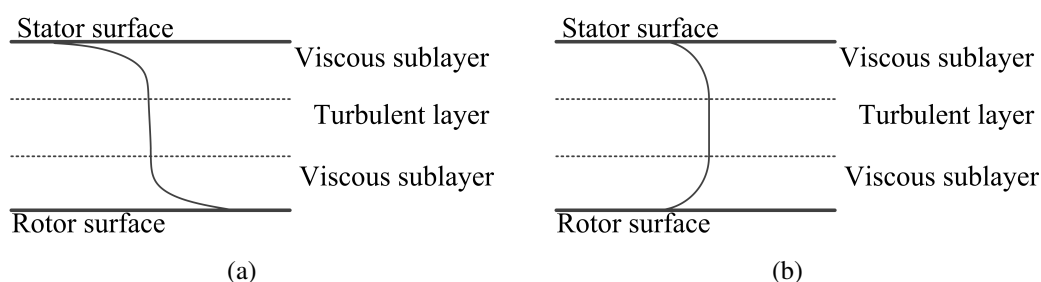
Figure 2.18: Turbulent flows in air-gap. (a) Tangential velocity. (b) Axial velocity.

(a)

(b)
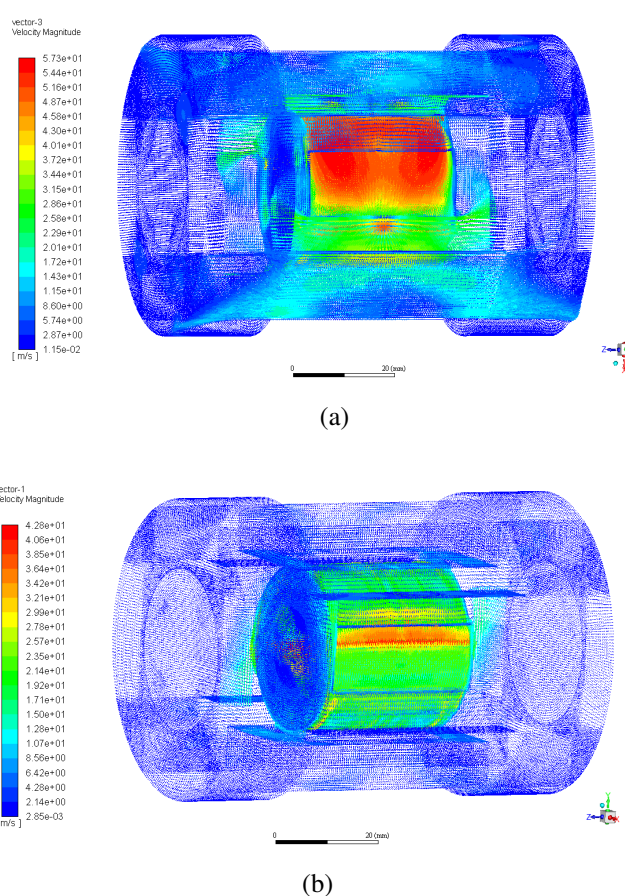
Figure 2.19: The velocity vector distribution of the fluid inside the solution domain. (a) Motor with stepped rotor. (b) Motor with proposed cylindrical rotor.

Instead of the analytical calculation based on the simplified model and empirical formula, the CFD is used here to calculate aerodynamic loss in the fluid channel of the motor. To illustrate the improvement of the cylindrical rotor, fluid solution domain model of the motor with stepped rotor is also built in Fluent/ANSYS. In 3D model, the end effect caused by short stack length can be taken into account in analysis as well. To guarantee the element quality and obtain convergence results, most of elements are controlled to be the hexahedron by proper grid partition

Figure 2.20: The velocity magnitude contour of one surface in the air-gap. (a) Motor with stepped rotor. (b) Motor with cylindrical rotor.

method. The simulation is analyzed when the rotor locates at the unaligned position of phase A. Fig. 2.19 presents the velocity vector distribution of the fluid inside the solution domain when motors operate at 30000 r/min. It can be found from Fig. 2.19(a) that the velocity magnitude in the motor with co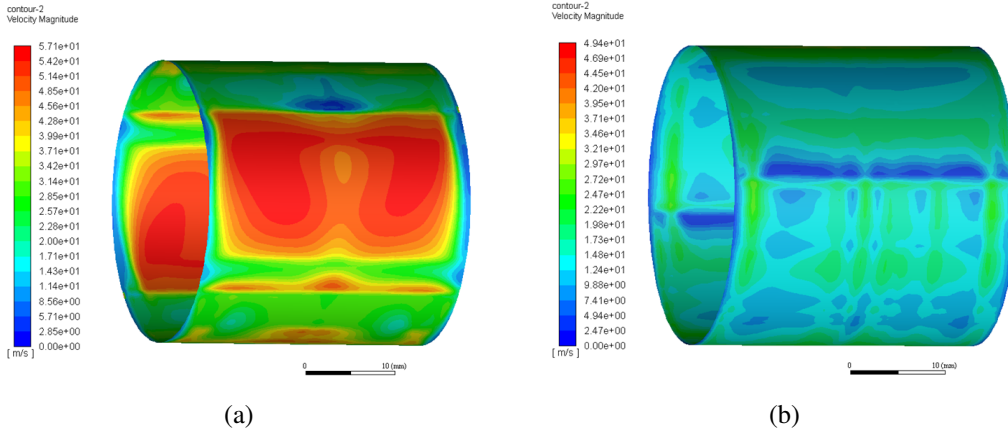nventional stepped rotor is much higher than that in the motor with cylindrical rotor (Fig. 2.19(b)). In Fig. 2.19(a), because of the high-speed mechanical rotation, the air inside the concaves not only be pushed to rotate synchronously with the rotor, but also has a relative motion with the rotor surface, but this phenomenon is not obvious in Fig. 2.19(b). Since the windage loss is tightly tied to velocity distribution on rotary surface, more windage loss will be generated in the motor with stepped rotor. In Fig. 2.19(a), the stator slot is providing a passageway for air flow and the air velocity in it is quite obvious, which also indicates that the stator part cannot be simply regarded as a cylindrical stator bore.

Fig. 2.20 gives out the velocity magnitude contours on a cylindrical surface extracted from mid of the air-gap. By padding the concaves between rotor poles the air velocity magnitude can be decreased prominently. Fig. 2.21 and Fig. 2.22 present the radial cross-section velocity vector graph extracted from the mid of the stack length of motor with stepped rotor and cylindrical rotor, respectively. Compared with Fig. 2.22(b), a bigger whirlpool has been formed inside the stator pockets in Fig. 2.21(b). Due to the expansion of the turbulent flow region and the shrink of the viscous sublayer, the windage loss on the stator surface of the motor with stepped rotor will be lower than that of the motor with cylindrical rotor. Whereas, since the overall velocity in the structure of Fig. 2.21 is much bigger than Fig. 2.22, the conventional rotor with no padding generates more loss.

To analyze the motors with different rotors, the windage loss obtained by CFD simulation at different operation speeds is plotted in Fig. 2.23. There is a relation between windage loss and operation speed and the following equation is assumed:

$$P_{m,w} = k_0 n^{\alpha_0} \tag{2.20}$$

where $P_{m,w}$ represents the windage loss in watt and n represents the operation speed in r/min. After the power function is applied to fit the discrete data points, smooth fitting curves shown

(a)

(b)

Figure 2.21: The velocity vector graphs of the motor with stepped rotor. (a) The velocity vector at a radial cross-section in the mid of the stack length. (b) Enlarged figure of the square frame part in (a).

in Fig. 2.23 can be got. For the motor with stepped rotor, $k_0 = 7.403 \times 10^{-13}$ and $\alpha_0 = 2.973$. For the motor with cylindrical rotor, $k_0 = 4.721 \times 10^{-13}$ and $\alpha_0 = 2.81$. The windage loss increases sharply with the increase of speed. The differences between the two fitting curves of windage loss are brought by the concave between rotor poles. It can be seen that the windage loss has slumped by adopting the cylindrical rotor and the higher the speed, the more effective this design will be. In brief, for high-speed SRMs, forming a smooth outline by padding the concaves between rotor poles is an effective method for power loss reduction.

2.5   Grid-connected SRM drive system based on DBR

SRM converter needs DC voltage for operation. The DBR circuit shown in Fig. 2.24 is a common power conversion method that converts AC voltage from the grid to DC voltage for SRM drive. The DBR consists of several diodes arranged in a bridge configuration, and the
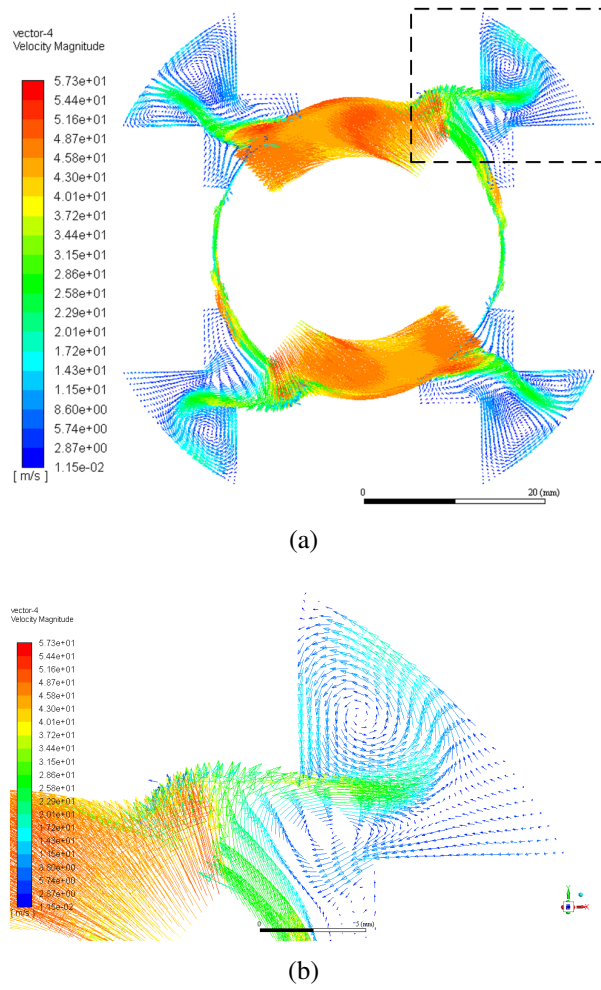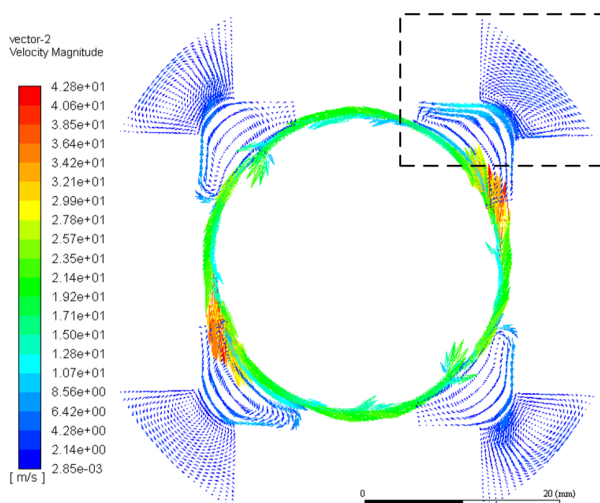
(a)

(b)

Figure 2.22: The velocity vector graphs of the motor with cylindrical rotor. (a) The velocity vector at a radial cross-section in the mid of the stack length. (b) Enlarged figure of the square frame part in (a).
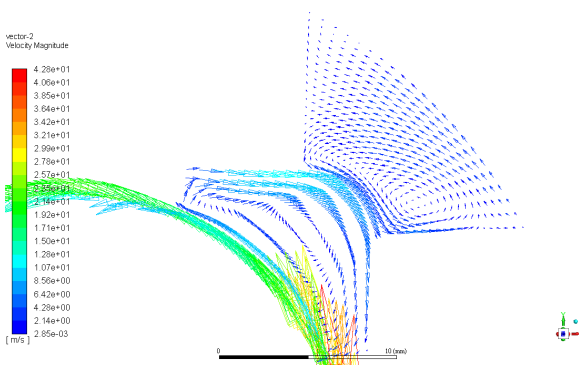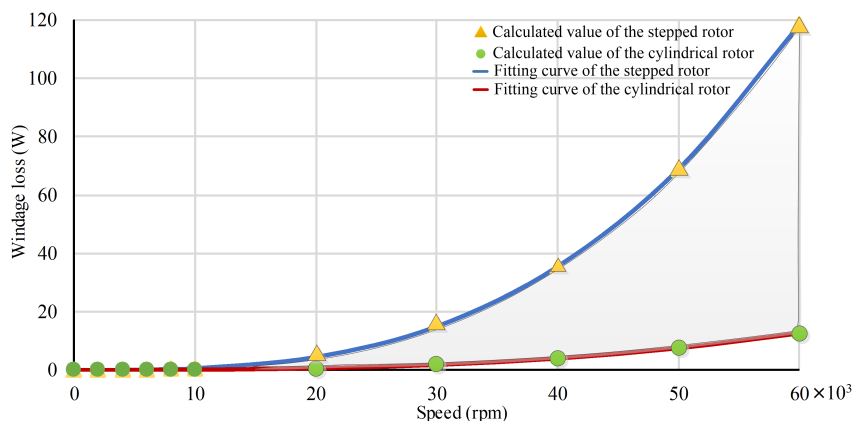

Figure 2.23: Windage loss

output voltage is determined by the state of the diodes. Due to the forced transfer of current from one diode to the next, DBR is a non-linear load for the AC source [53]. When a pair of diodes (one from the upper arms and one from the lower arms) is on, the output DC voltage is equal to the highest voltage from the grid-side line voltages. In this case, the largest grid-side line voltage supplies power to both the capacitor and the DC-link load. However, when all the diodes are off, the DC-link load is supplied by the capacitor energy, causing the output voltage, or the capacitor voltages, to decrease exponentially. Hence, the grid-side current to become discontinuous and non-sinusoidal, leading to high current THD. Additionally, the motor drive acts as an inductive load for the DBR, which causes a phase shift between the voltage and current waveforms. As a consequence, the high current THD and phase shift inevitably bring about the low grid-side power factor [54]. Therefore, although the adoption of DBR reduces system cost, a large amount of reactive power and current harmonics, which have severe damage to power quality, will flow inside grid. The reactive power leads to additional wattage losses along the lines, increased costs for energy and installation, and reduced available real power transmitted. High current distortion not only causes overheating and failure at operating conditions below their ratings but also results in decreased power factor. Besides, the uncontrollable DC bus voltage of DBR is susceptible to the operation condition of the SRM.
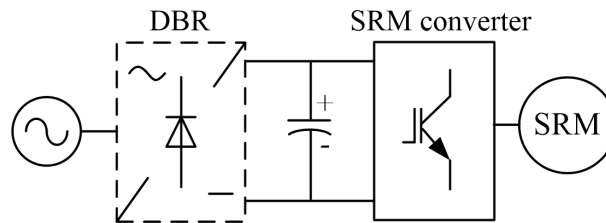
Figure 2.24: Grid-connected SRM drive system based on DBR.

2.5.1   Single-phase DBR-fed SRM drive system

The experiments of single-phase DBR-fed SRM drive system are implemented and relevant experimental parameters are itemized in Table 2.1. In experiments, the 4/2 SRM presented in last section, which achieves self-starting by designing steps on rotor, is employed to carry a fan-type load for tests.

The steady-state test waveforms of the conventional drive system at the rated speed of 25000 r/min are presented in Fig. 2.25. Besides the phase shift relative to grid-side voltage, the grid-side current presents obvious distortions, which results in not only poor current THD but also high reactive power. It means with the same capacity, the available real power that can be transmitted is reduced. In other words, more apparent power will flow in the grid in this system when providing the same output power for SRM. Fig. 2.26 shows the screen captures of the Yokogawa power analyzer in the single-phase DBR-fed SRM drive system. In the power analyzer, $P_1, Q_1, S_1, Ithd_1$, and λ_1 denote the real power, reactive power, apparent power, current THD, and power factor of grid, respectively. η_1 represents the efficiency of entire drive topology, and η_2 represents the efficiency of front-end converter, namely the DBR. For the conventional drive system, the uncontrollable front-end DBR has conduction loss but no switching loss, so it consumes less real power P_1 than the other VSRs with power switches when providing the same

output power for SRM, thereby resulting in the higher η_2 and higher η_1. As summarized in Fig. 2.27, the power factors of this drive system are just around 0.74, and the grid-side current THDs are around 70%.

Table 2.1: Experimental parameters of single-phase DBR-fed High-speed SRM drive system

Description	Parameter	Value
Frequency of grid-side voltage	$\omega_g(\mathrm{rad/s})$	$100\,\pi$
Grid-side filter resistance	$R_g(\Omega)$	0.2
Grid-side filter inductance	$L_g(\mathrm{mH})$	4
DC-link capacitor	$C(\mu\mathrm{F})$	2720
Control period	$T_s(\mu\mathrm{s})$	50
Rated torque of the high-speed SRM	$\tau_{em}(\mathrm{N\cdot m})$	0.12
Rated speed of the high-speed SRM	$n_r(\mathrm{r/min})$	25000
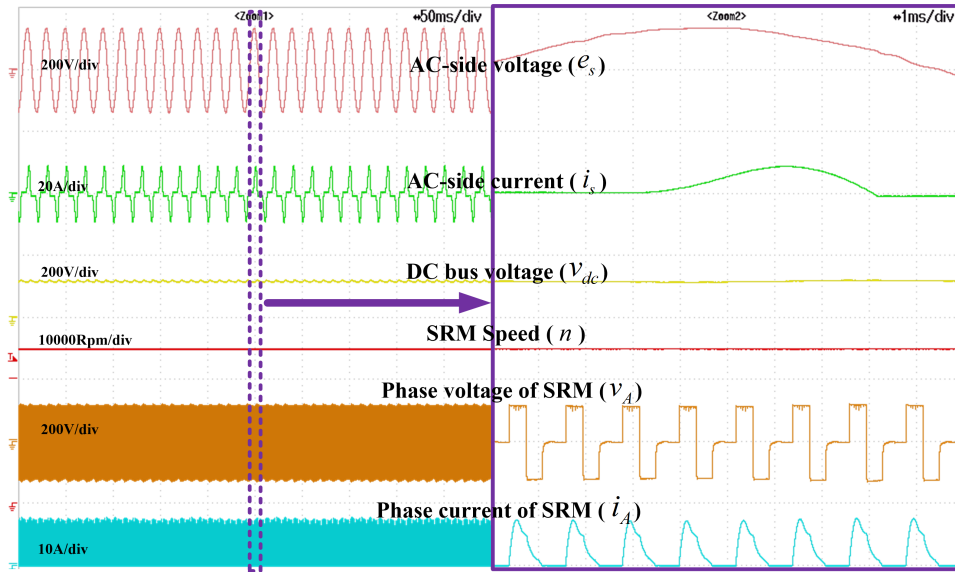
Figure 2.25: Steady-state experiment: at the rated speed of 25000 r/min.

2.5.2 Three-phase DBR-fed SRM drive system

The experiments of three-phase DBR-fed SRM drive system are also implemented on the testbench with the parameters given in Table 2.2. Fig. 2.28 gives out the power factors and efficiencies of the three-phase DBR-fed SRM drive system. In the figures, grid-side active power p, reactive power q, and power factor are denoted by PΣA, QΣA, and $\lambda\Sigma$A, respectively. η_1 denotes efficiency of the front end, namely the efficiency of the three-phase DBR, and η_2 denotes the efficiency of the whole drive topology. There is no switch in the diode rectifier for this drive system, and the power loss caused by the natural commutation is very small. Hence, the

	(a)			(b)			(c)			(d)
P1	0.1283 kw		P1	0.1447 kw		P1	0.1668 kw		P1	0.1899 kw
Q1	0.1089 kvar		Q1	0.1240 kvar		Q1	0.1439 kvar		Q1	0.1696 kvar
S1	0.1683 kVA		S1	0.1906 kVA		S1	0.2203 kVA		S1	0.2546 kVA
I thd1	65.233 %		I thd1	66.503 %		I thd1	67.600 %		I thd1	68.527 %
$\lambda 1$	0.7623		$\lambda 1$	0.7592		$\lambda 1$	0.7571		$\lambda 1$	0.7458
$\eta 1$	88.453 %		$\eta 1$	89.282 %		$\eta 1$	89.960 %		$\eta 1$	90.536 %
$\eta 2$	96.426 %		$\eta 2$	96.675 %		$\eta 2$	96.913 %		$\eta 2$	97.086 %

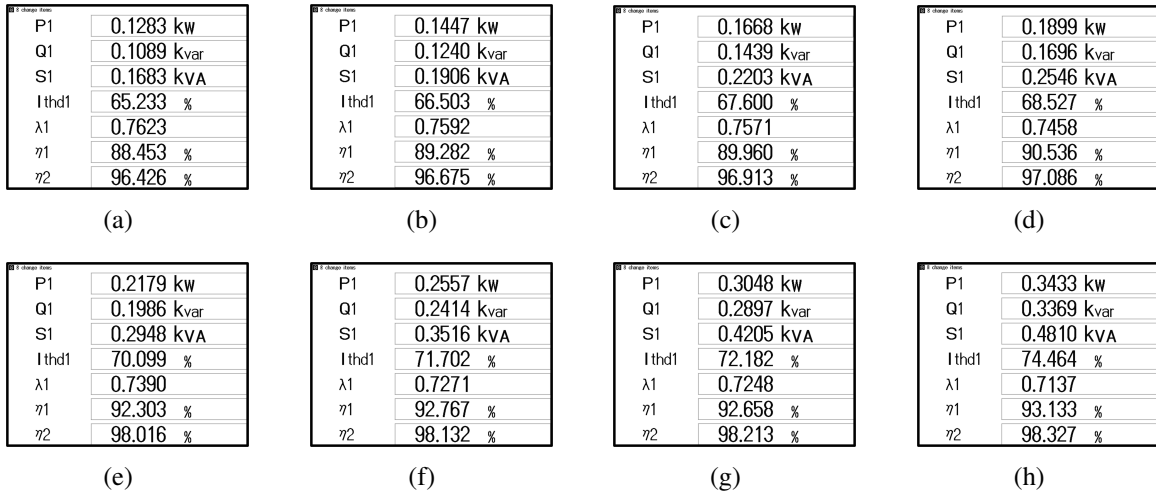		(e)			(f)			(g)			(h)
P1	0.2179 kw		P1	0.2557 kw		P1	0.3048 kw		P1	0.3433 kw
Q1	0.1986 kvar		Q1	0.2414 kvar		Q1	0.2897 kvar		Q1	0.3369 kvar
S1	0.2948 kVA		S1	0.3516 kVA		S1	0.4205 kVA		S1	0.4810 kVA
I thd1	70.099 %		I thd1	71.702 %		I thd1	72.182 %		I thd1	74.464 %
$\lambda 1$	0.7390		$\lambda 1$	0.7271		$\lambda 1$	0.7248		$\lambda 1$	0.7137
$\eta 1$	92.303 %		$\eta 1$	92.767 %		$\eta 1$	92.658 %		$\eta 1$	93.133 %
$\eta 2$	98.016 %		$\eta 2$	98.132 %		$\eta 2$	98.213 %		$\eta 2$	98.327 %

Figure 2.26: Screen captures of Yokogawa power analyzer in single-phase DBR-fed SRM drive system. (a)-(h) 18000 r/min-25000 r/min with the interval of 1000 r/min.
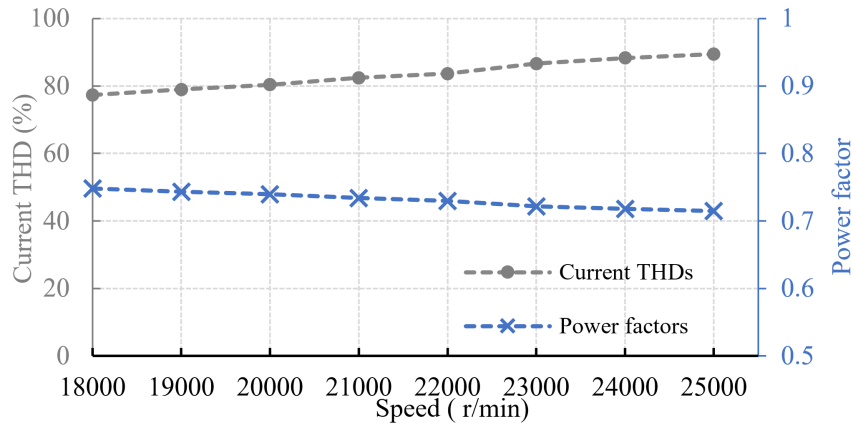

Figure 2.27: Grid-side power factors and current THDs in single-phase DBR-fed SRM drive system.

efficiency of the diode rectifier η_1 is high in Fig. 2.28, which results in high η_2. Nevertheless, a great deal of harmful reactive power $Q\Sigma A$ is brought into the grid because of the distorted grid-side current with phase shift. As summarized in Fig. 2.29, the grid-side current THDs in this three-phase DBR-fed SRM drive system are above 30%, and the power factors are around 0.91 due to the high reactive power.

2.6   Summary

In this chapter, the basics of SRM drive system is first explained in terms of the motor structures, converter topologies, and control algorithms. Then the modified 4/2 SRM with no torque dead zone and with reduced windage loss is described. To drive SRM, DBR is generally adopted as the front end for SRM converter. While the DBR-fed SRM drive system may be simple

Table 2.2: Experimental system parameters of three-phase DBR-fed High-speed SRM drive system

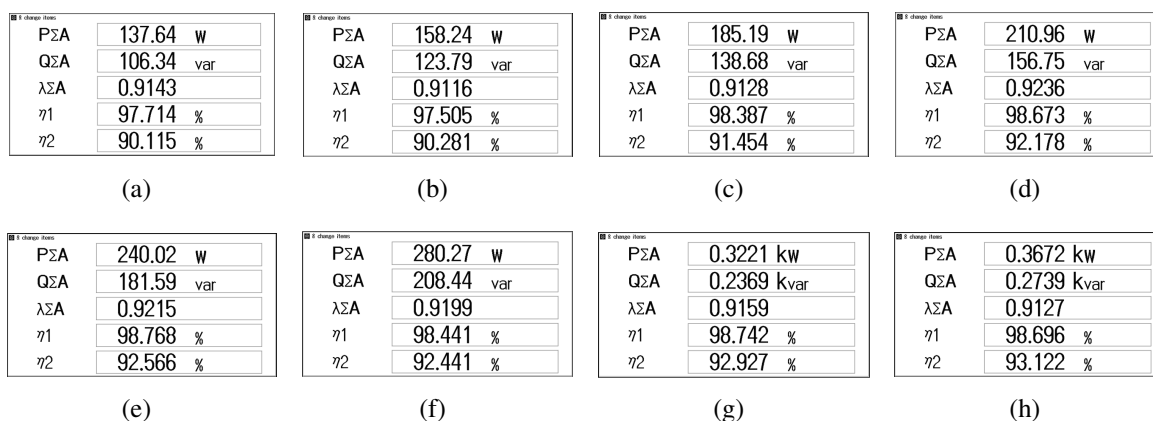| Description	Parameter	Value
Grid-side voltage frequency	$\omega_r(\text{rad/s})$	100π
Grid-side filter resistance	$R_g(\Omega)$	0.3
Grid-side filter inductance	$L_g(\text{mH})$	2
DC-link capacitor	$C(\mu\text{F})$	1360
Control period	$T_s(\mu\text{s})$	50
Rated torque of the high-speed SRM	$\tau_{e,m}(\text{N}\cdot\text{m})$	0.12
Rated speed of the high-speed SRM	$n_r(\text{r/min})$	25000

Figure 2.28: Screenshots of power analyzer in three-phase DBR-fed SRM drive system. (a)-(h) 18000 r/min-25000 r/min with the interval of 1000 r/min.
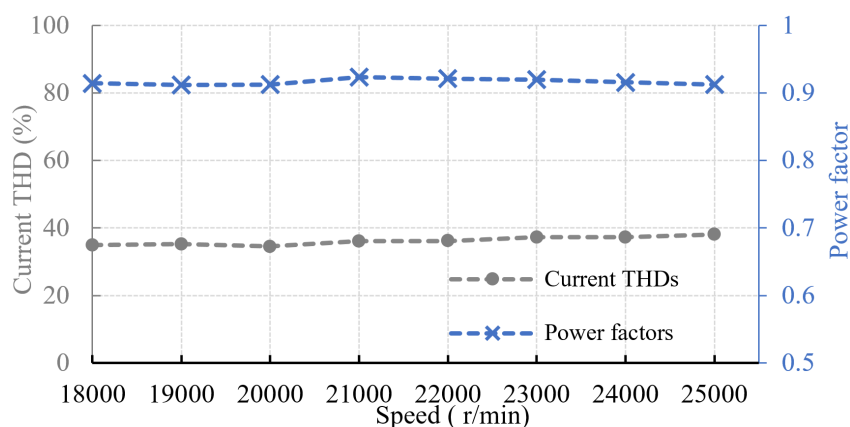
Figure 2.29: Grid-side power factors and current THDs in three-phase DBR-fed SRM drive system.

and cost-effective, it has several disadvantages that limit its applications. The power factor of the system is low due to the presence of reactive power in the input current, which can lead to higher energy consumption and increased operating costs. Besides, the DBR produces high levels of harmonic distortion in the grid, which may disturb other equipments connected to the same power supply. Additionally, the uncontrollable DC-link voltage of DBR can lead to poor motor performance and reduce the system reliability.

CHAPTER 3

Grid-connected high-speed SRM system with fast demagnetization voltage

3.1   Introduction

Power converters play essential roles in the control of SRM. Many topologies are developed to improve the drive performance of SRM. In [55], a converter with a single controllable switch is developed for a specially designed two-phase SRM to cut down the cost. In this converter, the recovered energy stored in the recovery capacitor is circulated back to the DC-link capacitor. In the converter developed in [56], the recovered energy from the main winding is retained and utilized within the motor side instead of being returned to the source, which reduces the capacitor's capacity and the rating of powering devices. However, the converters in [55], [56] have limited application scope because they only can be applied to the two-phase SRM with auxiliary windings for self-starting. Moreover, the freewheeling mode is not available in these converters, which weakens the quality of output torque. In [57], the performance of a novel six-phase SRM converter with minimal number of switches is evaluated. In this converter, the phase winding is connected in series with a diode to avoid the reverse current, and every switch is shared by two adjacent phases. This switch sharing mode brings severe coupling, which results in degraded system performance. In [58], a converter with fast demagnetization ability is researched to extend the speed range of SRM. However, the conventional winding configuration needs to be modified radically to be like an auto-transformer. Some other converters are developed to enhance drive performance with more voltage rails. In [59], a multilevel topology based on a T-type converter is designed, whereas several pairs of conduction mode cannot be realized simultaneously in adjacent excitation phases, for example, double-voltage magnetization mode and double-voltage demagnetization mode; magnetization mode and freewheeling mode. In [34], an asymmetric three-level neutral point diode clamped converter is developed to construct five voltage rails for SRM, yet it is expensive due to the quantity of insulated gate bipolar transistor (IGBT) and diode. The capacitive energy recovery converters creating new

voltage rail by extra boost capacitor are also developed to realize fast demagnetization for SRM in [33, 60–62]. The energy freewheels into the boost capacitor in the demagnetization process, and in later energization process, the boost capacitor is discharged. The voltage on the boost capacitor is allowed to rise quickly, which increases the turn-off voltage and consequently decreases the turn-off time. Hence, the advance angle can be reduced, which generates the same output power more efficiently. Alternatively, the higher output power can be achieved for the same advance angle. However, the energy flow path must be adequately designed to prevent the boost capacitor from being overcharged. In [60], a 4-level converter is developed. The energy stored in the boost capacitor can accelerate the magnetizing and demagnetizing process, but two situations must be avoided, namely, the energy in boost capacitor is emptied by the magnetizing process, and no current flows back to recovery capacitor due to the overlap of conduction region of adjacent phases. Moreover, inter-phase coupling does exist in this topology. The above two problems are solved in the converter developed in [61] by adopting two boost capacitors, but the demagnetizing voltage is still not stable and varies in different operating conditions. In [62], the voltage of the boost capacitor can be clamped to the DC-link voltage by a diode, yet there still is a mutual coupling between the conduction mode of adjacent phases.

SRM converters are generally fed by a DC power supply or by a DBR that takes AC source as input. Given the manufacture cost, the DBR is frequently adopted. Nevertheless, the performance decays due to the uncontrolled DC-link voltage and degraded power quality, as has been presented in Chapter 2. Some topologies are proposed to improve the power quality of the SRM drive system. In [12], an additional switch and diode are added before the asymmetric half-bridge converter to form a new topology. The power factors are improved, but the grid-side current THDs are not ideal. In [63], a Vienna-based power factor correction converter is adopted to drive the SRM. To keep the capacitor voltage balanced, the speed and loads must always be the same for the upper and lower motor. Besides the above, the DC-DC circuits are also developed as the front end for the SRM converter. Modified based on the Vienna converter, the circuit in [27] is presented, which comprises two Cuk converters with a common switch. In [20], a single-phase boost-type switch-mode rectifier is proposed to drive the SRM. Satisfying power quality is obtained, but the magnetization and demagnetization mode of the proposed topology are not decoupled, which limits the control flexibility. Although the front ends above have been developed to drive the SRM with corrected power factor, the energy in them cannot be fed back to gird during speed regulation.

In this chapter, a SRM drive topology, which is composed of a T-type single-phase VSR and a 4-level SRM converter, is proposed. With the 4-level SRM converter, fast demagnetization is achieved, which significantly reduces the current tailing time of the high-speed SRM. Moreover, a control strategy that regulates the VSR and SRM simultaneously by controlling the grid-side d and q-axis current is proposed. Additionally, bidirectional energy flow can be realized.

3.2   Proposed drive topology and mathematical model

The proposed drive topology composed of a T-type single-phase three-level VSR and a 4-level SRM converter is shown in Fig. 3.1.
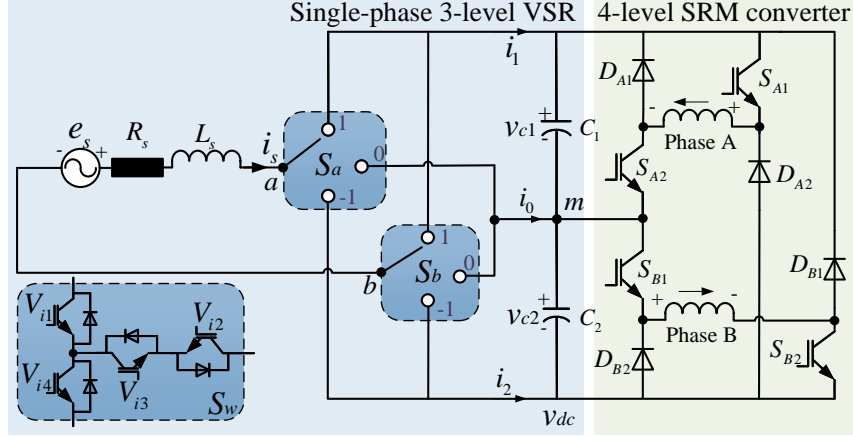
Figure 3.1: Proposed drive topology for high-speed SRM.

3.2.1 Front-end single-phase three-level VSR

The T-type single-phase VSR is adopted as the front end for the 4-level SRM converter in the proposed topology. The resistance, filter inductance, DC-link current, DC-link voltage, the voltage of capacitor C_1 and C_2 are denoted by R_s, L_s, i_{dc}, v_{dc}, v_{c1} and v_{c2}, respectively. The grid-side voltage, grid-side current, and rectifier voltage are represented by e_s, i_s, and u_s, respectively. There are two single-pole triple-throw switching unites in this topology, namely S_a and S_b. The switching state of S_w, $w \in \{a, b\}$ can be controlled by setting V_{i1}, V_{i2}, V_{i3}, and V_{i4} to the proper state

$$S_w = \begin{cases} +1 & V_{i1} \text{ On}, V_{i2} \text{ On}, V_{i3} \text{ Off}, V_{i4} \text{ Off} \\ 0 & V_{i2} \text{ On}, V_{i3} \text{ On}, V_{i1} \text{ Off}, V_{i4} \text{ Off} \quad w \in \{a, b\} \\ -1 & V_{i3} \text{ On}, V_{i4} \text{ On}, V_{i1} \text{ Off}, V_{i2} \text{ Off}. \end{cases} \tag{3.1}$$

Suppose v_{c1} and v_{c2} are well balanced, both point a and point b can be arbitrarily connected to $+\frac{v_{dc}}{2}$, 0, and $-\frac{v_{dc}}{2}$ by setting S_w to the state of 1, 0, and -1, respectively. Therefore, the rectifier voltage u_s can be described by

$$u_s = u_{am} - u_{bm} = \frac{S_a (S_a + 1) - S_b (S_b + 1)}{2} v_{c1}$$
$$- \frac{S_a (S_a - 1) - S_b (S_b - 1)}{2} v_{c2}. \tag{3.2}$$

The power in VSR follows the equation below

$$u_s i_s = v_{c1} i_1 - v_{c2} i_2 \tag{3.3}$$

where i_1 and i_2 represent the DC-link current shown in Fig. 1. Based on Kirchhoff's voltage law, the voltage equation of single-phase VSR can be given by

$$\frac{di_s}{dt} = \frac{1}{L_s} (e_s - R_s i_s - u_s). \tag{3.4}$$

(a) $\boldsymbol{u}_1(1, -1)$ (b) $\boldsymbol{u}_2(1, 0)$ (c) $\boldsymbol{u}_3(0, -1)$

(d) $\boldsymbol{u}_4(1, 1)$ (e) $\boldsymbol{u}_5(0, 0)$ (f) $\boldsymbol{u}_6(-1, -1)$

(g) $\boldsymbol{u}_7(0, 1)$ (h) $\boldsymbol{u}_8(-1, 0)$ (i) $\boldsymbol{u}_9(-1, 1)$
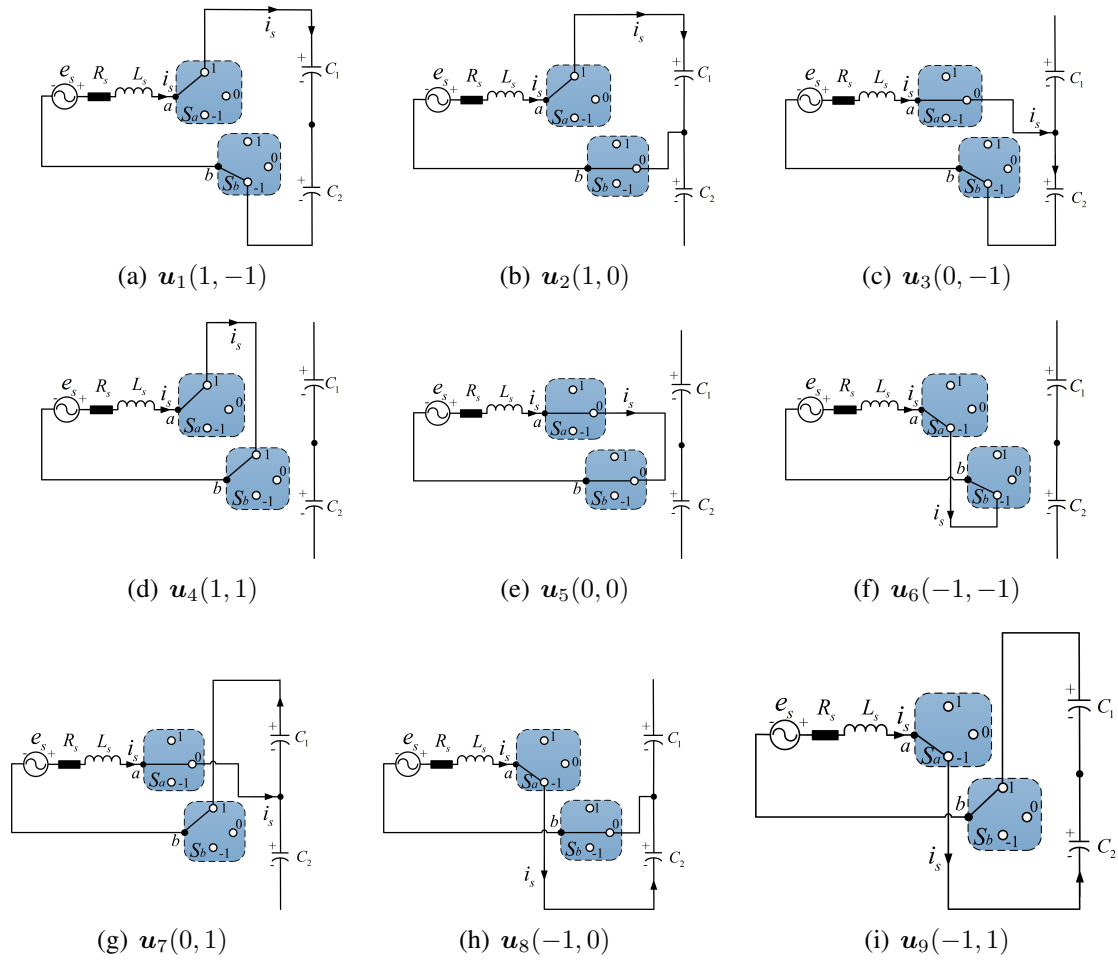
Figure 3.2: The charging and discharging modes of the two capacitors under the effect of the nine switching states.

There are nine switching states (S_a, S_b) in the single-phase VSR, and different rectifier voltages u_s can be obtained by applying these switching states on the VSR. For a better description, the nine base switching-state vectors, representing the rectifier voltage in two-dimensional $\alpha\beta$ stationary frame, are defined and shown in Fig. 3.3, and their corresponding regulation effect on capacitor voltages are presented in Fig. 3.2. The specific definitions of these vectors are described as follows:

- Base vector $\boldsymbol{u}_1(1, -1)$ is defined as the large positive vector, whose amplitude and space angle are v_{dc} and $0°$, respectively.

- Base vector $\boldsymbol{u}_2(1, 0)$ and $\boldsymbol{u}_3(0, -1)$ are redundant small positive vectors for each other, whose amplitude and space angle are both $\frac{v_{dc}}{2}$ and $0°$, respectively.

- Base vector $\boldsymbol{u}_4(1, 1)$, $\boldsymbol{u}_5(0, 0)$, and $\boldsymbol{u}_6(-1, -1)$ are redundant zero vectors for one another, whose amplitude and space angle are all 0 and $0°$, respectively.

- Base vector $\boldsymbol{u}_7(0, 1)$ and $\boldsymbol{u}_8(-1, 0)$ are redundant small negative vectors for each other, whose amplitude and space angle are both $-\frac{v_{dc}}{2}$ and $180°$, respectively.

- Base vector $\boldsymbol{u}_9(-1, 1)$ is defined as the large negative vector, whose amplitude and space angle are $-v_{dc}$ and $180°$, respectively.

Table 3.1: $\boldsymbol{u}_i$ and $\boldsymbol{u}_j$ in each section

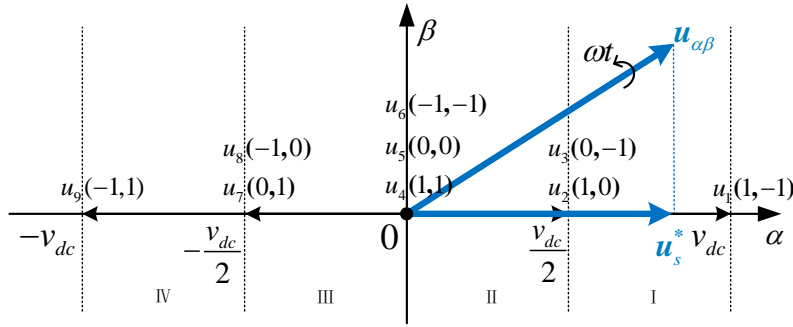|		Sector I	Sector II	Sector III	Sector IV
$\boldsymbol{u}_i$	$\boldsymbol{u}_{i+}$	$\boldsymbol{u}_2(1,0)$	$\boldsymbol{u}_2(1,0)$	$\boldsymbol{u}_8(-1,0)$	$\boldsymbol{u}_8(-1,0)$
	$\boldsymbol{u}_{i-}$	$\boldsymbol{u}_3(0,-1)$	$\boldsymbol{u}_3(0,-1)$	$\boldsymbol{u}_7(0,1)$	$\boldsymbol{u}_7(0,1)$
$\boldsymbol{u}_j$		$\boldsymbol{u}_1(1,-1)$	$\boldsymbol{u}_5(0,0)$	$\boldsymbol{u}_5(0,0)$	$\boldsymbol{u}_9(-1,1)$

Figure 3.3: Base vectors and sector division.

Suppose $\boldsymbol{u}_s^* = [u_\alpha, 0]^{\mathrm{T}}$ is the desired rectifier voltage that needs to be synthesized by SVPWM. Based on the theory of volt-second balance, the effect of $\boldsymbol{u}_s^*$ during a control period T_c is equivalent to

$$
\begin{cases}
\boldsymbol{u}_s^* T_c = \boldsymbol{u}_i T_i + \boldsymbol{u}_j T_j \\
T_c = T_i + T_j
\end{cases}
\quad \boldsymbol{u}_i, \boldsymbol{u}_j \in \{\boldsymbol{u}_1, \boldsymbol{u}_2 \ldots \boldsymbol{u}_9\}
\tag{3.5}
$$

where T_i and T_j denote the dwell time of base vector $\boldsymbol{u}_i$ and $\boldsymbol{u}_j$, respectively. $\boldsymbol{u}_i$ and $\boldsymbol{u}_j$ can be decided by identifying the sector where $\boldsymbol{u}_s^*$ locates, which is shown in Table 3.1. Then, T_i and T_j can be calculated by bringing $\boldsymbol{u}_i, \boldsymbol{u}_j$, and $\boldsymbol{u}_s^*$ into (3.5). Both the redundant base vector $\boldsymbol{u}_{i+}$ and $\boldsymbol{u}_{i-}$ are used in modulation for capacitor balancing control. For a better explanation, the voltage difference between v_{c1} (voltage of the upper capacitor C_1) and v_{c2} (voltage of the lower capacitor C_2) is defined as Δv_c, i.e., $\Delta v_c = v_{c1} - v_{c2}$, and the effect of every switching state on Δv_c is listed in Table 3.2. It can be found that Δv_c not only depends on the switching states but depends on the polarity of grid-side current i_s, namely, sign (i_s). For the same i_s, the redundant vectors $\boldsymbol{u}_2(1,0)$ and $\boldsymbol{u}_3(0,-1)$ have the opposite impact on Δv_c. Besides, for $\boldsymbol{u}_2(1,0)$ (or $\boldsymbol{u}_3(0,-1)$), its impacts on Δv_c is opposite when $i_s > 0$ and $i_s < 0$. The redundant vectors $\boldsymbol{u}_8(-1,0)$ and $\boldsymbol{u}_7(0,1)$ have the same impact on Δv_c as $\boldsymbol{u}_2(1,0)$ and $\boldsymbol{u}_3(0,-1)$, respectively. Therefore, capacitor balancing can be maintained by adjusting the dwell time of the above two pairs of redundant vectors. Generally, a PI controller taking Δv_c as input is used for capacitor balancing control, and its output is the impact factor f, which adjusts the dwell time of $\boldsymbol{u}_{i+}$ and $\boldsymbol{u}_{i-}$ by

$$\begin{cases} T_{i+} = \frac{1-\text{sign}(i_s)\cdot f}{2} T_i \\ T_{i-} = \frac{1+\text{sign}(i_s)\cdot f}{2} T_i \\ T_{i+} + T_{i-} = T_i \end{cases} \tag{3.6}$$

where $-1 \le f \le 1$. In capacitor balancing control, the polarity of i_s should be evaluated firstly. Then T_{i+} and T_{i-} should be adjusted according to f. It can be found from (3.6) and Table 3.2 that Δv_c will decrease if $f > 0$, yet Δv_c will increase if $f < 0$. The dynamic regulation of f can effectively keep the capacitors balanced without causing any effect on the modulation of $\boldsymbol{u}_s^*$ during the operation of VSR.

Table 3.2: The effect of base voltage vectors on Δv_c

	$\boldsymbol{u}_1(1,-1)$	$\boldsymbol{u}_2(1,0)$	$\boldsymbol{u}_3(0,-1)$	$\boldsymbol{u}_4(1,1)$	$\boldsymbol{u}_5(0,0)$	$\boldsymbol{u}_6(-1,-1)$	$\boldsymbol{u}_7(0,1)$	$\boldsymbol{u}_8(-1,0)$	$\boldsymbol{u}_9(-1,1)$
$\Delta v_c\,(i_s > 0)$	×	↑	↓	×	×	×	↓	↑	×
$\Delta v_c\,(i_s < 0)$	×	↓	↑	×	×	×	↑	↓	×

3.2.2 Back-end 4-level SRM converter

In the drive topology, a 4-level SRM converter is constructed based on the conventional split-DC converter to connect to the end of the VSR with dual output voltage. It has four conduction modes, namely, magnetization mode (denoted as 1), freewheeling mode (denoted as 0), demagnetization mode (denoted as -1), and double-voltage demagnetization mode (denoted as -2). The conduction mode combinations of the two phases of the 4-level SRM converter are illustrated in Fig. 3.4. There are two switches and two diodes in each phase, and the two phases are connected in parallel on DC-link. No common switch is adopted in this converter. Given the high back-EMF in phase winding, single pulse control (SPC) is adopted for high-speed SRM control in this system. The magnetization mode and double-voltage demagnetization mode are analyzed as examples.

1) Magnetization mode:

When S_{p1} and $S_{p2}, p \epsilon \{A, B\}$ are switched on, the capacitor voltage v_c is applied to the winding of phase p. Supposing the capacitor voltages on DC-link are well balanced (namely, $v_{c1} = v_{c2} = v_c$), the voltage and current equations of this mode are given by

$$\begin{cases} v_m = v_c = r_m i_m + L_m(i_m, \theta_r)\frac{\partial i_m}{\partial t} + \frac{\partial L_m(i_m,\theta_r)}{\partial \theta_r}\omega_r i_m \\ i_m(t) = I_{p1\_ini}\, e^{-t/\tau_a} + \frac{v_c}{R_{eq\_m}}(1 - e^{-t/\tau_a}) \\ R_{eq\_m} = r_m + \partial L_m(i_m, \theta_r)\omega_r/\partial\theta_r \\ \tau_a = L_m\,(i_m, \theta_r)/R_{eq\_m} \end{cases} \tag{3.7}$$

where $v_m, i_m, r_m, L_m, I_{p1\_ini}$, and ω_r denote phase voltage, current, resistance, inductance, initial current, and angular velocity of SRM, respectively. Regularly, the energy stored in phase winding is fully released at the end of every stroke, thus $I_{p1\_ini} = 0$.

2) Double-voltage demagnetization mode:

When S_{p1} and S_{p2} are switched off, a reversed DC-link voltage equaling to $-2v_c$ is applied to the winding of phase p and the mathematical model of this mode are given by

$$\begin{cases} v_m = -2\,v_c = r_m\,i_m + L_m(i_m, \theta_r)\frac{\partial i_m}{\partial t} + \frac{\partial L_m(i_m, \theta_r)}{\partial \theta_r}\omega_r i_m \\ i_m(t) = I_{p2\_ini}\,e^{-t/\tau_a} - \frac{2v_c}{R_{eq\_m}}(1 - e^{-t/\tau_a}) \end{cases} \tag{3.8}$$

where I_{p2_ini} is the initial current in winding at the start of this mode. For high-speed SRM, fast demagnetization is extremely important for the reduction of current tailing time, which contributes to negative torque elimination.

The double-voltage demagnetization mode in this converter can be performed entirely. The energy flow of any phase in this converter will not be affected by the conduction mode of the other phases, which means fully inter-phase control independence has been realized. If some advanced control schemes are going to be applied to this converter, all its conduction modes can be performed flexibly to realize accurate current regulation.

The conduction mode combinations of conventional type of SRM converter featured with split DC-link, i.e., the split-DC converter, are presented in Fig. 3.5. Just two conduction modes can be applied to the SRM for this converter, namely, the magnetization mode (denoted as 1) and demagnetization mode (denoted as -1). Compared with the conventional split-DC converter, the 4-level SRM converter has two more conduction modes, and the newly constructed double-voltage demagnetization mode is of great importance for high-speed SRM drive. For high-speed SRM, the current drops very slowly due to the high rotational speed after being switched off. In order to reduce the tailing time of the demagnetization current of the high-speed SRM, it is vital to accelerate the current decreasing process by the fast demagnetization with $-2v_p$.

3.3 Integrated current control strategy based on virtual orthogonal system

3.3.1 Overall system descriptions

The proposed control system for high-speed SRM is presented in Fig. 3.6. The encoder signals are sent to position/velocity estimator for position and velocity estimation. If rotor locates in the conduction region of a phase, two switches of the corresponding phase are turned on together for energizing; if not, the switches are turned off together so that the double-voltage demagnetization mode $(-2v_c)$ can be applied to winding for fast demagnetization. The demagnetization mode $(-v_c)$ is implemented in the 4-level SRM converter to achieve strict over-current protection.

From the conventional point of view, if the SPC were adopted, the motor speed can be adjusted by regulating the DC-link voltage of VSR. As is known to all that the DC-link voltage
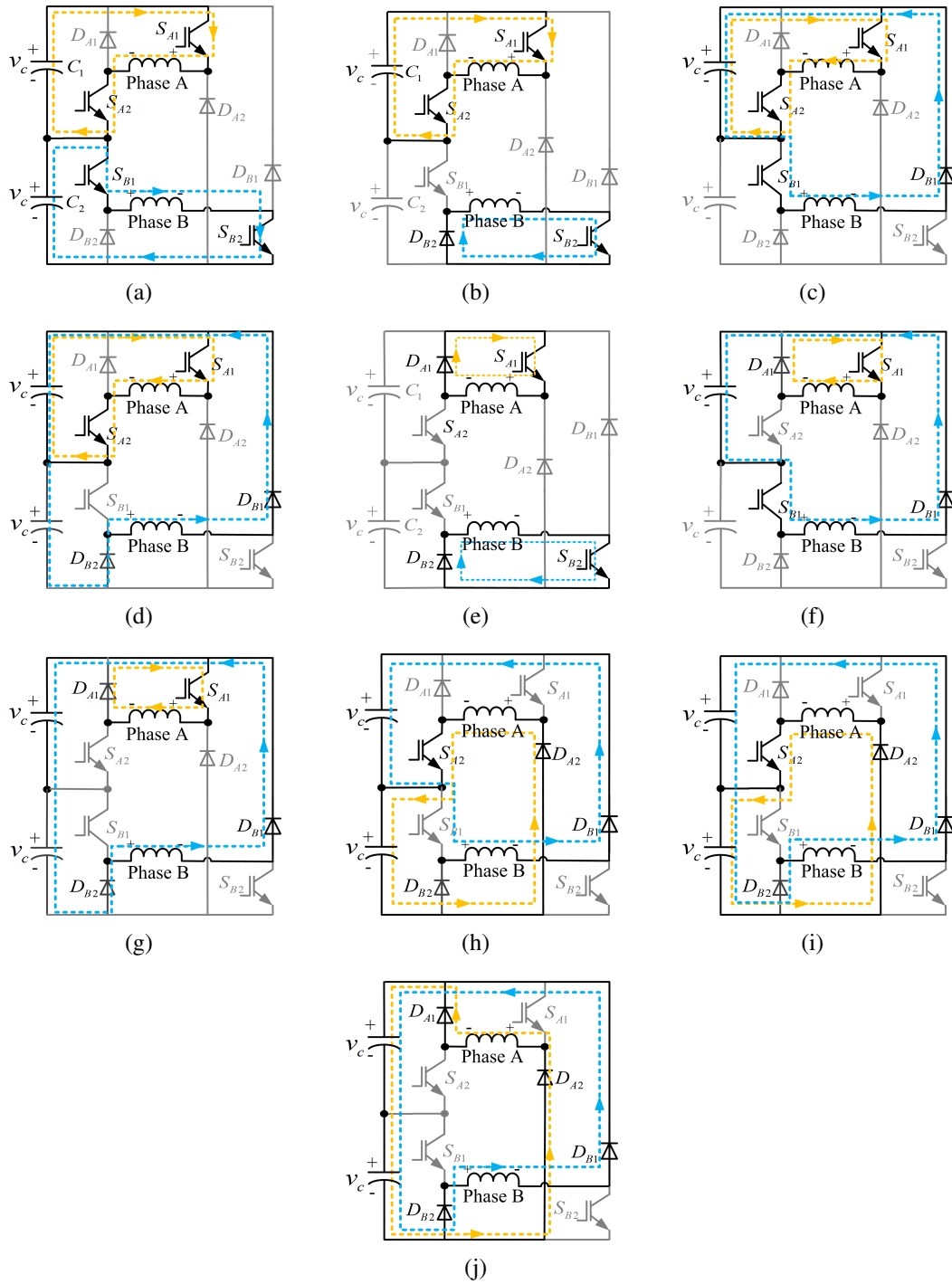
Figure 3.4: Conduction modes combinations in 4-level SRM converter. (a) (1,1). (b) (1,0). (c) (1,-1). (d) (1,-2). (e) (0,0). (f) (0,-1). (g) (0.-2). (h) (-1,-1). (i) (-1,-2). (j) (-2,-2).

can be governed by manipulating i_d. That means the speed can be regulated by controlling DC-link voltage, during which process the DC-link voltage is regulated by controlling the i_d of VSR. It is a rather complicated system because there are three control loops, i.e., speed control loop, DC-link voltage control loop, and i_d control loop. The implementation of this hypothetical
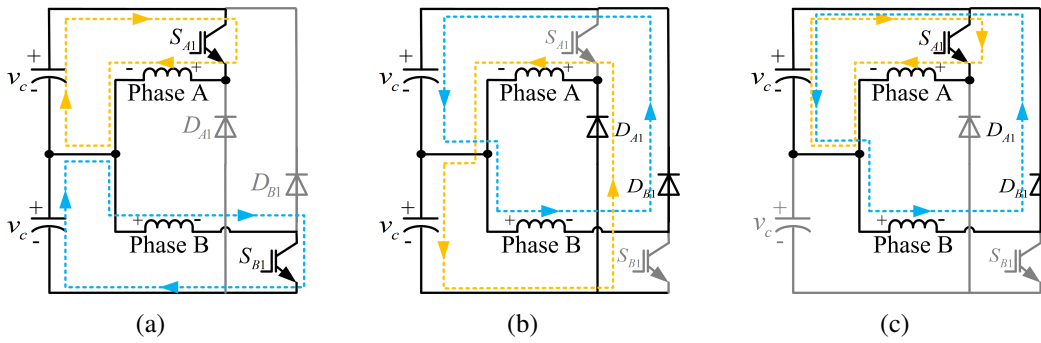
Figure 3.5: Conduction modes combinations in conventional split-DC converter. (a) (1,1). (b) (-1,-1). (c) (1,-1).
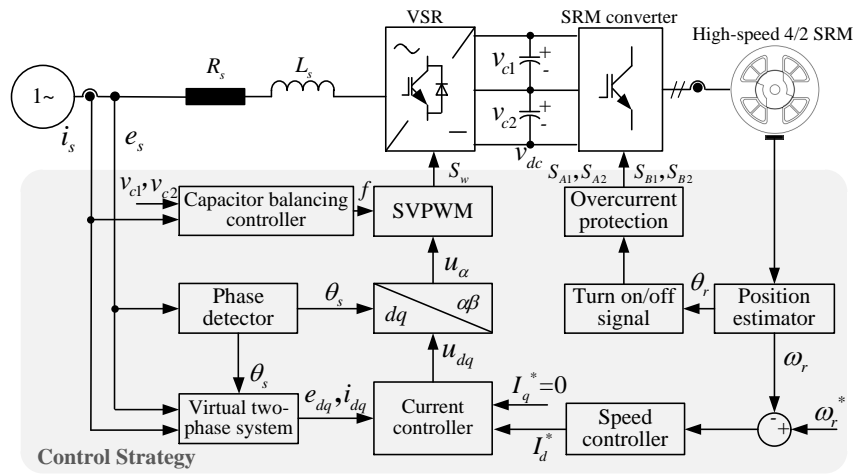

Figure 3.6: Proposed control system for high-speed SRM drive system based on 4-level SRM converter.

method brings a very complicated parameter tuning process. In the proposed control strategy, the motor speed is directly governed by manipulating i_d, so the output of the speed PI controller is the reference of the d-axis component of grid-side current (I_d^*). I_d^* can be either positive or negative due to the bidirectional energy flow ability of the drive topology, which means the energy not only can flow from the grid to the SRM but can flow back to the grid. The reference of q-axis component of grid-side current (I_q^*) is set to zero for power factor correction. The current decoupled strategy based on feedforward control is adopted to track I_d^* and I_q^* in the proposed system. As a result, motor speed, grid-side power factor, and grid-side current THDs in the system can be regulated simultaneously through the decoupling control of grid-side current. That is to say, an integrated control strategy that controls the front-end VSR and the SRM together by one algorithm has been realized.

3.3.2 Current control strategy

In the three-phase VSR system, the AC quantities is converted into DC quantities by transforming the variables from abc stationary reference frame to orthogonal $\alpha\beta$ reference frame then

to dq synchronous reference frame. Afterward, based on the controller designed in dq frame, satisfying control performance can be obtained. However, this method is not readily applicable to the single-phase VSR because only the one-phase variables are available in the single-phase VSR, yet the dq transformation needs two orthogonal variables.

In order to control the single-phase VSR in the same way as the three-phase VSR, a virtual phase whose variables are orthogonal to those of the single-phase system is created. Then the overall system can be easily represented in $\alpha\beta$ reference frame, within which the original grid-side variables ξ_s are considered as the α-axis component of the vector $\xi_{\alpha\beta} = [\xi_\alpha, \ \xi_\beta]^{\mathrm{T}}$ and the β-axis component ξ_β is obtained by a $\pi/2$ lag of its corresponding original grid-side variables ξ_s. Then, the voltage equation of the virtual two-phase system can be expressed as

$$\boldsymbol{e}_{\alpha\beta} = R_s \boldsymbol{i}_{\alpha\beta} + L_s \frac{d\boldsymbol{i}_{\alpha\beta}}{dt} + \boldsymbol{u}_{\alpha\beta}. \tag{3.9}$$

With the Park transformation

$$\boldsymbol{\xi}_{dq} = \begin{bmatrix} \cos\theta_s & \sin\theta_s \\ -\sin\theta_s & \cos\theta_s \end{bmatrix} \boldsymbol{\xi}_{\alpha\beta}, \tag{3.10}$$

(3.9) can be transformed into

$$L_s \frac{d\boldsymbol{i}_{dq}}{dt} = \boldsymbol{e}_{dq} + \begin{bmatrix} -R_s & \omega_s L_s \\ -\omega_s L_s & -R_s \end{bmatrix} \boldsymbol{i}_{dq} - \boldsymbol{u}_{dq} \tag{3.11}$$

where $\boldsymbol{\xi}_{dq} = [\xi_d, \xi_q]^{\mathrm{T}}$, $\theta_s = \omega_s t$ is the angle between the α-axis and d-axis in the virtual two-phase orthogonal system, and ω_s is the fundamental frequency. A coefficient S_d [64], which represents the ratio between u_d and DC-link voltage, is defined as

$$S_d = \frac{u_d}{v_{dc}}. \tag{3.12}$$

It can be seen from (3.11) that there is a coupling between i_d and i_q, which increases the design complexity of the controller. For the sake of decoupling, current feedforward control is adopted and two intermediate variables, i.e. u_{cd}^* and u_{cq}^* should be defined

$$u_{cd}^* = L_s \frac{di_d}{dt} + R_s i_d \tag{3.13}$$

$$u_{cq}^* = L_s \frac{di_q}{dt} + R_s i_q \tag{3.14}$$

where u_{cd}^* and u_{cq}^* can be obtained by the PI controllers of i_d and i_q, respectively. After bringing (3.13) and (3.14) into (3.11), the rectifier voltage u_{dq} in dq reference frame can be given by

$$
\begin{aligned}
u_d &= e_d + \omega_s L_s i_q - u_{cd}^* \\
u_q &= e_q - \omega_s L_s i_d - u_{cq}^*.
\end{aligned}
\tag{3.15}
$$

With I_d^* and I_q^*, the rectifier voltage $\boldsymbol{u}_{dq}$ can be obtained by the decoupled current feedback control. Then, $\boldsymbol{u}_{dq}$ is transformed back to $\alpha\beta$ reference frame to obtain u_α, which belongs to the original single-phase phase. Finally, u_α is fed into the SVPWM block for drive signal production, and u_β that belongs to the virtual β phase is discarded. With the constructed virtual β phase, the AC quantities of the original single-phase system are transformed into DC quantities in dq reference frame to obtain the control signal of the original single-phase system.

3.3.3 Enhancement of current THDs and power factors

The THD is defined as the ratio of the equivalent RMS current of all the harmonic frequencies (from the 2 nd harmonic on) over the RMS current of the fundamental frequency:

$$
\text{THD} = \frac{\sqrt{\sum_{n=2}^{\infty} I_{n\_rms}^2}}{I_{fund\_rms}}
\tag{3.16}
$$

where I_{n_rms} and I_{fund_rms} are the RMS current of the nth harmonic and the fundamental frequency, respectively. In the proposed system, the grid-side current THDs are reduced by controlling the d-axis and q-axis components of grid-side current to be constant in the decoupled current control strategy. The variables in $\alpha\beta$ reference frame can be derived by applying the inverse Park transformation matrix to the corresponding variables in the synchronous dq reference frame

$$
\boldsymbol{\xi}_{\alpha\beta} =
\begin{bmatrix}
\cos\theta_s & -\sin\theta_s \\
\sin\theta_s & \cos\theta_s
\end{bmatrix}
\boldsymbol{\xi}_{dq}.
\tag{3.17}
$$

Thus, the original grid-side current i_s ($i_s = i_\alpha$) can be written as

$$
i_s = \cos(\omega_s t) i_d - \sin(\omega_s t) i_q.
\tag{3.18}
$$

If i_d and i_q of the virtual orthogonal two-phase system are constant, i_s can be rewritten as

$$
\begin{aligned}
i_s &= \sqrt{i_d^2 + i_q^2}\left(\cos(\omega_s t)\frac{i_d}{\sqrt{i_d^2 + i_q^2}} - \sin(\omega_s t)\frac{i_q}{\sqrt{i_d^2 + i_q^2}}\right) \\
&= \sqrt{i_d^2 + i_q^2}\left(\cos(\omega_s t)\cos\varphi - \sin(\omega_s t)\sin\varphi\right) \\
&= K\cos(\omega_s t + \varphi)
\end{aligned}
\tag{3.19}
$$

where $K = \sqrt{i_d^2 + i_q^2}$ and $\varphi = \arctan\left(\frac{i_q}{i_d}\right)$. It can be seen from (3.19) that i_s is a standard sinusoidal curve, whose frequency is the fundamental frequency ω_s. In this case, THDs are

around zero because $I_{n\_rms} = 0$ in (3.16). Therefore, by controlling i_d and i_q to be constant in the system, i_s can be a standard sinusoidal curve with low THDs.

This system realizes the integrated control of VSR and SRM, within which the motor speed is regulated by i_d. In steady-state condition, the output of speed PI controller, i.e., reference of d-axis component of grid-side current I_d^*, is a constant, and reference of q-axis component of grid-side current $I_q^* = 0$ is set in the system for power factor correction. That means the THDs can be well controlled if i_d and i_q can successfully trace their references in the current feed-forward algorithm. Because i_d control loop is a stable first-order inertial element, and fast response can always be ensured by setting a proper cross-over frequency. The block diagram of i_q control loop has the same form as that of the i_d control loop, and they use the same control parameters. Therefore, low current THDs can be obtained in this system.

Power factor is related to the displacement factor $\cos\varphi$ and the quotient of the RMS value of fundamental current divided by the total RMS value [65]

$$\text{Power factor } = \frac{I_{fund_rms}}{\sqrt{\sum_{n=1}^{\infty} I_{n-rms}^2}} \cos\varphi. \tag{3.20}$$

As can be seen, the regulated low reactive power and low THDs contribute to favorable power factors. In the instantaneous power theory, the real power $p(t)$ and reactive power $q(t)$ can be expressed as

$$\begin{pmatrix} p(t) \\ q(t) \end{pmatrix} = \frac{3}{2} \begin{bmatrix} e_\alpha(t) & e_\beta(t) \\ e_\beta(t) & -e_\alpha(t) \end{bmatrix} \begin{pmatrix} i_\alpha(t) \\ i_\beta(t) \end{pmatrix}. \tag{3.21}$$

Applying Park transformation to 3.21 gives

$$\begin{pmatrix} i_d(t) \\ i_q(t) \end{pmatrix} = \frac{2}{3e_d(t)} \begin{pmatrix} p(t) \\ q(t) \end{pmatrix}. \tag{3.22}$$

It can be seen from above that the reactive power depends on i_q, and low reactive power can be are obtained by further regulating the q-axis current to the value near zero. Consequently, near-unity power factors can also be obtained in the proposed system.

3.3.4 System transfer function

The control block diagram of the d-axis component of grid-side current can be drawn as the highlighted part of Fig. 3.7, which is the control block diagram of the proposed high-speed SRM drive system.

The open-loop transfer function of i_d control loop is given by

$$G_{cc}(s) = \frac{sK_{cp} + K_{ci}}{s} \cdot \frac{1}{sL_s + R_s} \tag{3.23}$$

where K_{cp} and K_{ci} are the proportional and integral gains for the current PI controller. By designing $\frac{K_{ci}}{R_s} = \frac{K_{cp}}{L_s}$, the closed-loop transfer function of i_d control loop can be simplified as

$$\Phi_{cc}(s) = \frac{i_d(s)}{I_d^*(s)} = \frac{sK_{cp} + K_{ci}}{L_s s^2 + sR_s + sK_{cp} + K_{ci}} = \frac{1}{T_{cc}s + 1} \tag{3.24}$$
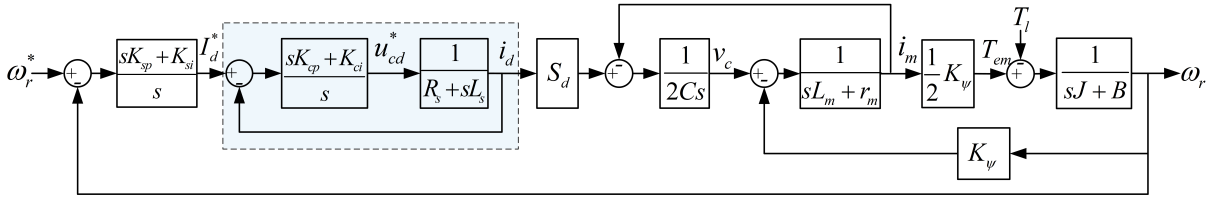
Figure 3.7: Block diagram of the high-speed SRM drive system based on 4-level SRM converter.

where $T_{cc} = \frac{L_s}{K_{cp}} = \frac{1}{\omega_{cc}}$ is the time constant of this first-order inertial element and ω_{cc} is the cross-over frequency. Applying Kirchhoff's current law to the drive topology in Fig. 3.1 gives

$$i_m + C\frac{dv_{dc}}{dt} = S_d i_d \tag{3.25}$$

where $C = C_1 = C_2$, $S_d \epsilon (0, 1)$ is the equivalent coefficient and can be regarded as a constant in steady state [64], and i_m is the winding current. The expression of voltage and electromagnetic torque of SRM [66] can be given by

$$v_c = r_m i_m + L_m \frac{di_m}{dt} + K_\psi \omega_r \tag{3.26}$$

$$T_{em} = \frac{1}{2} K_\psi i_m \tag{3.27}$$

where $K_\psi = \frac{d\psi_m}{d\theta_r}$, and ψ_m, r_m, L_m, T_{em}, and ω_r denote flux linkage, resistance, inductance, electromagnetic torque, and angular velocity of SRM, respectively. Moreover, the relationship between electromagnetic torque and angular velocity is given by

$$T_{em} = T_l + B\omega_r + J\frac{d\omega_r}{dt} \tag{3.28}$$

where T_l, J, and B represent load torque, moment of inertia, and viscous friction coefficient, respectively. Then, given the value of the system parameters, the open-loop transfer function of the proposed control strategy can be written as

$$G_{sc}(s) = K_{sp}\frac{\tau_{si}s + 1}{\tau_{si}s}\frac{1}{T_{cc}s + 1}\frac{1}{T_w s} \tag{3.29}$$

where K_{sp} and τ_{si} are the proportional gain and integral time constant of the speed controller, respectively, and $T_w = (2CK_\psi{}^2 + 2J)/S_d K_\psi.K_{sp}$ and τ_{si} can be chosen in accordance with the "symmetrical optimum" [67], which is a standard design procedure for transfer functions containing a double integration. Its main idea is to choose the cross-over frequency at the geometric mean of the two corner frequencies, to obtain maximum phase margin, which in turn will result in optimum damping of the speed loop. By normalizing with

$$\tau_{si} = \delta^2 T_{cc}, \quad \delta > 1 \tag{3.30}$$

the cross-over frequency ω_{cs} of $G_{sc}(s)$ can be written as

$$\omega_{cs} = \frac{1}{\sqrt{\tau_{si} T_{cc}}} = \frac{1}{\delta T_{cc}} \tag{3.31}$$

From the cross-over condition $|G_{sc}(j\omega_{cs})| = 1$, the gain of the speed controller can be given by

$$K_{sp} = \frac{T_w}{\delta T_{cc}}. \tag{3.32}$$

The closed-loop transfer function can be written as

$$\Phi_{sc}(s) = \frac{K_{sp}\tau_{si}s + K_{sp}}{T_{cc}T_w\tau_{si}s^3 + T_w\tau_{si}s^2 + K_{sp}\tau_{si}s + K_{sp}}. \tag{3.33}$$

Then, the characteristic equation of the proposed system is

$$D(s) = T_{cc}T_w\tau_{si}s^3 + T_w\tau_{si}s^2 + K_{sp}\tau_{si}s + K_{sp} \tag{3.34}$$

and its first column in Routh array is $[T_{cc}T_w\tau_{si}, T_w\tau_{si}, K_{sp}T_{cc}(\delta^2 - 1), K_{sp}]^{\mathrm{T}}$. It can be found all elements in this column is positive, which, according to Routh's stability criterion, proves the stability of the proposed system.

3.4   Simulation evaluation

The simulation model of the proposed high-speed SRM drive system constructed in Matlab/Simulink is shown in Fig. 3.8. The power converter and SRM are constructed based on the library blocks, and the control strategy is realized by Matlab Function. Fig. 3.9 presents the steady-state simulation results at the rated speed. For the grid side, a sinusoidal shape grid-side current, which is in the same phase as the grid-side voltage, is obtained during the operation of SRM. The capacitor balancing control has been successfully implemented, so the curves of v_{c1} and v_{c2} overlaps. Independent regulation for the d-axis and q-axis component of the grid-side current has been realized based on the current feed-forward control. The q-axis component of grid-side current is kept at around 0 A to control the grid-side power quality while regulating the d-axis component i_d to around 7.8 A for motor operation. For the motor side, even if the motor operates at 25000 r/min, the tailing current declines rapidly under the double-voltage demagnetization mode of the 4-level SRM converter.

The dynamic test results when speed changes from 20000 r/min to 25000 r/min to 18000 r/min are shown in Fig. 3.10. The sinusoidal gird-side current and balanced capacitor voltages can be obtained during the whole dynamic process. In the proposed system, the high-speed SRM is controlled by i_d, so once the speed command is changed from 20000 r/min to 25000 r/min, i_d is immediately increased to provide more power for SRM, and the capacitor voltage is boosted from 85 V to 135 V accordingly. When speed command is changed from 25000 r/min to 18000 r/min, the direction of i_d is immediately reversed, and the phase difference between grid-side voltage and grid-side current has been changed from 0 to π (the power factor has been changed from 1 to -1). In this process the energy starts to flow from the DC side to the grid to reduce the motor speed as soon as possible. As a result, the speed is rapidly reduced by directly transferring the excess energy back to the grid.
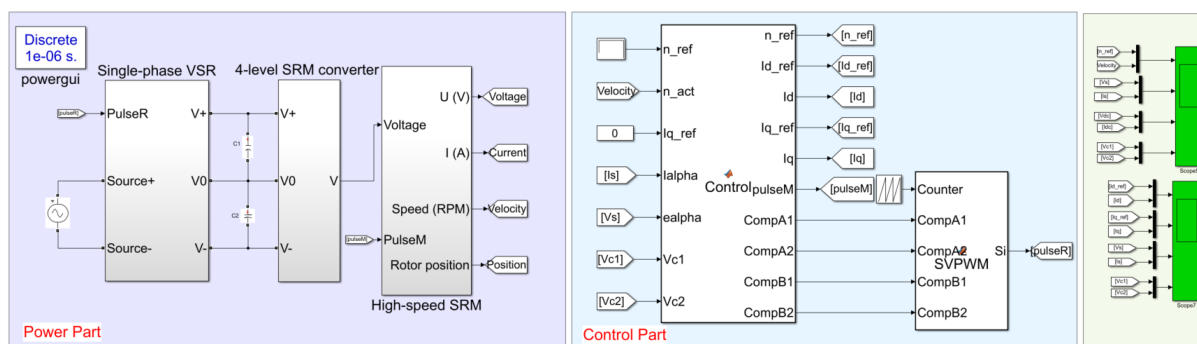
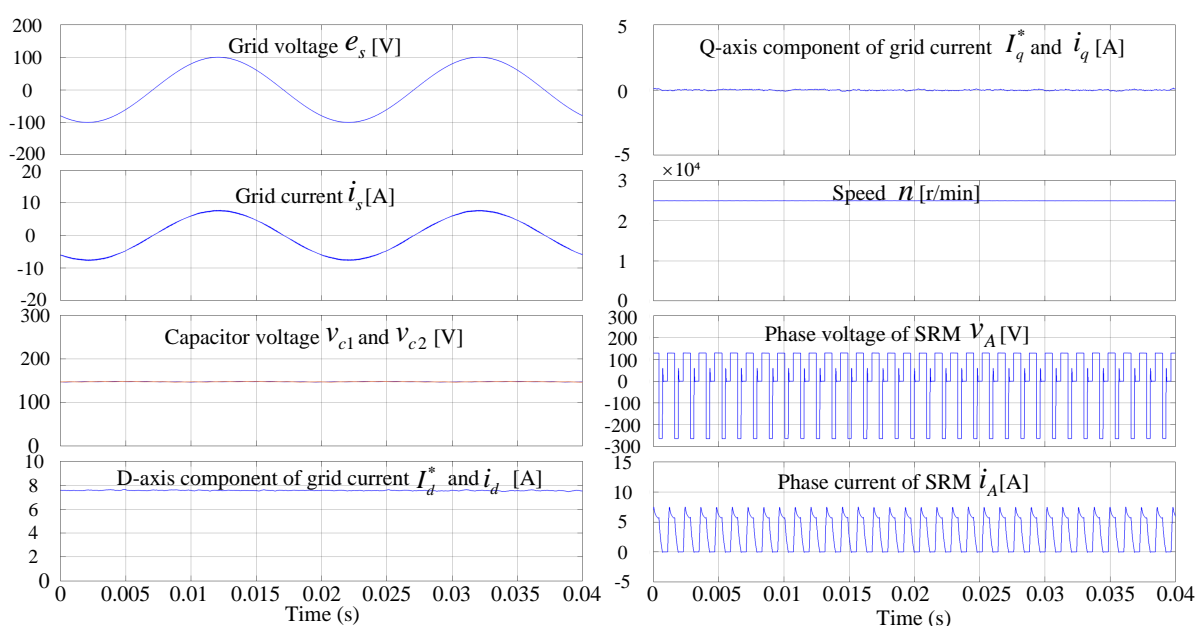Figure 3.8: Simulation model of the proposed high-speed SRM control system.

Figure 3.9: Steady-state simulation results at rated speed of 25000 r/min.

Table 3.3: Experimental parameters of the system with 4-level SRM converter

VSR			PMSM		
Parameter	Description	Value	Parameter	Description	Value
$e_s(\text{V})$	Grid-side voltage (peak)	100	$T_{\text{em}}(\text{N} \cdot \text{m})$	Rated torque	0.12
$R_s(\Omega)$	Filter resistance	0.004	$n_r(\text{r/min})$	Rated speed	25000
$L_s(\text{mH})$	Filter inductance	4	N_s/N_r	Number of stator pole	4
$C_1, C_2(\mu\text{F})$	DC-link capacitor	2720	$l_{\text{air}}(\text{mm})$	Number of rotor pole	2

3.5   Experimental evaluation
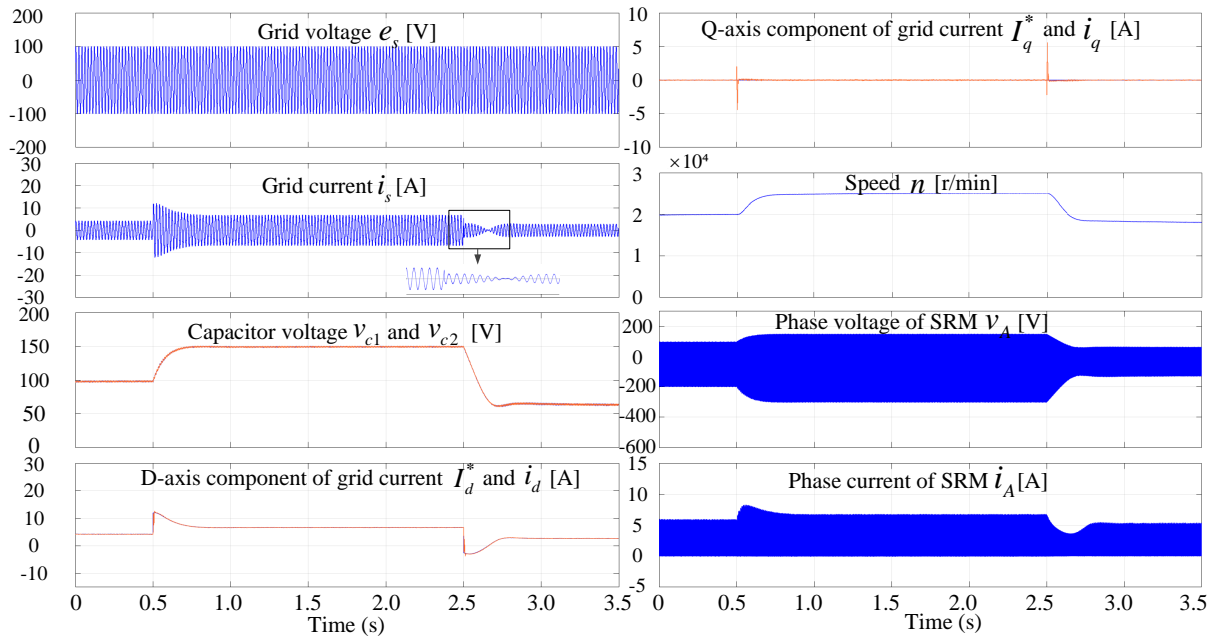
Figure 3.10: Dynamic simulation results when speed changes from 20000 r/min to 25000 r/min to 18000 r/min.

3.5.1 Experimental parameters and flowchart

A testbench is constructed to verify the feasibility of the proposed SRM drive system. A 4/2 high-speed SRM with fan-type load is coupled to proposed drive topology and subjected to extensive tests. The rotor position is measured using a high-speed 1024-line incremental encoder (HEIDENHAIN ERO1420). A digital signal processor (DSP)-based (TMS320F28335) controller manages the control of the whole system. The control period T_c is set to 20 kHz in the algorithm. Fig. 3.11 shows the photograph of the testbench used to verify the proposed idea. The specifications of the proposed drive topology and SRM are shown in Table 3.3. An off-the-shelf T-type single-phase three-level VSR (F3L75R12W1H3_B27) from Infineon is used as the front end. Four switches (IXGH72N60B3) and four diodes (DSEI60-06A) are used to construct the 4-level SRM converter. The flow chart of the proposed control strategy is presented in Fig. 3.12.

3.5.2 Experimental results

3.5.2.1 Steady-state performances

Fig. 3.13 presents the experimental waveforms of the ten operating combinations of the 4-level SRM converter. It can be found that each of the four conduction modes can be applied to the converter successfully. Since the conduction mode of one phase will not be affected by that of the other phase at all, full inter-phase control independence has been realized.

For high-speed SRM, the current drops very slowly due to the high rotational speed after being switched off, so it can easily persist into the inductance decreasing region. To ensure the performance of the high-speed SRM drive system, it is crucial to accelerate the current decreas-
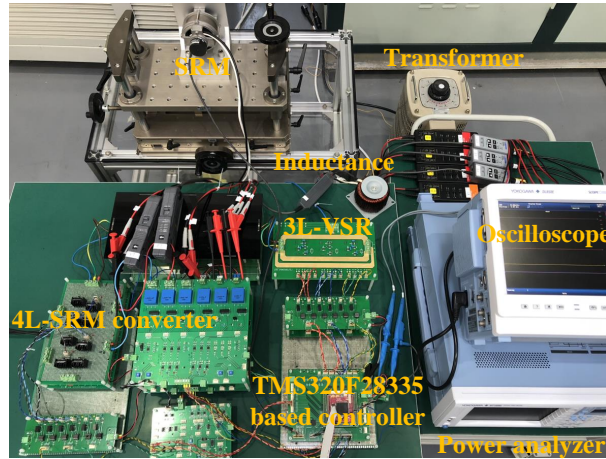
Figure 3.11: Idea-proofed testbench of the system with 4-level SRM converter.
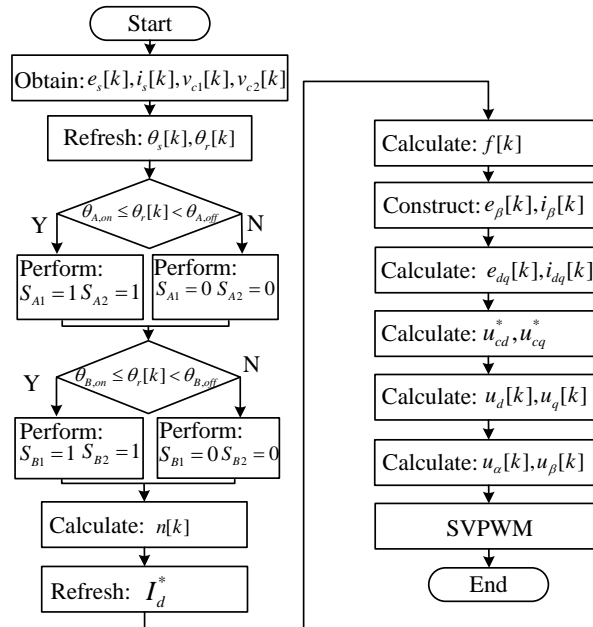

Figure 3.12: Flow chart of an interrupt service routine.

ing process by fast demagnetization mode. The conventional demagnetization mode $(-v_c)$ corresponds to a slow demagnetization process, yet double-voltage demagnetization mode $(-2v_c)$ can realize a fast demagnetization. It can be found from Fig. 3.14 that the double-voltage demagnetization mode can significantly reduce the tailing time of the demagnetization current, compared with the conventional demagnetization mode.

The steady-state experimental results obtained at 20000 r/min and 25000 r/min are shown in Fig. 3.15 and Fig. 3.16, respectively. It can be found that the voltage of C_1 and C_2 coincide with each other all the time, which means the capacitor balancing control has been successfully implemented. Stable DC-link voltage whose value is around 160 V is obtained, and the voltage ripple is observed to be $\pm$ 2 V in the experiment. Independent regulation for the d-axis and q-axis component of the grid-side current has been realized based on the current feedforward
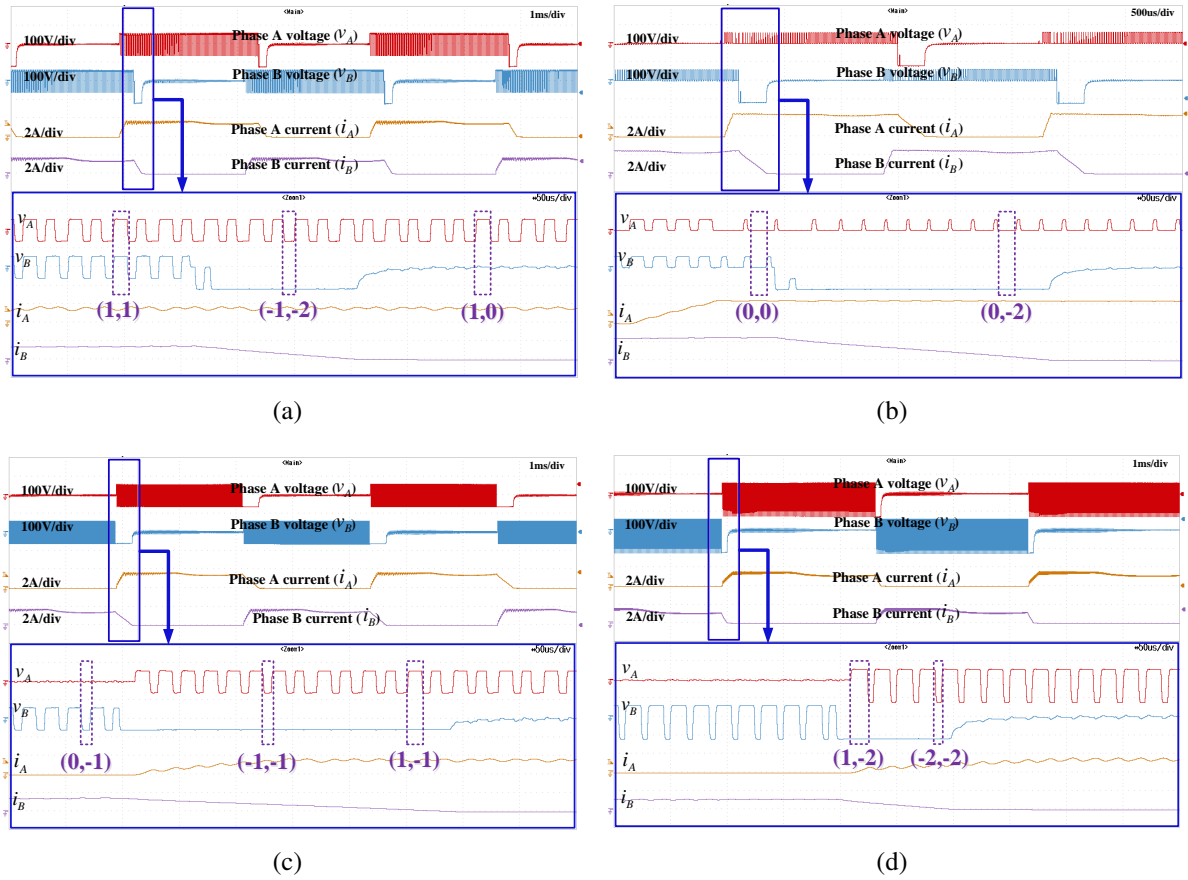
Figure 3.13: Experimental waveforms of the ten operation combinations. (a) (1,1), (-1,-2), and (1,0) are presented. (b) (0,0) and (0,-2) are presented. (c) (0,-1), (-1,-1) and (1,-1) are presented. (d) (1,-2) and (-2,-2) are presented.

control. A dual, 12-bit serial input digital-to-analog converter (DAC) 7612 is used to present the curves of i_d and i_q. Moreover, an offset has been added to DAC output to display both the positive and negative value of i_d and i_q, so the blue and purple short lines locating on the left-most side of the curves indicate 0 A for i_d and i_q, respectively. This setup is also applied to all the curves of i_d and i_q presented in this chapter. The q-axis component of grid-side current has been kept within ± 0.15 A to control the grid-side power quality. The d-axis component is regulated to 4.2 A to provide enough active power for motor operation. A sinusoidal grid-side current which is in the same phase as the grid-side voltage is obtained during the operation of SRM. For the motor side, as has been shown in Area 1 of Zoom 2 window, the current tailing time in the demagnetization process has dramatically decreased because of the adoption of the 4-level SRM converter. Although the motor is running at 20000 r/min, the tailing current declines rapidly under the double-voltage demagnetization mode. Fig. 3.16 displays the waveforms when the motor runs at 25000 r/min. v_{c1} and v_{c2} are still well balanced. The DC-link voltage is increased to 260 V, and the ripple at 25000 r/min is within ± 2.5 V. i_q has been regulated within ± 0.2 A to reduce the reactive power flow in grid, and i_d is around 7.6 A to provide enough energy for the SRM. A standard sinusoidal grid-side current is obtained, even if the
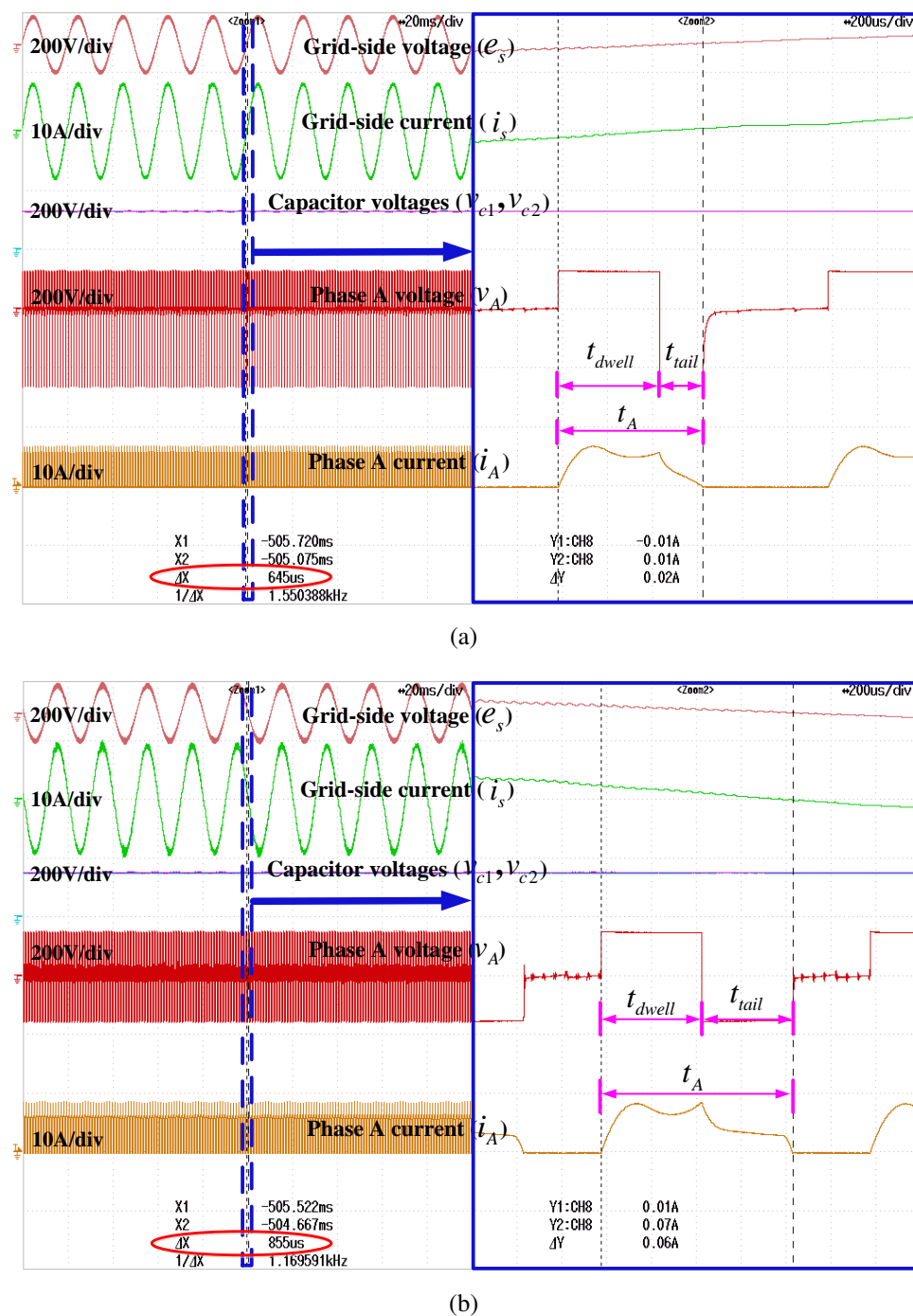
(a)

(b)

Figure 3.14: Experiment results at 25000 r/min. (a) Demagnetized by $-2v_c$. (b) Demagnetized by $-v_c$.

pulsatile current is flowing on DC-link. The harmonic spectrum of grid-side current at 20000 r/min and 25000 r/min are illustrated in Fig. 3.17. With the proposed drive topology, the THDs have dropped down to the value within 5 %.
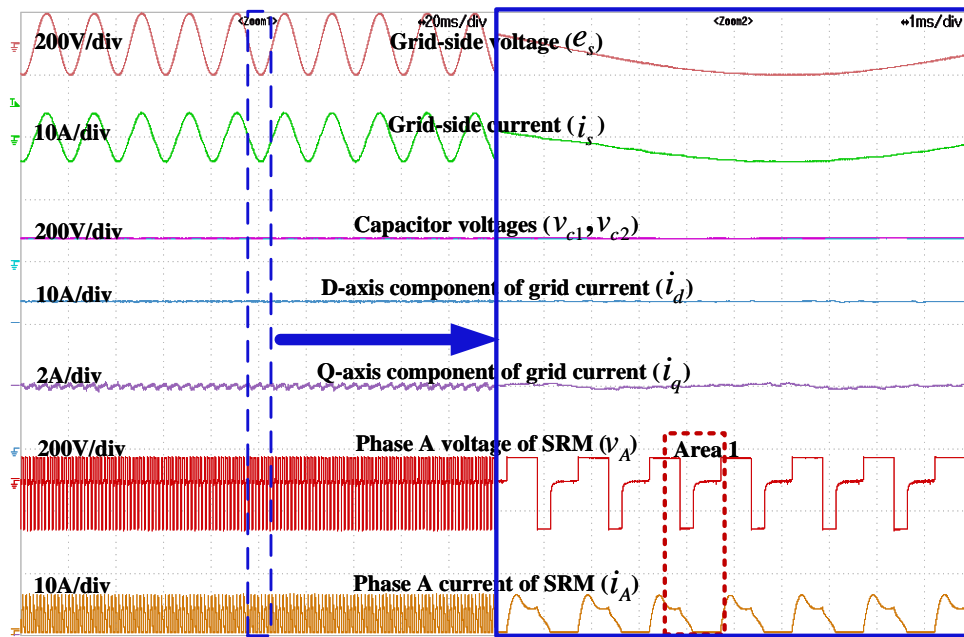
Figure 3.15: Steady-state experimental results at 20000 r/min
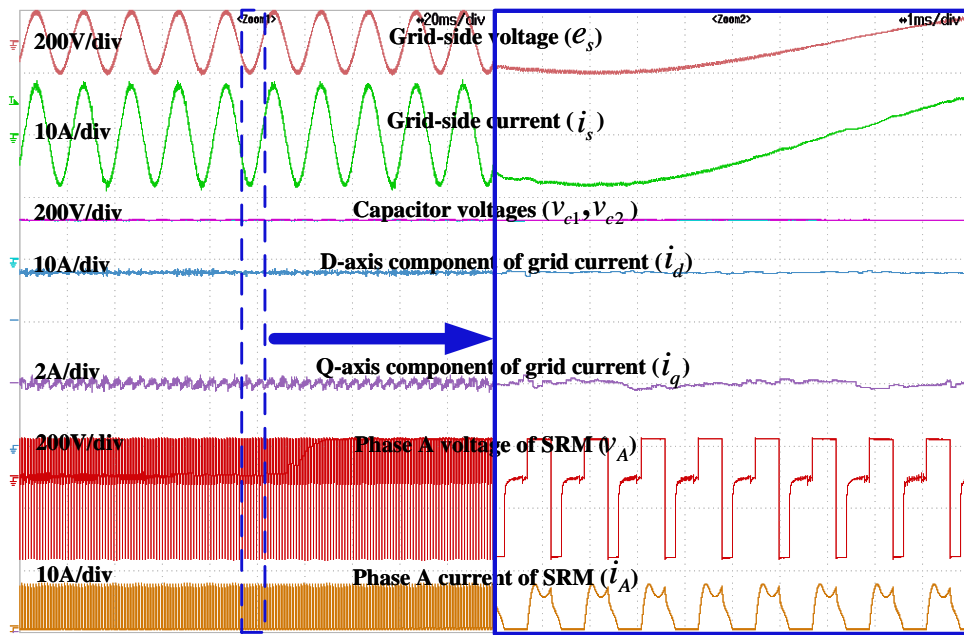

Figure 3.16: Steady-state experimental results at 25000 r/min.

3.5.2.2 Transient-state performances

Fig. 3.18 shows the dynamic test result when the motor starts from standstill to 25000 r/min. As can be seen from the Zoom 1 window that the grid-side current can respond to the increased load torque and rotational speed in time once a new speed command is issued. Although there are some burrs on the curve of i_d, they are just the noises on the output port of DAC because grid-side current does not present any corresponding change that matches those burrs. Double-
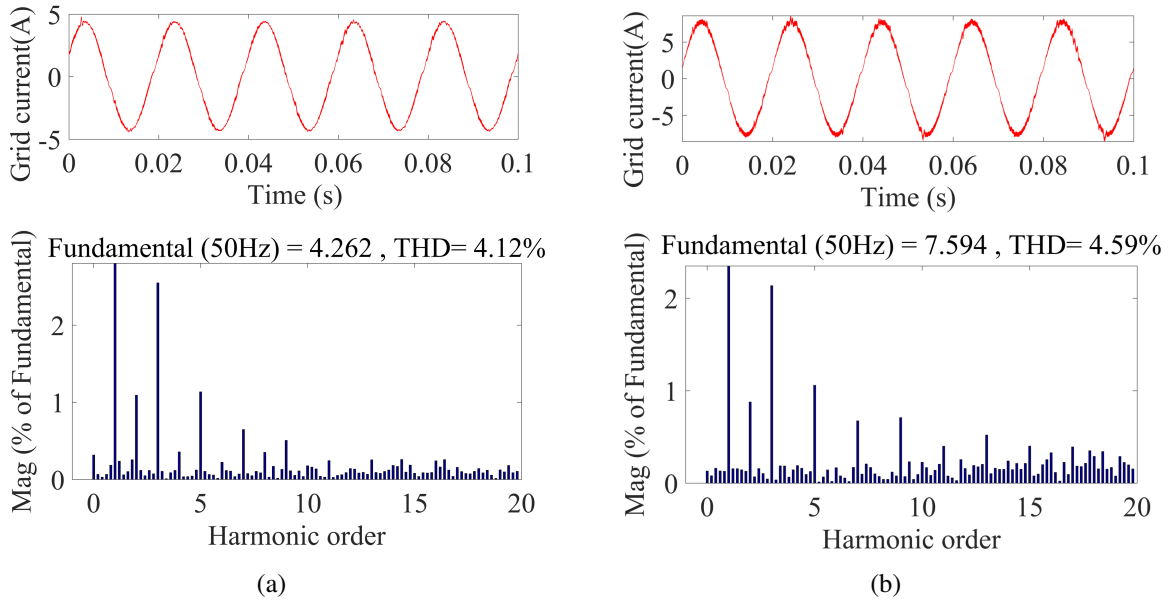
Figure 3.17: Harmonic spectrum of grid-side current at different speeds. (a) At 20000 r/min. (b) At 25000 r/min.

voltage demagnetization is realized once phase switches are turned off. Strict over-current protection has been performed in the starting process. It can be seen in Area 1 that the current is chopped in the conduction region every time the current reaches the predefined maximal threshold (9.5 A). Despite there is a voltage difference between the two capacitors in the first serval periods, the two capacitors can be pulled back to a balanced state by the capacitor balancing control.

The dynamic test result when speed changes from 20000 r/min to 25000 r/min to 20000 r/min is shown in Fig. 3.19. In Zoom 1 window, when the speed command changes from 20000 r/min to 25000 r/min, i_d is increased to 12 A to provide more active power at the motor shaft. The sinusoidal gird-side current that is in phase with grid-side voltage can be obtained during the whole dynamic process. SRM is directly controlled by i_d. Most importantly, once the reduced command speed is issued, the direction of i_d is immediately reversed to reduce the motor speed as soon as possible, which means the energy starts to flow from DC side to grid. During this process, the phase difference between grid-side voltage and grid-side current changes from 0 to π, and accordingly, the power factor changes from 1 to -1. Thanks to the ability of bidirectional energy flow of VSR, the speed is rapidly reduced by transferring the excess energy back to the grid.

The speed error waveform during speed regulation is shown in Fig. 3.20. An offset has been added to the DAC output of speed error, so the short pink line on the left side of the curve indicates 0 r/min. Besides, an upper-lower limit is set to avoid unnecessary overflow when command speed changes abruptly. Based on the proposed drive topology, the speed error can be governed within 15 r/min at steady state.
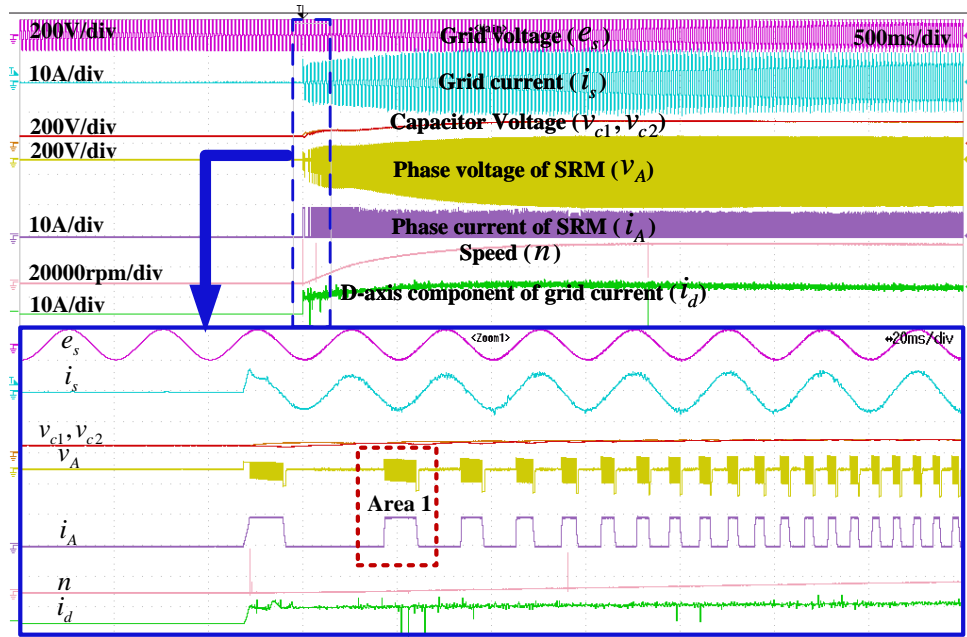
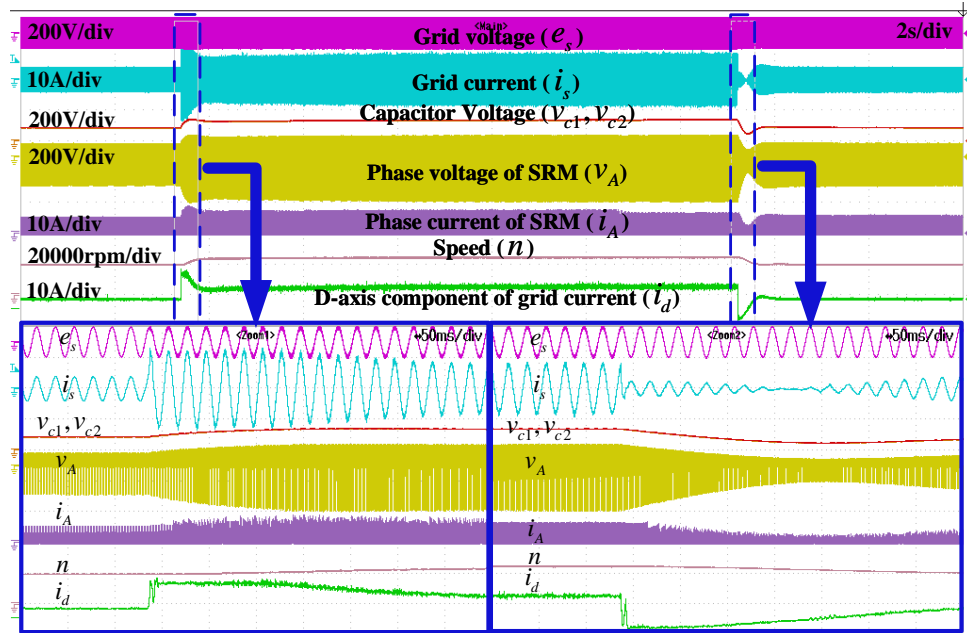Figure 3.18: Dynamic test results when the motor starts from standstill to 25000 r/min.

Figure 3.19: Dynamic test results when speed changes from 20000 r/min to 25000 r/min to 20000 r/min.

3.5.2.3 THDs and power factors

Fig. 3.21 shows the power analyzer screenshots of the proposed drive system composed of VSR and 4-level SRM converter. $U_{rms1}, I_{rms1}, P_1, Q_1, S_1$, and λ_1 denote the voltage, current, active power, reactive power, apparent power, and power factor of grid-side, respectively. η_1 is calculated based on the active power at SRM winding terminal and grid-side, which is the

Figure 3.20: Dynamic test results when speed changes from 0 r/min to 20000 r/min to 25000 r/min to 20000 r/min.

efficiency of the whole drive topology. η_2 is the efficiency of the front end connected before the SRM converter. Compared with the conventional DBR, all the front ends with power factor correction will unavoidably cause drop in efficiency, which is brought by the frequent switching action of power switches, whereas high grid-side power quality can be obtained. The THDs and power factors of the proposed system has been summarized in Fig. 3.23. It can be seen that the power factor in the proposed drive system has been increased to around 0.99, and grid-side current THDs have been reduced to below 5%. Fig. 3.22 presents the power analyzer screenshots when tests are carried out on the topology composed of the VSR and the split-DC converter. In the experiments, the mechanical output power has been controlled to be the same at the same speed. The split-DC converter adopts conventional demagnetization mode $(-v_c)$, which corresponds to a relatively long current tailing time. It can be found from Fig. 3.21 and Fig. 3.22 that the topology based on split-DC converter consumes more grid-side active power than the topology based on 4-level SRM converter when providing the same output power, which indicates the lower efficiency of the split-DC converter. However, no matter which SRM converter is adopted, the front-end VSR always has a satisfying regulation effect on grid-side power quality since the power factor has been controlled around 0.99.

3.6 Summary

A novel drive topology has been proposed for a high-speed SRM drive system, and a series tests are carried out on a testbench to show the validity of the proposed control strategy. The contributions of this chapter are as follows:

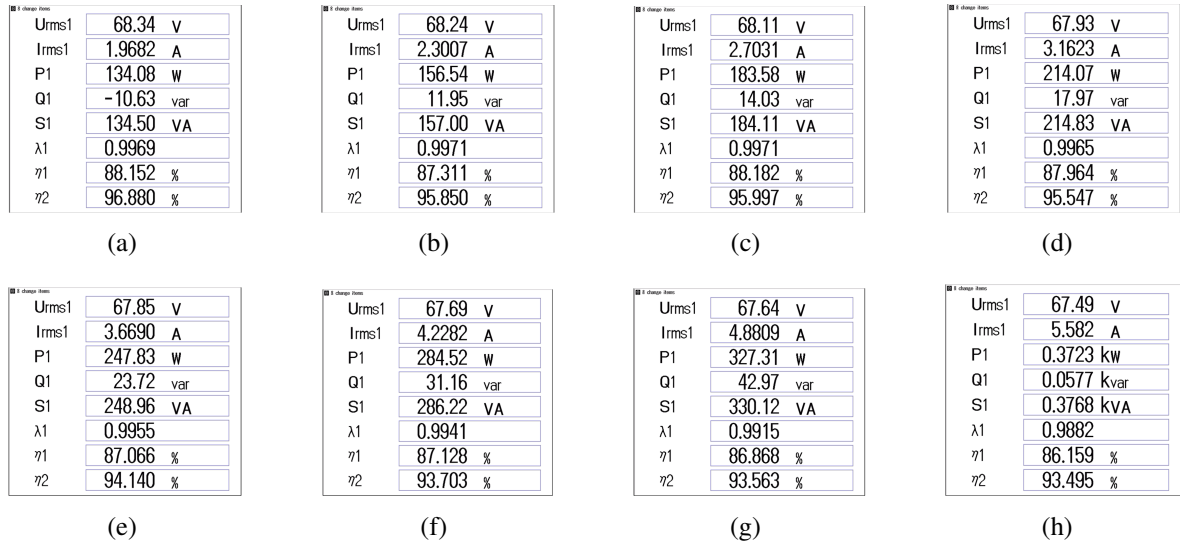1) Realize the fast demagnetization. A new four-voltage-rail SRM converter without the

	(a)	(b)	(c)	(d)
Urms1	68.34 V	68.24 V	68.11 V	67.93 V
Irms1	1.9682 A	2.3007 A	2.7031 A	3.1623 A
P1	134.08 W	156.54 W	183.58 W	214.07 W
Q1	−10.63 var	11.95 var	14.03 var	17.97 var
S1	134.50 VA	157.00 VA	184.11 VA	214.83 VA
$\lambda 1$	0.9969	0.9971	0.9971	0.9965
$\eta 1$	88.152 %	87.311 %	88.182 %	87.964 %
$\eta 2$	96.880 %	95.850 %	95.997 %	95.547 %

	(e)	(f)	(g)	(h)
Urms1	67.85 V	67.69 V	67.64 V	67.49 V
Irms1	3.6690 A	4.2282 A	4.8809 A	5.582 A
P1	247.83 W	284.52 W	327.31 W	0.3723 kw
Q1	23.72 var	31.16 var	42.97 var	0.0577 kvar
S1	248.96 VA	286.22 VA	330.12 VA	0.3768 kVA
$\lambda 1$	0.9955	0.9941	0.9915	0.9882
$\eta 1$	87.066 %	87.128 %	86.868 %	86.159 %
$\eta 2$	94.140 %	93.703 %	93.563 %	93.495 %

Figure 3.21: Screenshots from power analyzer when $-2v_c$ is used for demagnetization. (a) 18000 r/min. (b) 19000 r/min. (c) 20000 r/min. (d) 21000 r/min. (e) 22000 r/min. (f) 23000 r/min. (g) 24000 r/min. (h) 25000 r/min.

	(a)	(b)	(c)	(d)
Urms1	68.55 V	68.42 V	68.27 V	68.17 V
Irms1	2.0256 A	2.3622 A	2.7410 A	3.2368 A
P1	138.33 W	161.07 W	186.42 W	219.67 W
Q1	12.11 var	13.39 var	16.14 var	20.73 var
S1	138.86 VA	161.63 VA	187.12 VA	220.64 VA
$\lambda 1$	0.9962	0.9966	0.9963	0.9956
$\eta 1$	86.582 %	86.330 %	86.273 %	86.050 %
$\eta 2$	96.414 %	95.959 %	95.242 %	94.803 %

	(e)	(f)	(g)	(h)
Urms1	68.06 V	67.99 V	67.90 V	67.83 V
Irms1	3.7695 A	4.3365 A	5.0162 A	5.851 A
P1	255.11 W	292.73 W	340.36 W	0.3911 kw
Q1	27.18 var	35.03 var	45.86 var	0.0674 kvar
S1	256.55 VA	294.82 VA	343.44 VA	0.3969 kVA
$\lambda 1$	0.9944	0.9929	0.9910	0.9855
$\eta 1$	85.768 %	86.156 %	84.701 %	84.570 %
$\eta 2$	93.764 %	94.324 %	93.012 %	92.294 %

Figure 3.22: Fig. 12. Screenshots from the power analyzer when $-v_c$ is used for demagnetization. (a) 18000 r/min. (b) 19000 r/min. (c) 20000 r/min. (d) 21000 r/min. (e) 22000 r/min. (f) 23000 r/min. (g) 24000 r/min. (h) 25000 r/min.

common switch is proposed, within which the full control independence of every phase can be realized. Its double-voltage demagnetization mode can significantly reduce the current tailing time, which improves the drive performance of the high-speed SRM.

2) Regulates the front-end converter and SRM together. The control of front-end VSR and SRM are integrated into one current control strategy based on virtual orthogonal system, within which the d-axis and q-axis component of grid-side current control the SRM speed and grid-side
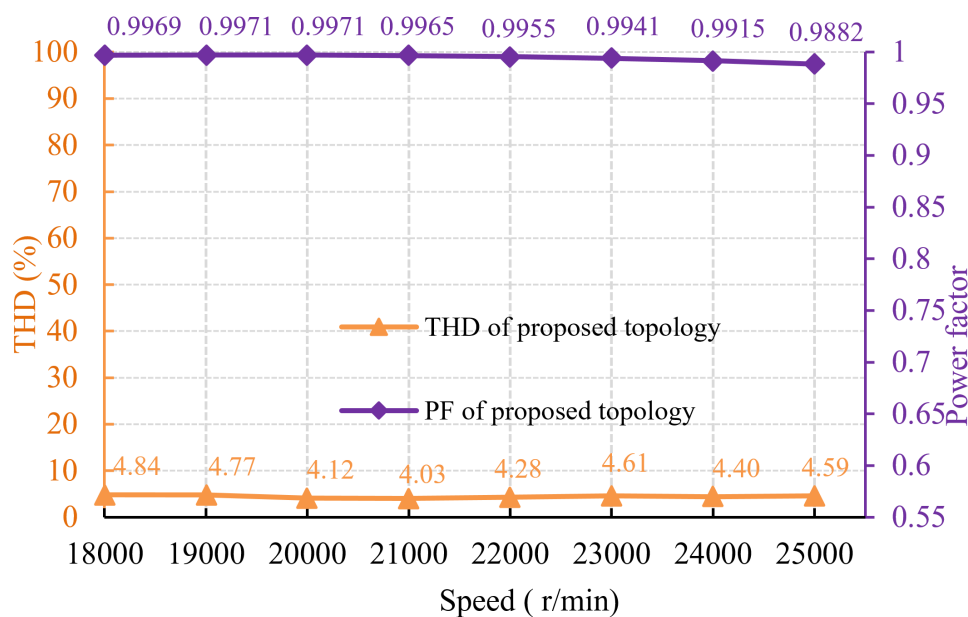
Figure 3.23: THDs and power factors at different speeds.

power factor, respectively.

- Control the SRM speed. Stable speed is realized, and the speed error can be governed within $\pm$ 15 r/min at 25000 r/min in the experiment.

- Control the grid-side power quality. The grid-side power factors in the topology based on conventional diode rectifier are just around 0.7, yet they have been increased to around 0.99 through the control of i_q. The grid-side current THDs in the topology based on the diode rectifier are up to 92 %, yet the THDs of the proposed drive topology have been reduced to below 5 %.

3) Realize the bidirectional energy flow. In the proposed system, the energy not only can flow from grid to motor but can be fed back to gird under the regulation of grid-side current.

CHAPTER 4

P-DBPC strategy for grid-connected high-speed SRM system

4.1 Introduction

The control simplicity of SRMs has made them attractive research objects in these decades [68, 69]. Additionally, the singly-excited doubly salient structure without permanent magnet, excellent fault-tolerance ability, and fast acceleration capability enable SRMs' reliable operation at high speeds and high temperatures. Conventionally, the DC source required by the SRM power converter is supplied through the DBR, but a large amount of reactive power and current harmonics are induced into the grid, which is incredibly harmful to the system [70]. To get a satisfactory gird-side power quality, several DBR-connected DC-DC topologies are developed for SRM drive to improve the power factor. In [71], a front-end converter is employed to regulate the DC-link voltage in motor driving mode, and in idle mode, the front-end converter is arranged as a buck converter to charge the battery from AC input. Four diodes of the motor converter are utilized to form the buck converter, and the inductors of two motor windings are used as the input filter components during each half AC cycle. However, the additional circuit increases the costs and reduces the power density. In [72], a compact battery-powered SRM drive for electric vehicle with voltage-boosting and on-board power-factor-corrected-charging capabilities is presented. The three-phase windings of the SRM is reused and one additional diode and one relay need to be employed, which not only increases the semiconductor device but also may generate torque. In [73], intelligent power modules (IPMs) are adopted to realize an integrated driving/charging drive for SRMs. Five legs of two IPMs are employed to construct the modified four-phase ASHB converter, and a front-end DC-DC boost converter is formed by the remaining one leg to boost the DC-link voltage from a battery. During charging mode, some IPM power devices and motor windings are arranged to form a buck-boost or buck converter to convert the AC input to charge the battery with good power quality. In [74], a highly compact topology that realizes high power factor for the charging mode is proposed

for electric vehicle applications. The new drive topology reuses the stator winding and power devices of SRM converter. The diodes in two phases of ASHB converter are used to form the DBR to convert the AC voltage into DC voltage firstly. The winding and three power devices of the third phase are used to form a single-phase DC-DC boost converter to improve the power factor of AC input. Motor driving mode and charging mode with unity power factor can be switched by adding just one relay to the main drive circuit. Due to the application field, the aforementioned topologies do not need to realize power factor correction during the operation of SRM, but its concept based on AC-DC and DC-DC boost converters is generally adopted in grid-connected SRM drive system for power factor correction. In [75], the front end supplying two equal output voltages for the back-end split-DC converter is adopted for power quality improvement. However, since each capacitor on the DC link manages the energizing for one phase of SRM, the symmetry of capacitor voltages must be emphasized. Moreover, the computation burden caused by the enumeration algorithm is heavy for the controller. In [20], by adding the high-frequency capacitor and adequately designing the bulky capacitor in the switch-mode rectifier, the voltage spikes on the DC link are damped to facilitate the improvement of the line drawn power quality. Nevertheless, the inter-phase control independence is weakened due to the coupling between excitation mode and demagnetizing mode in the back-end SRM converter. In [25], the developed SRM drive system performs harmonic cancellation by treating the line current and ripples as disturbances, yet several control strategies are simultaneously employed. In [76], a circuit modified on the single-ended primary inductor converter is researched, but the speed is not directly governed in the control strategy. The DBR-connected topologies also can be replaced with AC-DC topologies to enhance the power quality. In [29], the three-level converter is developed to drive the SRMs, but many power devices are employed in the system, which is low cost-effective. The drive circuit in [77], which is made up of two Cuk circuits, is developed to generate dual equal output voltages for SRM split-DC converter, and the circuit actually acts as an individual Cuk converter during individual half cycles of the input voltage. However, an additional controller is requisite to keep the upper and lower capacitor on DC link balanced.

Enhanced grid-side power factor can be achieved in the above SRM drive systems, but the energy cannot be transferred back to the grid. In [78], a SRM drive topology with bidirectional energy flow and fast demagnetization voltage is proposed, and a current-regulated strategy is developed in a virtual orthogonal system in which a fictitious phase is specially constructed to ease the modeling and control in dq coordinate plane. The phase-locked loop and rotatory transformation are requisite in the system, both of which complicate the system control. Moreover, the balancing control for the DC-link capacitors should always be considered by an additional control loop which inevitably increases the system control complexity. In this chapter, the modeling and control for the SRM drive system are completed in the stationary coordinate plane in the proposed P-DBPC strategy, so the phase locking and rotatory transformation for variables are unnecessary. More importantly, since the SRM drive can be regarded as a load of the VSR, a direct connection of power between the front-end VSR and back-end SRM is built, and the SRM is controlled by manipulating the instantaneous active power flowing to the motor side. An online observer is employed to make sure the instantaneous active power and instantaneous reactive power can tightly track their respective references. The errors between the predicted and actual power are considered as disturbances. The feed-forward action of the errors ensures that the estimated disturbance term is added to the calculated voltage reference, thereby provid-

ing a robust control. Hence, the errors caused by the mismatches between nominal values and the practical value of the parameters can both be compensated by adding a term to the expression of the desired voltage vector. Additionally, without causing computational burden on the controller, an A-SVPWM approach is developed to improve system efficiency by reducing the switching action of power switches.
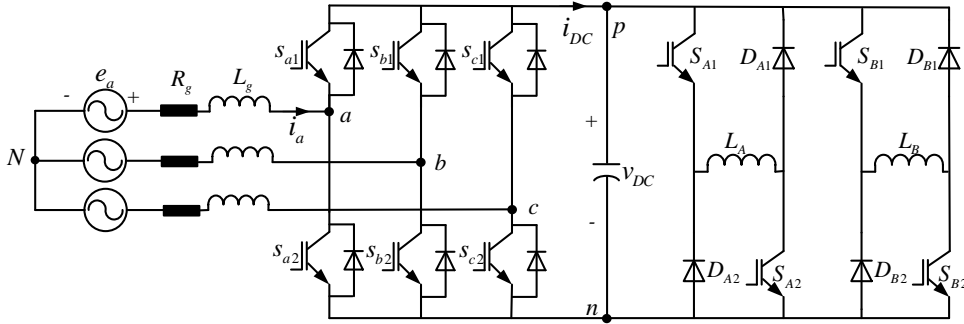
4.2 Drive topology and mathematical model

Figure 4.1: The drive topology of high-speed SRM drive based on P-DBPC.

As can be seen from Fig. 4.1, each leg of the VSR has two switches, and they must be controlled in complementary pairs. The terminal voltage of VSR, i.e., u_{xn}, $x \in \{a, b, c\}$ can be set either to v_{DC} or 0 by configuring the switching state s_x of each leg

$$u_{xn} = \begin{cases} v_{DC} & s_x = 1(s_{x1} \; On, s_{x2} \; Off) \\ 0 & s_x = 0(s_{x1} \; Off, s_{x2} \; On) \end{cases} x \in \{a, b, c\}. \tag{4.1}$$

Totally, there are eight switching states in this VSR

$$\vec{s}_v \in \left\{ [0, 0, 0]^{\mathrm{T}}, [0, 0, 1]^{\mathrm{T}}, \cdots, [1, 1, 0]^{\mathrm{T}}, [1, 1, 1]^{\mathrm{T}} \right\} \tag{4.2}$$

where $\vec{s}_v = [s_a, s_b, s_c]^{\mathrm{T}}$, $v \in \{0, 1, \cdots, 7\}$. To ease the modeling and controller design, variables $\vec{\xi}_{abc} = [\xi_a, \xi_b, \xi_c]^{\mathrm{T}}$ in abc coordinate plane are transformed to $\vec{\xi}_{\alpha\beta} = [\xi_\alpha, \xi_\beta]^{\mathrm{T}}$ in stationary $\alpha\beta$ coordinate plane by $\vec{\xi}_{\alpha\beta} = M_{abc-\alpha\beta}\vec{\xi}_{abc}$, with $M_{abc-\alpha\beta}$ being the Clark-transformation matrix

$$\vec{\xi}_{\alpha\beta} = \underbrace{\frac{2}{3} \begin{bmatrix} 1 & -0.5 & -0.5 \\ 0 & \frac{\sqrt{3}}{2} & -\frac{\sqrt{3}}{2} \end{bmatrix}}_{M_{abc-\alpha\beta}} \vec{\xi}_{abc}. \tag{4.3}$$

Thus, the model of the VSR in stationary $\alpha\beta$ coordinate system is given by

$$\vec{e}_{\alpha\beta}(t) = R_g\vec{i}_{\alpha\beta}(t) + L_g\frac{d\vec{i}_{\alpha\beta}}{dt} + \vec{u}_{\alpha\beta}(t) \tag{4.4}$$

where e, i, u, L_g, and R_g are grid-side voltage, current, converter voltage, filter inductor, and filter resistor, respectively. Each of the eight switching states $\vec{s}_v$ has a corresponding converter voltage vector [79]

$$\vec{u}_{\alpha\beta}(t) = \boldsymbol{M}_{abc-\alpha\beta}(\vec{u}_{abcn}(t) + u_{nN}(t)) = \boldsymbol{M}_{abc-\alpha\beta}\vec{s}_v(t)v_{DC} \tag{4.5}$$

where $\vec{u}_{abcn} = [u_{an}, u_{bn}, u_{cn}]^{\mathrm{T}}$ and u_{nN} is expressed as

$$u_{nN}(t) = -\frac{1}{3}v_{DC}\sum_{x=a,b,c} s_x. \tag{4.6}$$

For the convenience of description, eight base vectors denoted as $\vec{u}_v$, $v \in \{0, 1, \cdots, 7\}$ are defined to represent the converter voltage vectors corresponding to $\vec{s}_v$ in $\alpha\beta$ coordinate plane.

4.3   Instantaneous power theory

For power systems with sinusoidal voltages and currents, quantities such as active power, reactive power, etc., are based on the average concept [80]. Many contributors have attempted to redefine these quantities to deal with three-phase systems with distorted currents and voltages. Among them, Akagi et al. [81] have introduced an interesting concept of instantaneous power theory. This concept gives an effective method to control the instantaneous real and reactive power for three-phase systems, and the detailed definitions are presented as follows.

Consider the network whose terminal voltages and currents are $\vec{e}_{abc} = [e_a, e_b, e_c]^{\mathrm{T}}$ and $\vec{i}_{abc} = [i_a, i_b, i_c]^{\mathrm{T}}$, respectively. The instantaneous real power in the time domain is expressed as [82]

$$p(t) = e_a(t)i_a(t) + e_b(t)i_b(t) + e_c(t)i_c(t) \tag{4.7}$$

where $i_a + i_b + i_c = 0$. $\vec{e}_{abc}$ and $\vec{i}_{abc}$ in (4.7) can be expressed in terms of their corresponding space phasors $\boldsymbol{e}(t)$ and $\boldsymbol{i}(t)$

$$\begin{aligned}
p(t) = {} & \Re\left\{\boldsymbol{e}(t)e^{j0}\right\}\Re\left\{\boldsymbol{i}(t)e^{j0}\right\} + \Re\left\{\boldsymbol{e}(t)e^{-j\frac{2}{3}\pi}\right\}\Re\left\{\boldsymbol{i}(t)e^{-j\frac{2}{3}\pi}\right\} \\
& + \Re\left\{\boldsymbol{e}(t)e^{-j\frac{4}{3}\pi}\right\}\Re\left\{\boldsymbol{i}(t)e^{-j\frac{4}{3}\pi}\right\}
\end{aligned} \tag{4.8}$$

where $\boldsymbol{e}(t) = \frac{2}{3}\left[e^{j0}e_a(t) + e^{j\frac{2}{3}\pi}e_b(t) + e^{j\frac{4}{3}\pi}e_c(t)\right]$ and $\boldsymbol{i}(t) = \frac{2}{3}\left[e^{j0}i_a(t) + e^{j\frac{2}{3}\pi}i_b(t) + e^{j\frac{4}{3}\pi}i_c(t)\right]$ are space phasors, and $\Re\{\ \}$ is the real-part operator. Based on the identity $\Re\{\boldsymbol{\xi}_1\}\Re\{\boldsymbol{\xi}_2\} = (\Re\{\boldsymbol{\xi}_1\boldsymbol{\xi}_2\} + \Re\{\boldsymbol{\xi}_1\boldsymbol{\xi}_2^\star\})/2$, (4.8) is expressed as

$$\begin{aligned}
p(t) = {} & \frac{\Re\left\{\boldsymbol{e}(t)\boldsymbol{i}(t)e^{j0}\right\} + \Re\left\{\boldsymbol{e}(t)\boldsymbol{i}^\star(t)\right\}}{2} + \frac{\Re\left\{\boldsymbol{e}(t)\boldsymbol{i}(t)e^{-j\frac{4}{3}\pi}\right\} + \Re\left\{\boldsymbol{e}(t)\boldsymbol{i}^\star(t)\right\}}{2} \\
& + \frac{\Re\left\{\boldsymbol{e}(t)\boldsymbol{i}(t)e^{-j\frac{8}{3}\pi}\right\} + \Re\left\{\boldsymbol{e}(t)\boldsymbol{i}^\star(t)\right\}}{2}.
\end{aligned} \tag{4.9}$$

where * indicates the conjugate complex. Since $e^{j0} + e^{-j\frac{4}{3}\pi} + e^{-j\frac{8}{3}\pi} \equiv 0$, (4.9) is simplified to

$$p(t) = \frac{3}{2}\Re\left\{\boldsymbol{e}(t)\boldsymbol{i}^\star(t)\right\}. \tag{4.10}$$

To achieve the analogy with conventional phasor analysis, the definitions of the instantaneous reactive power and the instantaneous complex power are given by [82]

$$q(t) = \frac{3}{2}\Im\left\{\boldsymbol{e}(t)\boldsymbol{i}^\star(t)\right\} \tag{4.11}$$

$$s(t) = p(t) + jq(t) = \frac{3}{2}\boldsymbol{e}(t)\boldsymbol{i}^\star(t) \tag{4.12}$$

where $\Im\{\ \}$ is the imaginary-part operator. $\boldsymbol{e}(t)$ and $\boldsymbol{i}^\star(t)$ in the above expressions also can be expressed in two-phase $\alpha\beta$ reference frame as below

$$\vec{\boldsymbol{e}}_{\alpha\beta}(t) = e_\alpha + je_\beta \tag{4.13}$$

$$\vec{\boldsymbol{i}}^*_{\alpha\beta}(t) = i_\alpha - ji_\beta. \tag{4.14}$$

To obtain equivalent expressions in terms of $\alpha\beta$-frame variables, the following expressions can be got by substituting (4.13) and (4.14) into (4.10) and (4.11)

$$p(t) = \frac{3}{2}\left[e_\alpha(t)i_\alpha(t) + e_\beta(t)i_\beta(t)\right] = \frac{3}{2}\Re\left(\vec{\boldsymbol{e}}_{\alpha\beta}(t)\vec{\boldsymbol{i}}^\star_{\alpha\beta}(t)\right) \tag{4.15}$$

$$q(t) = \frac{3}{2}\left[-e_\alpha(t)i_\beta(t) + e_\beta(t)i_\alpha(t)\right] = \frac{3}{2}\Im\left(\vec{\boldsymbol{e}}_{\alpha\beta}(t)\vec{\boldsymbol{i}}^\star_{\alpha\beta}(t)\right). \tag{4.16}$$

4.4 Proposed P-DBPC strategy

In this section, a deadbeat power control strategy is proposed to govern the front-end converter and back-end SRM shown in Fig. 4.1 simultaneously. Stable SRM control is achieved by controlling the instantaneous active power in the drive system. Enhanced grid-side power quality is achieved through directly reducing the instantaneous reactive power. P-DBPC with disturbance observer can make sure the active and reactive power can track their references without steady-state error even the inaccurate parameter is adopted in the calculation. Besides, without causing burden on the controller, A-SVPWM is developed to increase the system efficiency by lowering the frequency of switching action in the C-SVPWM.

4.4.1 Overall system description

As can be seen from Fig. 4.2, the position θ_r and angular velocity ω_r of the SRM are computed in position estimator through the feedback encoder signals from the motor shaft. Then the two phases of the high-speed SRM are energized in turn according to θ_r under SPC. The turn-on and turn-off angles of phase winding are determined by the experiments of proposed drive system in advance to form a predefined lookup table, and different turn-on and turn-off angles are used at different speeds. The output of speed PI controller of the back-end SRM is torque reference T^*, and the active power reference P^* is obtained by multiplying T^* by the angular velocity
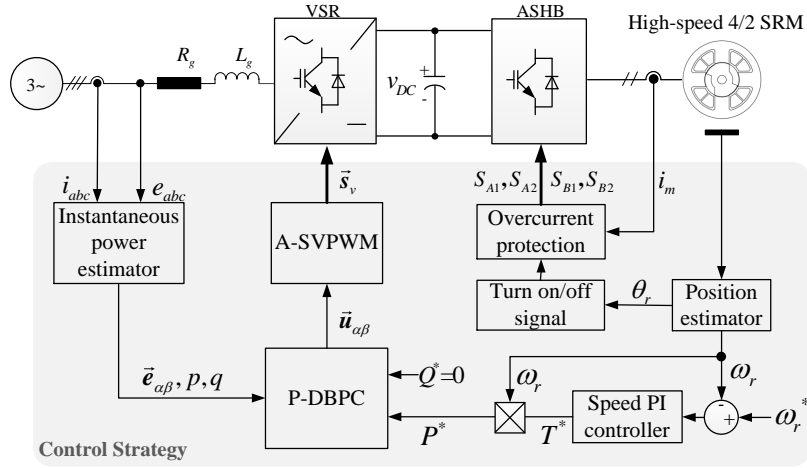
Figure 4.2: The proposed control system of the high-speed SRM drive based on P-DBPC.

ω_r. P^* is the desired instantaneous active power required by the motor side, and it is directly provided by the front-end VSR through the instantaneous active power control of P-DBPC. In this way, a direct connection of power between the front-end VSR and back-end SRM is built, and the whole system can be controlled by manipulating the instantaneous power flow. The overall system control block diagram and the design of the speed controller are presented in the latter part.

4.4.2   Control strategy description

In the proposed system, P-DBPC with disturbance observer is employed to make the input active and reactive power follow P^* and Q^* ($Q^* = 0$ for unity power factor), respectively. It takes advantage of the power model in the stationary $\alpha\beta$ coordinate plane to calculate the desired converter voltage vector, with no demand for dq rotation transformation. In light of the instantaneous power theory, the instantaneous active power $p(t)$ and instantaneous reactive power $q(t)$ can be described by

$$\begin{pmatrix} p(t) \\ q(t) \end{pmatrix} = \frac{3}{2} \begin{bmatrix} e_\alpha(t) & e_\beta(t) \\ e_\beta(t) & -e_\alpha(t) \end{bmatrix} \vec{\boldsymbol{i}}_{\alpha\beta}(t). \tag{4.17}$$

The relationship between e_α and e_β can be described by

$$\frac{d}{dt} \begin{pmatrix} e_\alpha(t) \\ e_\beta(t) \end{pmatrix} = \begin{pmatrix} -\omega_g e_\beta(t) \\ \omega_g e_\alpha(t) \end{pmatrix} \tag{4.18}$$

where $\omega_g = 2\pi f$ denotes the angular frequency of the grid-side voltage. Equation (4.4) can be rewritten as:

$$\frac{d}{dt} \vec{\boldsymbol{i}}_{\alpha\beta}(t) = \frac{1}{L_g} (\vec{\boldsymbol{e}}_{\alpha\beta}(t) - R_g \vec{\boldsymbol{i}}_{\alpha\beta}(t) - \vec{\boldsymbol{u}}_{\alpha\beta}(t)) \tag{4.19}$$

Substituting (4.18) and (4.19) into (4.17) gives

$$\frac{d}{dt}\begin{pmatrix} p(t) \\ q(t) \end{pmatrix} = \frac{3}{2L_g}\begin{bmatrix} e_\alpha(t) & e_\beta(t) \\ e_\beta(t) & -e_\alpha(t) \end{bmatrix}\begin{pmatrix} e_\alpha(t) - u_\alpha(t) \\ e_\beta(t) - u_\beta(t) \end{pmatrix}$$
$$+ \begin{pmatrix} -\frac{R_g}{L_g}p(t) - \omega_g q(t) \\ -\frac{R_g}{L_g}q(t) + \omega_g p(t) \end{pmatrix}. \tag{4.20}$$

(4.20) can be transformed into the following form after being applied with the backward Euler discretization.

$$\begin{pmatrix} p[k+1] \\ q[k+1] \end{pmatrix} = \frac{3T_s}{2L_g}\begin{bmatrix} e_\alpha[k] & e_\beta[k] \\ e_\beta[k] & -e_\alpha[k] \end{bmatrix}\begin{pmatrix} e_\alpha[k] - u_\alpha[k] \\ e_\beta[k] - u_\beta[k] \end{pmatrix}$$
$$+ \begin{pmatrix} p[k] - \frac{T_s R_g}{L_g}p[k] - T_s\omega_g q[k] \\ q[k] - \frac{T_s R_g}{L_g}q[k] + T_s\omega_g p[k] \end{pmatrix} \tag{4.21}$$

where $\xi[k]$, $\xi[k+1]$, and T_s denote variable value at instant k and $k+1$, and control period, respectively. (4.21) holds when the actual values of the inductor and resistor, i.e., L_g and R_g, are brought into the expression. However, it is actually the nominal values, i.e., $L_{g,no}$ and $R_{g,no}$, are involved in the calculation of the prediction since L_g and R_g are unknown. Considering those uncertainties as a dynamic disturbance, (4.21) can be rewritten as

$$\begin{pmatrix} p[k+1] \\ q[k+1] \end{pmatrix} = \frac{3T_s}{2L_{g,no}}\begin{bmatrix} e_\alpha[k] & e_\beta[k] \\ e_\beta[k] & -e_\alpha[k] \end{bmatrix}\begin{pmatrix} e_\alpha[k] - u_\alpha[k] \\ e_\beta[k] - u_\beta[k] \end{pmatrix}$$
$$+ \begin{bmatrix} 1 - \frac{T_s R_{g,no}}{L_{g,no}} & -T_s\omega_g \\ \omega_g T_s & 1 - \frac{T_s R_{g,no}}{L_{g,no}} \end{bmatrix}\begin{pmatrix} p[k] \\ q[k] \end{pmatrix} - \frac{T_s}{L_{g,no}}\begin{pmatrix} g_p[k] \\ g_q[k] \end{pmatrix} \tag{4.22}$$

where the subscript "no" represents the nominal value, and g_p and g_q are the disturbances. Assuming that the values of g_p and g_q are constant during each sampling interval [83], [84], so Luenberger disturbance observer can be constructed as below

$$\begin{pmatrix} \hat{p}[k+1] \\ \hat{q}[k+1] \\ \hat{g}_p[k+1] \\ \hat{g}_q[k+1] \end{pmatrix} = \frac{3T_s}{2L_{g,no}}\begin{bmatrix} e_\alpha[k] & e_\beta[k] \\ e_\beta[k] & -e_\alpha[k] \\ 0 & 0 \\ 0 & 0 \end{bmatrix}\begin{pmatrix} e_\alpha[k] - u_\alpha[k] \\ e_\beta[k] - u_\beta[k] \end{pmatrix}$$
$$+ E\begin{pmatrix} \hat{p}[k] \\ \hat{q}[k] \\ \hat{g}_p[k] \\ \hat{g}_q[k] \end{pmatrix} + \begin{bmatrix} l_1 & 0 & 0 & 0 \\ 0 & l_1 & 0 & 0 \\ 0 & 0 & l_2 & 0 \\ 0 & 0 & 0 & l_2 \end{bmatrix}\begin{pmatrix} p[k] - \hat{p}[k] \\ q[k] - \hat{q}[k] \\ p[k] - \hat{p}[k] \\ q[k] - \hat{q}[k] \end{pmatrix} \tag{4.23}$$

where $E = \begin{bmatrix} 1 - \frac{T_s R_{g,no}}{L_{g,no}} & -T_s\omega_g & -\frac{T_s}{L_{g,no}} & 0 \\ \omega_g T_s & 1 - \frac{T_s R_{g,no}}{L_{g,no}} & 0 & -\frac{T_s}{L_{g,no}} \\ 0 & 0 & 1 & 0 \\ 0 & 0 & 0 & 1 \end{bmatrix}$, and the gains (l_1, l_2) of the observer can be selected by the pole placement method [85], and $\hat{\zeta}$, $\zeta \in \{p, q, g_p, g_q\}$ represents the

estimated variable. Deadbeat control is to calculate the desired variables by presuming that the system attains the intended behavior at the very end of every control period. Hence the desired voltage vector can be calculated by bringing $p[k+1] = P^*$ and $q[k+1] = Q^* = 0$ into (4.22)

$$
\begin{aligned}
\vec{u}_{\alpha\beta}[k] =& \vec{e}_{\alpha\beta}[k] - \frac{2L_{g,no}}{3T_s \|\vec{e}_{\alpha\beta}[k]\|^2}
\begin{bmatrix} e_\alpha[k] & e_\beta[k] \\ e_\beta[k] & -e_\alpha[k] \end{bmatrix} \\
& \cdot \begin{pmatrix} P^* - p[k] + \frac{T_s R_{g,no}}{L_{g,no}} p[k] + T_s \omega_g q[k] + \frac{T_s}{L_{g,no}} \hat{g}_p[k] \\ Q^* - q[k] + \frac{T_s R_{g,no}}{L_{g,no}} q[k] - T_s \omega_g p[k] + \frac{T_s}{L_{g,no}} \hat{g}_q[k] \end{pmatrix} .
\end{aligned}
\tag{4.24}
$$

The error caused by the mismatched parameters is considered as the disturbance to correct the expression of the desired converter voltage, thereby providing a robust control. The implementation of P-DBPC with disturbance observer within instant k is described as follows. Firstly, $p[k]$ and $q[k]$ are computed according to the measured $\vec{e}_{\alpha\beta}[k]$ and $\vec{i}_{\alpha\beta}[k]$. $\hat{g}_p[k]$ and $\hat{g}_q[k]$ in (4.24) are estimated disturbances that are already obtained in the interval of $[k-1, k]$. Then with the above values, the desired converter voltage $\vec{u}_{\alpha\beta}[k]$ can be calculated by bringing updated P^* and Q^* into (4.24). Besides, in order to prepare the calculation for the next instant (i.e., instant $k+1$), $\hat{p}[k+1]$, $\hat{q}[k+1]$, $\hat{g}_p[k+1]$, and $\hat{g}_q[k+1]$ should be predicted based on (4.23) where $\hat{p}[k]$ and $\hat{q}[k]$ are already obtained in the interval of $[k-1, k]$. Since $\hat{g}_p[k]$ and $\hat{g}_q[k]$ are obtained from the last interval, both $\hat{g}_p[0]$ and $\hat{g}_q[0]$ equal 0 in the calculation of $\vec{u}_{\alpha\beta}[0]$ within the initial instant $k = 0$. Finally, through synthesizing and applying the calculated $\vec{u}_{\alpha\beta}[k]$, the active and reactive power can reach their references without steady-state error.

4.4.3 Description of A-SVPWM
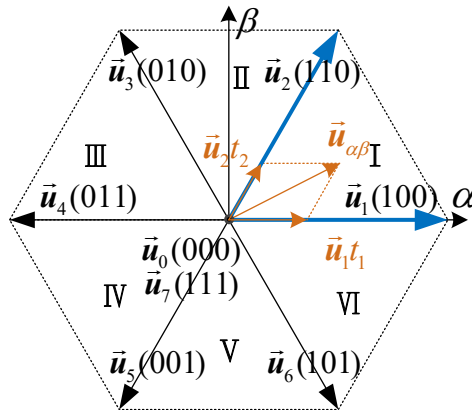
Figure 4.3: Base vectors and sector division.

$\vec{u}_{\alpha\beta}[k]$ should be applied to the VSR through SVPWM. The base vectors and sector division of SVPWM are shown in Fig. 4.3. The switching patterns of conventional C-SVPWM when $\vec{u}_{\alpha\beta}[k]$ locates inside sector I are presented in Fig. 4.4(a), and there are eight switching patterns within a control period (T_s). t_0, t_1, and t_2 represent the dwell time for zero voltage vectors ($\vec{u}_0$ and $\vec{u}_7$), $\vec{u}_1$, and $\vec{u}_2$, respectively. Beginning and ending with the zero-voltage vector $\vec{u}_0$ (000),
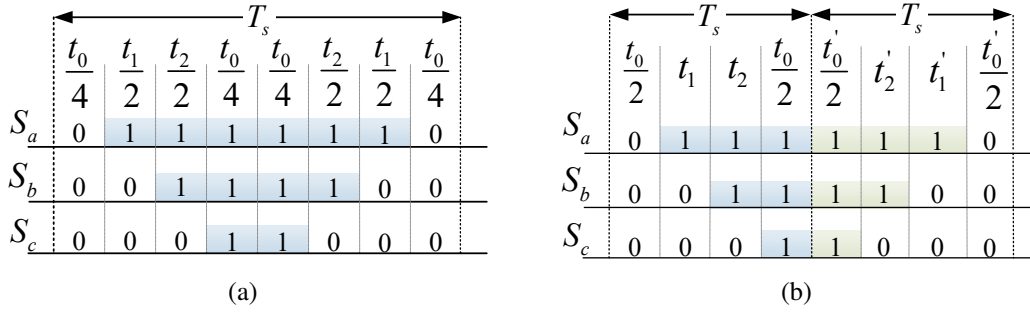
Figure 4.4: Switching patterns if $\vec{u}_{\alpha\beta}[k]$ locates in sector I. (a) Conventional C-SVPWM. (b) Improved A-SVPWM.

the C-SVPWM implements the other zero-voltage vector $\vec{u}_7$ (111) in the middle of T_s. Thus, the switching frequency of the C-SVPWM equals the control frequency, namely, $1/T_s$.

To lower the switching frequency of the conventional C-SVPWM, an A-SVPWM is developed. Until the implementation of the selected base vectors, each application step of the improved A-SVPWM is identical to that of the conventional C-SVPWM. Fig. 4.4(b) illustrates the switching patterns of the improved A-SVPWM when $\vec{u}_{\alpha\beta}[k]$ locates within sector I. If the switching pattern of $\vec{u}_{\alpha\beta}[k]$ starts with (000) and ends with (111), then the switching pattern of $\vec{u}_{\alpha\beta}[k+1]$ should start with (111), and end with (000). It can be found that the selected base vectors are only implemented once in a control period of A-SVPWM. Though the firing pulse is asymmetric in one control period, it is nearly symmetric in two consecutive control periods as the duty cycles will not alter much within two consecutive control periods in steady-state operation. It can be concluded that the switching frequency of A-SVPWM is $1/2T_s$, which is half of that of the conventional C-SVPWM. This modulation method can be widely applied to the algorithms with SVPWM for switching loss reduction.

4.4.4 Design of the speed controller
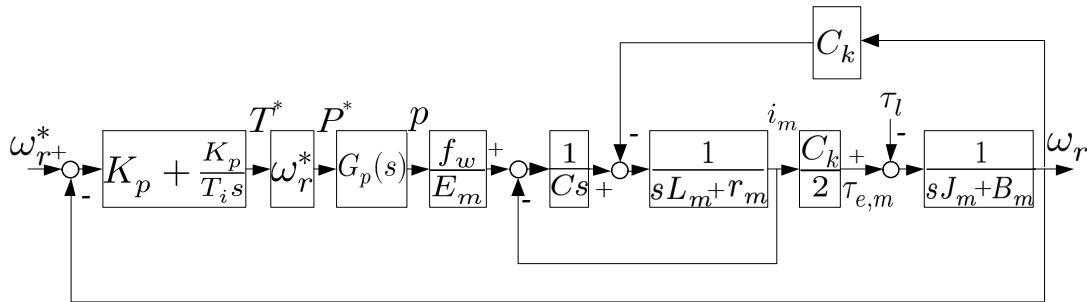
Figure 4.5: Block diagram of high-speed SRM drive based on P-DBPC.

The system block diagram is presented in Fig. 4.5. A PI controller is adopted for speed regulation

$$T^* = k_p e + \frac{k_p}{T_i} \int e \, dt, \qquad e = \omega_r^* - \omega_r \qquad (4.25)$$

with transfer function $F(s) = k_P(1 + 1/(T_i s))$ is used. The relationship between active power p and d-axis component of grid-side current in the proposed system can be expressed as below through applying the magnitude-invariant version of Clarke transformation and Park transformation to (4.17)

$$i_d = \frac{2p}{3E_m} \tag{4.26}$$

where E_m represents the amplitude of the grid-side voltage. With the control frequency of 20 kHz, the actual active power in P-DBPC can track the active power reference with fast response by directly calculating the desired converter voltages, so the transfer function of the deadbeat control can be modeled as unity gain [86]$-$[87], namely, $G_p(s) = 1$. For point p on DC-link shown in Fig. 4.1, the following current expression holds [88]

$$\frac{dv_{DC}}{dt} = \frac{3f_\omega i_d}{2C} - \frac{i_m}{C} \tag{4.27}$$

where $f_\omega \in [0, 1]$ is a constant in steady condition [64], C represents the capacitance of the DC-link capacitor. The electromagnetic torque of SRM can be expressed by [66]

$$\tau_{e,m} = \frac{1}{2}C_k i_m \tag{4.28}$$

where $C_k = \frac{d\psi_m}{d\theta_r}$. Then, given the system parameters, the open-loop transfer function can be derived as

$$F_{ol}(s) = \frac{k_P(T_i s + 1)}{T_i s} \frac{k_A}{k_B s^2 + k_C s} \tag{4.29}$$

where $k_A = \frac{C_k \omega_r^* f_\omega}{2}$, $k_B = Cr_m J_m E_m$, $k_C = \frac{C_k^2 E_m C}{2} + J_m E_m$. To ease the analysis, (4.29) is rewritten into the form expressed by the multiplication of three terms:

$$F_{ol}(s) = G_{ol}(s)H_{ol}(s)I_{ol}(s) \tag{4.30}$$

where $G_{ol}(s) = \frac{k_A}{k_C} \frac{k_P(T_i s+1)}{T_i s}$, $H_{ol}(s) = \frac{1}{s}$, $I_{ol}(s) = \frac{1}{\frac{k_B}{k_C}s+1}$. In light of [67] and [89], a maximum phase margin φ_m can show at the crossover frequency $\omega_{f,c}$ of $F_{ol}(s)$ in the phase frequency characteristic by making sure the following expressions hold

$$\omega_{g,c} = \frac{1}{\gamma}\omega_{f,c} = \frac{1}{T_i} \tag{4.31}$$

$$\omega_{i,c} = \gamma\omega_{f,c} = \frac{k_C}{k_B} \tag{4.32}$$

where $\omega_{g,c}$, $\omega_{i,c}$ represent the crossover frequency of $G_{ol}(s)$ and $I_{ol}(s)$, respectively, and γ is generally within the interval of [2, 4]. Thus, combining (4.31) and (4.32) gives the integral time constant of the speed PI controller

$$T_i = \gamma^2 \frac{k_B}{k_C}. \tag{4.33}$$

Since $|F_{ol}(j\omega_{f,c})| = |G_{ol}(j\omega_{f,c})H_{ol}(j\omega_{f,c})I_{ol}(j\omega_{f,c})| = 1$ at $\omega_{f,c}$, the following expression holds

$$\frac{k_P k_A}{k_C} = \frac{k_C}{\gamma k_B}. \tag{4.34}$$

(4.34) gives the proportional gain of the speed PI controller

$$k_P = \frac{k_C^2}{\gamma k_A k_B}. \tag{4.35}$$

4.4.5 Analysis of power flow in the proposed system

In the proposed drive system, SRM drive can be regarded as the load of the VSR, so the output active power of VSR (denoted as P_{VSR}) is the sum of the active power consumed by DC-link capacitors (denoted as P_C) and the active power consumed by SRM drive (denoted as P_M), i.e., $P_{VSR} = P_M + P_C$. Suppose $P_{VSR} > P_M$, the DC-link voltage will increase since $P_C > 0$. Then, P_M will increase since the DC-link voltage is applied to the winding terminal in every conduction region, and the increased P_M will reduce P_C. The P_M will continue to rise until $P_{VSR} = P_M$, i.e., $P_C = 0$. Similarly, suppose $P_{VSR} < P_M$, the DC-link voltage will decrease since $P_C < 0$. Then, P_M will decrease, which makes P_C gradually approach zero, and P_M will stop decreasing when $P_{VSR} = P_M$. It can be found that P_{VSR} always can regulate P_M, and constant P_{VSR} indicates constant P_M. Based on the above, the SRM is proposed to be regulated by directly controlling the active power flowing to the motor side. Specifically, the torque reference T^* obtained from the speed controller is multiplied by the motor angular velocity ω_r to compute the active power reference P^*, and P^* is supplied by VSR through the active power control in P-DBPC. In this way, a direct connection of power between the front-end VSR and back-end SRM is built. The P-DBPC can make sure the active power flowing to the motor side follows the reference P^*. The energy feedback can be fulfilled so that the excess active power can be transferred back to the grid. The improvements in grid-side power factor and current harmonics can be realized by further setting $Q^* = 0$ in P-DBPC.

4.5 Simulation evaluation

Fig. 4.6 illustrates the simulation results of the loading and unloading processes. During the loading process, it is essential to maintain a stable speed. Therefore, the input active power is increased, and the DC-link voltage is subsequently increased to maintain a stable speed. The increase in input power is required to compensate for the additional load placed on the system. Similarly, during the unloading process, the system should maintain a stable speed. To achieve this, the input active power is decreased, and the DC-link voltage is decreased accordingly. It is worth noting that the control of the loading and unloading process is critical for the proper functioning of the system. A stable speed ensures that the system remains within its operating limits and avoids any overloading or underloading conditions that may cause damage to the system. Therefore, precise control of the input active power is necessary to ensure the reliability of the system. The simulation results demonstrate the effectiveness of the control strategy employed in maintaining stable speed during the loading and unloading processes.
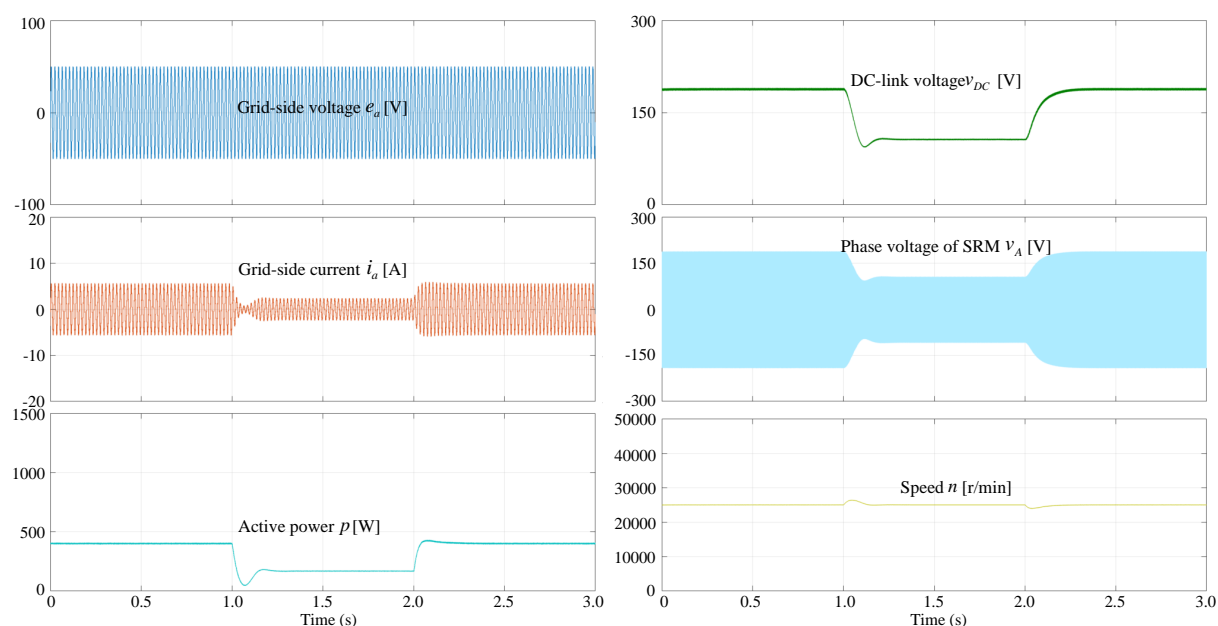
Figure 4.6: Simulation waveforms at 25000 r/min when torque changes from 0.12 N·m to 0.06 N·m to 0.12 N·m.

4.6   Experimental evaluation

4.6.1   Testbench parameters and pseudocode
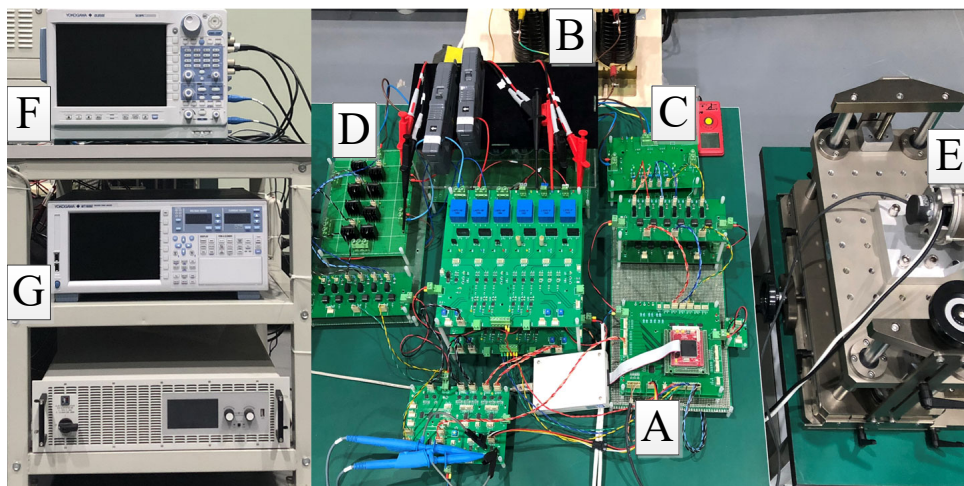
Figure 4.7: Experimental testbench of the high-speed SRM drive based on P-DBPC. (A) TMS320F28335-based controller. (B) Filter inductor. (C) VSR. (D) AHBC. (E) 4/2 SRM. (F) Oscilloscope DL850. (G) Power analyzer WT1800.

A practical laboratory setup is constructed to validate the effectiveness of the proposed control system. Fig. 4.7 and Table 4.1 present the photograph and hardware configuration of the constructed testbench, respectively. A fan is employed as the load in this high-speed SRM drive

Table 4.1: Hardware configuration high-speed SRM drive system based on P-DBPC

Function	Producer	Type
DSP	TEXAS INSTRUMENTS	TMS320F28335
VSR	INFINEON	FS100R06
IGBT	IXYS	IXGH60N60
Fast recovery diodes	IXYS	DSEI60-06A
High-speed incremental encoder	HEIDENHAIN	ERO1420

Table 4.2: Testbench parameters of high-speed SRM drive system based on P-DBPC

Description	Parameter	Value
Grid-side voltage frequency	$\omega_r(\mathrm{rad/s})$	100π
Grid-side filter resistance	$R_{g,no}(\Omega)$	0.3
Grid-side phase voltage	$e_g(\mathrm{V})$	50
Grid-side filter inductor	$L_{g,no}(\mathrm{mH})$	2
DC-link capacitor	$C(\mu\mathrm{F})$	1360
Control period	$T_s(\mu\mathrm{s})$	50
Rated torque of the high-speed SRM	$\tau_{e,m}(\mathrm{N}\cdot\mathrm{m})$	0.12
Rated speed of the high-speed SRM	$n_r(\mathrm{r/min})$	25000

system. The load torque is proportional to the square of the speed for the fan-loaded system, and the torque values at different operating speeds are presented in Fig. 4.8. The experimental parameters concerning the drive system are given in Table 4.2, and the control frequency equals the sampling frequency in the experiments. The necessary implementation steps of the proposed high-speed SRM drive based on P-DBPC during kth interrupt are listed as the following quasi-code:

A-SVWPM should be implemented to make sure $\vec{u}_{\alpha\beta}[k]$ can be applied, and its steps are listed as the following quasi-code:

4.6.2 Experimental results

4.6.2.1 Steady-state performances

The steady-state waveforms of the proposed system when the high-speed SRM operates at 20000 r/min are shown in Fig. 4.9. The general deadbeat control cannot ensure that the actual power follows its reference since the steady-state error caused by the parameter mismatch often exists in the system [90], [91]. However, in the proposed system, the reactive power fluc-
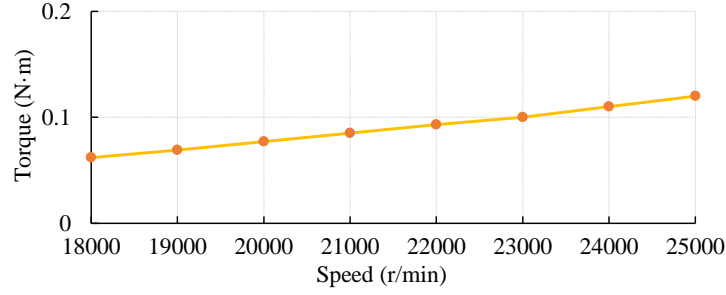
Figure 4.8: Torques of the proposed drive system.

1: **function** Proposed P-DBPC ($\vec{e}_{\alpha\beta}[k]$, $\vec{i}_{\alpha\beta}[k]$, $\theta_r[k]$, k)

2:      **if** $\theta_{m,on} \le \theta_r[k] \le \theta_{m,off}, m \in A, B$ **then**
3:          Set $S_{m1} = 1$; $S_{m2} = 1^1$
4:      **else then**
5:          Set $S_{m1} = 0$; $S_{m2} = 0^2$
6:      **end if**
7:      Estimate $\omega_r[k]$
8:      Refresh $T^*[k]$
9:      Calculate $P^* = \omega_r[k]T^*[k]$
10:     Calculate $p[k]$ and $q[k]$ according to (4.17)
11:     Calculate $\vec{u}_{\alpha\beta}[k]$ according to (4.24)

12:     Estimate $\hat{p}[k+1]$, $\hat{q}[k+1]$, $\hat{g}_p[k+1]$, and $\hat{g}_q[k+1]$ according to (4.23)
13:     Implement A-SVPWM
14: **end function**

---

[1] Turn on the switch of phase m of SRM. [2] Turn off the switch of phase m of SRM.

tuates around 0 Var, and its ripple is controlled within ± 10 Var during the operation of SRM. The phase of grid-side current is almost the same as that of the grid-side voltage. To afford the high-speed operation of 20000 r/min, the active power is controlled to around 190 W, and stable DC-link voltage, whose ripple is within ± 0.9 V according to the waveform, is realized. The SRM is well regulated, and its phase current is around 4.7 A in this operating condition.

Fig. 4.10 gives the steady-state waveforms of the proposed system in the rated operating condition, namely, 25000 r/min. The ripple of DC-link voltage is regulated to around ± 1 V. An enlarged image of the DC-link voltage ripple marked by dashed rectangular is shown on the right side of Fig. 4.10. It can be found that the fluctuation frequency of the DC-link voltage is twice the electrical frequency (defined as the reciprocal of electrical period) of SRM. A fluctuation period can be divided into three sections in view of the variation trend. In section "ab", the energy stored in the magnet field of the motor flows back to the capacitor due to the demagnetization of phase winding, which leads to the rise of DC-link voltage. The winding current descends quickly within a short time after being switched off, so the energy flowing back is relatively big. In section "bc", the rotor position goes into the maximum inductor region, so the drop of winding current becomes slow, which reduces the rising rate of the DC-link voltage.

1: **function** A-SVPWM[1] $(\vec{u}_{\alpha\beta}[k],\ k^2)$

2:      Judge the sector where $\vec{u}_{\alpha\beta}[k]$ locates
3:      Calculate the duty ratio $d_{x1}[k]$ for $s_{x1}, x \in \{a, b, c\}$
3:      **if** $(k\%2) == 1$ **then**
4:          CMPA[3] $= d_{x1}[k]$ TBPRD[3]
5:      **else then**
6:          CMPA $= (1 - d_{x1}[k])$ TBPRD
7:      **end if**
8:      AQCTLA[3] [CAU] = 0x3
9:      $k = k + 1$
10: **end function**

---

[1] TBCTL[CTRMODE], CMPCTL[SHDWBMODE], and CMPCTL [LOADAMODE] bit should be particularly configured to 0 in program header file of TMS320F28335.

[2] k, whose default value is 0, counts the number of interrupts.

[3] The registers in the enhanced pulse width modulator module of TMS320F28335.
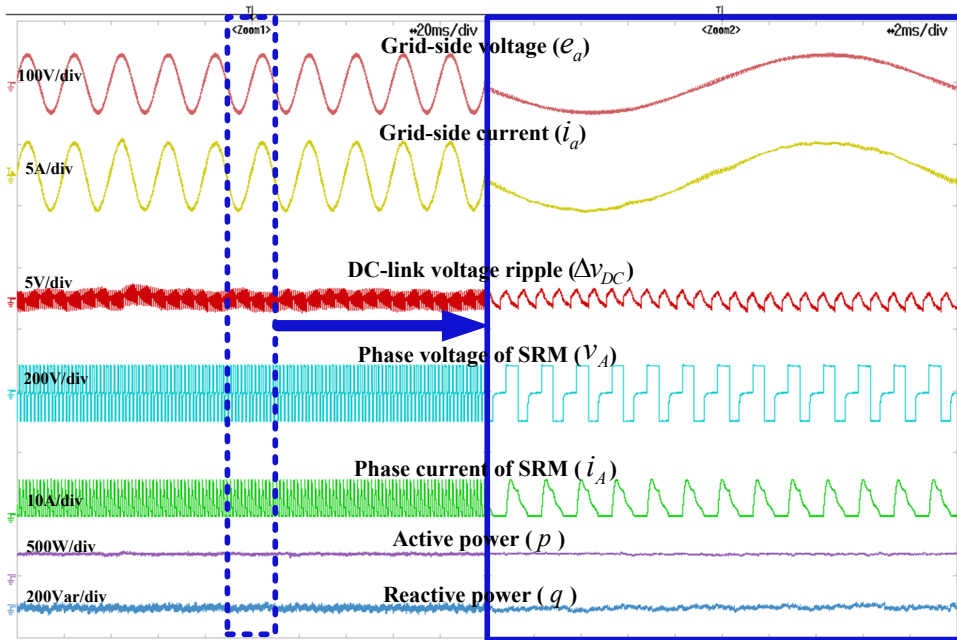
Figure 4.9: Steady-state experiment results of proposed system at 20000 r/min.

In section "cd", the DC-link voltage declines due to the current establishment of the incoming phase. At the rated operating condition, the active power is about 390 W, and the reactive power has been controlled within ±30 Var for power quality enhancement.

The improved A-SVPWM described before is applied to the proposed system, and its related waveforms at the rated operating condition are presented in Fig. 4.11. The pulse named "control signal" is generated in every interrupt of the controller to intuitively reflect the control frequency of the proposed system, namely, 20 kHz, and its High logic state represents the execution time of the interrupt function. As has been analyzed before, the switching frequency of power switches
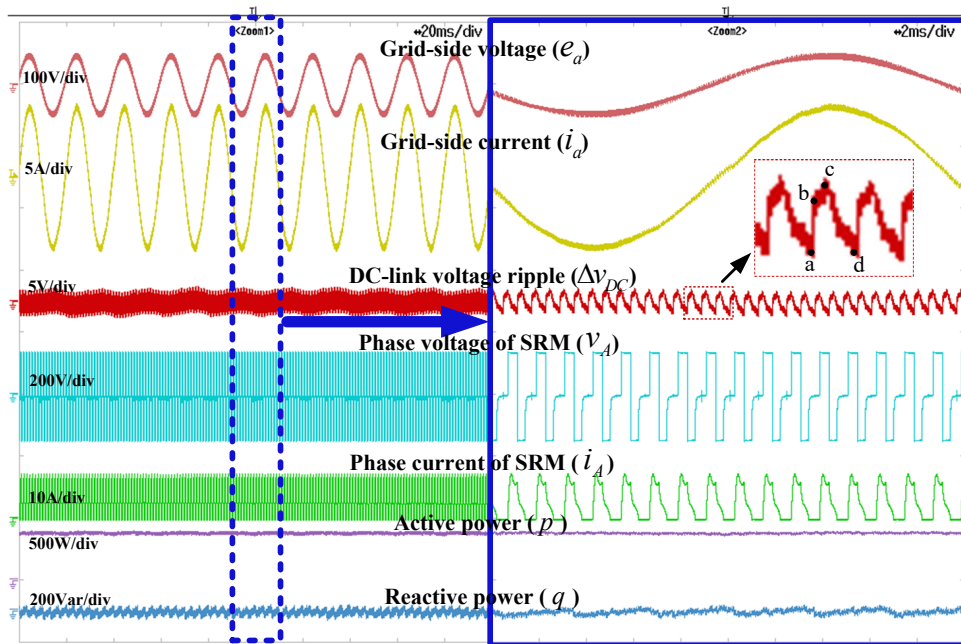
Figure 4.10: Steady-state experiment results at 25000 r/min.
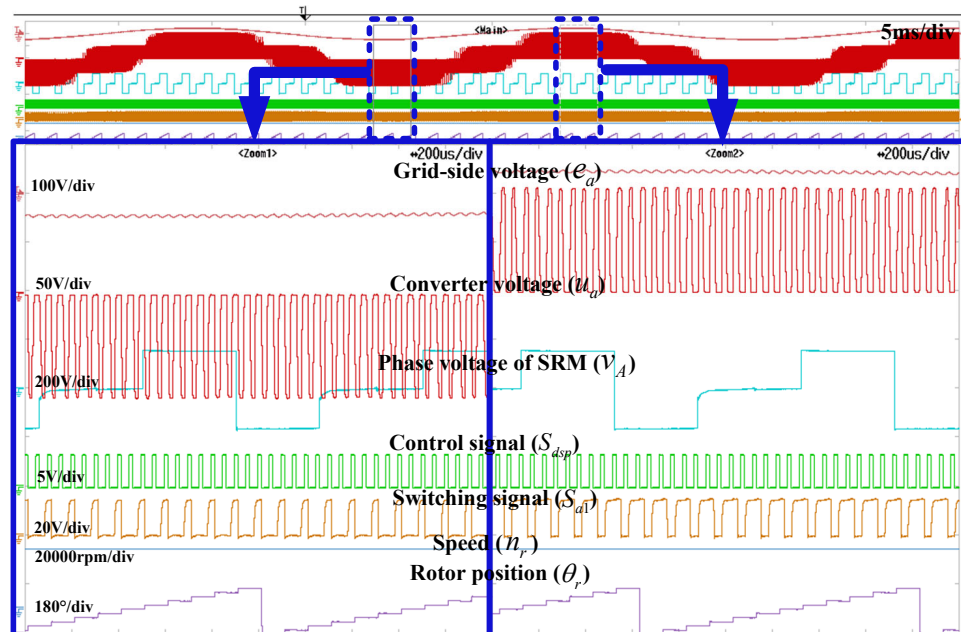
Figure 4.11: Experimental waveforms related to the improved A-SVPWM at 25000 r/min.

would equal control frequency if the conventional C-SVPWM were employed. However, it can be seen from the switching signal in the figure that the switching frequency of the power switch in A-SVPWM has been reduced to 10 kHz by changing the execution order of the selected base vectors. In the experiments, the measured interrupt execution time of the proposed control strategy with C-SVPWM and A-SVPWM are almost the same, both of which are around 16 us. Therefore, without causing extra computational burden to the controller, A-SVPWM can

effectively reduce its switching frequency to half of that of the C-SVPWM.
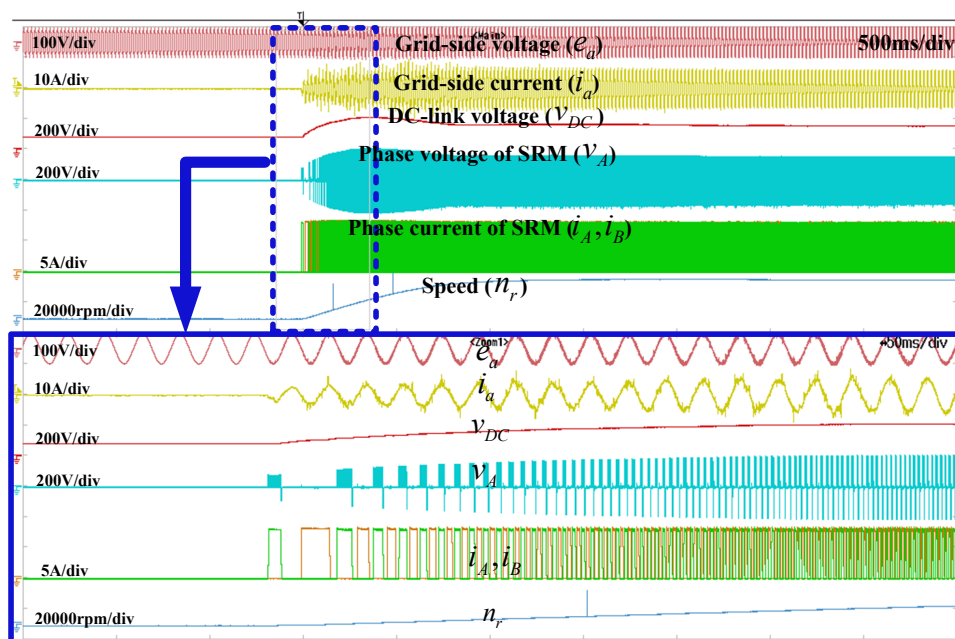
Figure 4.12: Dynamic test results when the SRM starts from standstill to 25000 r/min.

4.6.2.2 Transient-state performances

Fig. 4.12 shows the dynamic test waveforms of the proposed system when SRM starts from standstill to the rated operating condition. As can be clearly observed from the enlarged window at the lower part of the figure, the grid-side current presents sine quality from the beginning. The speed steadily rises, and it goes into steady state after approximately 1 s. At the very beginning of the starting, the winding current of the motor has reached the protection threshold, namely, 7.5 A, so it is chopped by hardware overcurrent protection.

The dynamic test results of the proposed system when the motor is commanded to accelerate and decelerate are shown in Fig. 4.13 and Fig. 4.14, respectively. In the figures, the short line on the left-hand side of the active power curve implies 0 W. When the speed command is adjusted from 20000 r/min to 25000 r/min, the active power is increased to supply more energy for the SRM, and the DC-link voltage is risen from 100 V to 160 V, accordingly. During this process, the sinusoidal gird-side voltage and current are in phase, and the phase current of SRM has been increased to around 7 A. At the instant of deceleration in Fig. 4.14, a negative active power reference is generated. In order to follow the negative active power reference, the direction of the grid-side current flow is changed from the positive direction (namely, being in phase with the grid-side voltage) to the negative direction (namely, having a phase shift of 180° with the grid-side voltage) to produce the negative instantaneous active power. In this way, the speed is quickly decreased by feeding the excess energy back toward the grid side.

The curves of speed and the error between the actual and reference speed during speed regulation are shown in Fig. 4.15. The red line on the left side of the curve of speed error indicates 0 r/min. The maximal speed error that can be displayed is 100 r/min due to the output limitation of the digital-to-analog chip. The speed can be well regulated in the proposed SRM drive
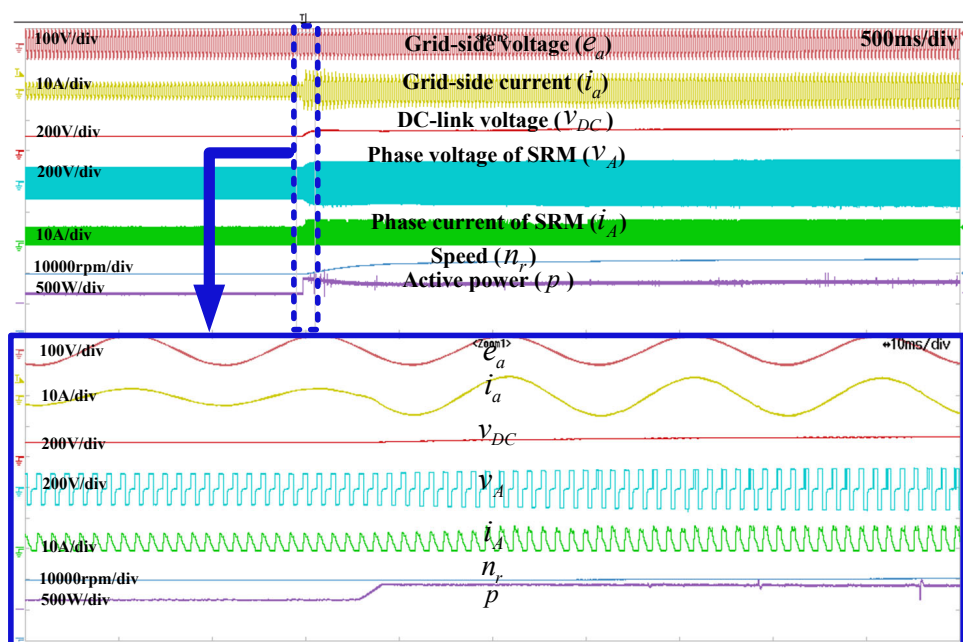
Figure 4.13: Experimental results when SRM speed changes from 20000 to 25000 r/min.
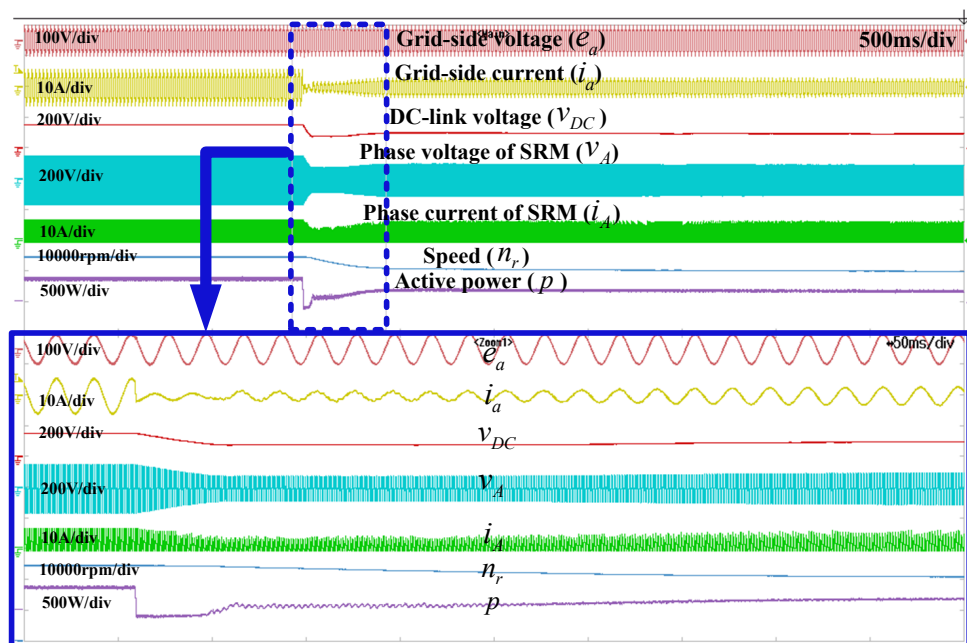
Figure 4.14: Dynamic test results when SRM speed changes from 25000 to 20000 r/min.

system, and the speed tracking error is within ± 15 r/min in the steady state.

4.6.2.3   Parameter sensitivity

The parameter sensitivity experiments are performed, and the experimental waveforms, screenshots of power analyzer, and current harmonic analysis are presented in Fig. 4.16, Fig. 4.17,
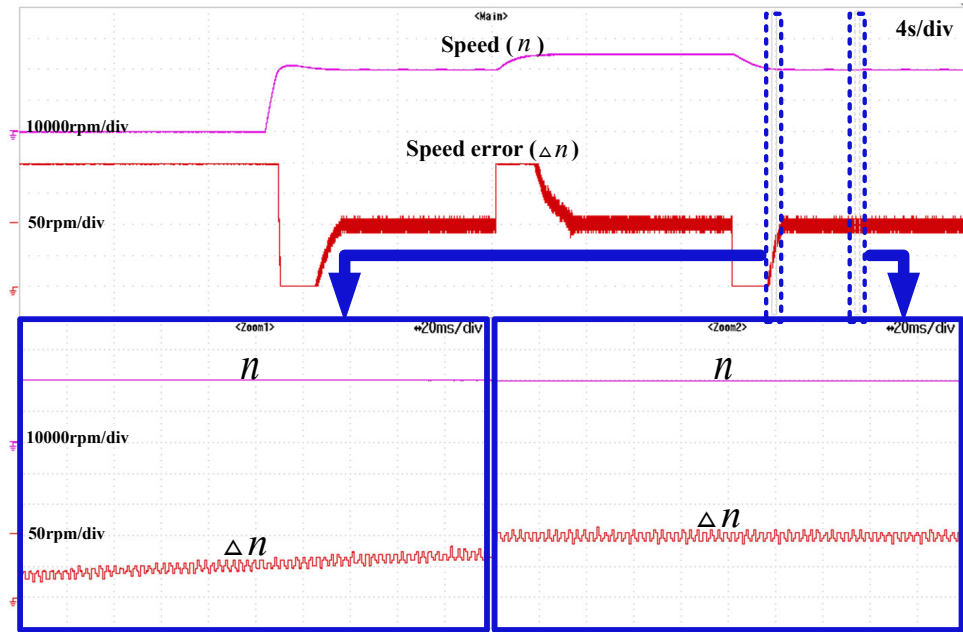
Figure 4.15: Dynamic test results when SRM speed changes from 0 r/min to 20000 r/min to 25000 r/min to 20000 r/min.

and Fig. 4.18, respectively. In the experiments, three pairs of mismatched parameters are configured when the SRM runs in its rated operating condition to test the system performance. With the disturbance observer, the prediction error caused by the mismatched parameters can be estimated online to compensate for deadbeat control. Therefore, as can be seen from Fig. 4.16, there is still no steady-state error in reactive power even if $L_{g,no}$ and $R_{g,no}$ are decreased to 50 % and increased to 150 % simultaneously in experiments. According to Fig. 4.17 and Fig. 4.18, satisfying power factor $\lambda\Sigma A$ and current THD can be got when the mismatched parameters are used in the system, which proves the validity of the disturbance observer.

4.6.2.4 Performances with C-SVPWM and A-SVPWM

Experimental comparisons have been made to verify the effectiveness of the proposed drive system with conventional C-SVPWM and with the improved A-SVPWM. In the proposed high-speed SRM drive system, control frequency f_{contr} equals sampling frequency f_{samp}. For conventional C-SVPWM, the switching frequency of the power switch equals the control frequency, i.e., $f_{switch} = f_{contr}$. However, the improved A-SVPWM rearranges the execution order of the selected base vectors so that its switching frequency can be reduced to half of its control frequency, i.e., $f_{switch} = 0.5f_{contr}$. Although A-SVPWM reduces its switching frequency to half of that of the C-SVPWM, the applied converter voltage vector is the same for the A-SVPWM and C-SVPWM. Therefore, their control performances on power factor and reactive power are similar at the same control frequency of 20 kHz, which can be seen from Fig. 4.19 and Fig. 4.20. Fig. 4.21 and Fig. 4.22 give the power analyzer screenshots of the proposed drive system with conventional C-SVPWM and improved A-SVPWM at 20 kHz, respectively. In the figures, grid-side active power p, reactive power q, and power factor are denoted by PΣA, QΣA, and

(a)

(b)

(c)
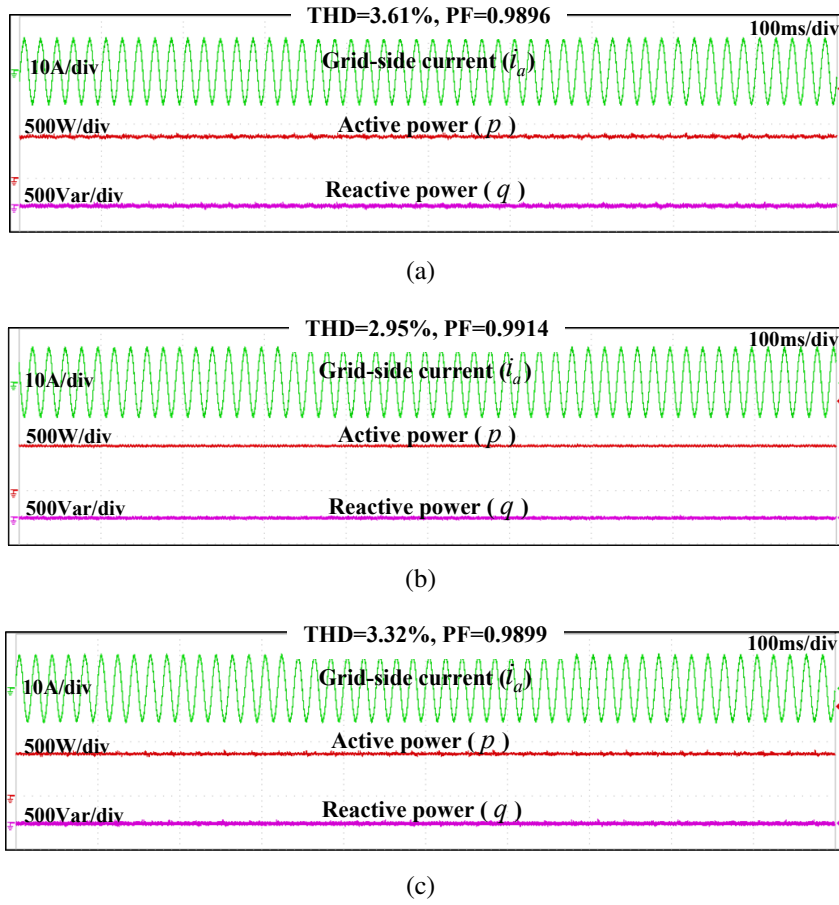
Figure 4.16: Waveforms of parameter sensitivity experiments in the rated operating condition (25000 r/min). (a) $L_{g,no}$ decreases to 50% and $R_{g,no}$ decreases to 50% ($L_{g,no} = 1\text{mH}, R_{g,no} = 0.15\Omega$). (b) $L_{g,no}$ and $R_{g,no}$ are adopted ($L_{g,no} = 2\text{mH}, R_{g,no} = 0.3\Omega$). (c) $L_{g,no}$ increases to 150% and $R_{g,no}$ increases to 150% ($L_{g,no} = 3\text{mH}, R_{g,no} = 0.45\Omega$).

(a)

(b)

(c)
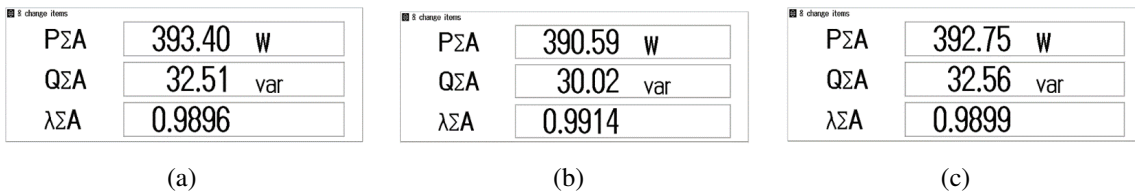
Figure 4.17: Screenshots of power analyzer in parameter sensitivity experiments in the rated operating condition. (a) $L_{g,no}$ decreases to 50% and $R_{g,no}$ decreases to 50% ($L_{g,no} = 1\text{mH}, R_{g,no} = 0.15\Omega$). (b) $L_{g,no}$ and $R_{g,no}$ are adopted ($L_{g,no} = 2\text{mH}, R_{g,no} = 0.3\Omega$). (c) $L_{g,no}$ increases to 150% and $R_{g,no}$ increases to 150% ($L_{g,no} = 3\text{mH}, R_{g,no} = 0.45\Omega$).

$\lambda\Sigma$A, respectively. η_1 denoted the efficiency of the front-end VSR. η_2 denotes the efficiency of whole drive topology. Fig. 4.21 and Fig. 4.22 confirm that C-SVPWM and A-SVPWM can realize similar control performance on reactive power and power factor for the proposed system at the same control frequency of 20 kHz. Nevertheless, compared with C-SVPWM, A-
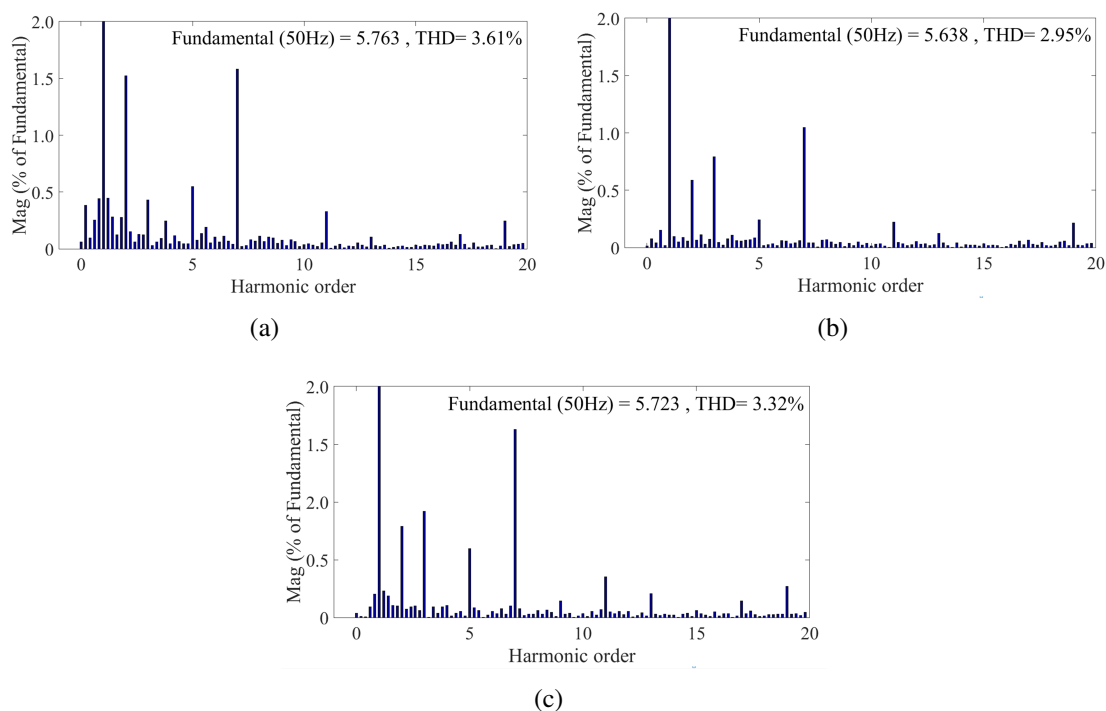
Figure 4.18: Grid-side current harmonic analysis in parameter sensitivity experiments in the rated operating condition. (a) $L_{g,no}$ decreases to 50% and $R_{g,no}$ decreases to 50% ($L_{g,no} = 1\text{mH}, R_{g,no} = 0.15\Omega$). (b) $L_{g,no}$ and $R_{g,no}$ are adopted ($L_{g,no} = 2\text{mH}, R_{g,no} = 0.3\Omega$). (c) $L_{g,no}$ increases to 150% and $R_{g,no}$ increases to 150% ($L_{g,no} = 3\text{mH}, R_{g,no} = 0.45\Omega$).

SVPWM succeeds in improving in the efficiency of VSR (η_1) by reducing switching frequency to 10 kHz, and finally succeeds in reaching a higher η_2, which confirms the practicability of the improved A-SVPWM. At the rated operating condition, there are an increase of 2.419 % on η_1 and an increase of 2.143 % on η_2 for the system with A-SVPWM (Fig. 4.22(h)) compared with the system with C-SVPWM (Fig. 4.21(h)).

In order to test the performances of C-SVPWM and A-SVPWM at the same switching frequency, the control frequency of C-SVPWM should be set to 10 kHz. Fig. 4.23 gives the system experimental waveforms of C-SVPWM at the switching frequency of 10 kHz. Therefore, $f_{\text{contr}} = f_{\text{samp}} = f_{\text{switch}} = 10\text{kHz}$ holds for the system with C-SVPWM, and $f_{\text{contr}} = f_{\text{samp}} = 20\text{kHz}, f_{\text{switch}} = 10\text{kHz}$ hold for the system with A-SVPWM. Higher sampling frequency contributes to higher control accuracy, so more distortion appears on the grid-side current of C-SVPWM shown in Fig. 4.23 , which can be proved by the current THDs analysis shown in Fig. 4.24. Moreover, compared with the efficiency experimental results of A-SVPWM given in Fig. 4.22, the experimental efficiency results of C-SVPWM given in Fig. 4.25 shows higher reactive power and lower power factor.

For the same switching frequency, the control frequency/sampling frequency of A-SVPWM is twice that of the C-SVPWM, so A-SVPWM shows higher control accuracy and better system performance than C-SVPWM. For the same control frequency/sampling frequency, while achieving the almost same control performance as the C-SVPWM, A-SVPWM can reduce its switching frequency to half of that of the C-SVPWM, which indicates less switching loss and
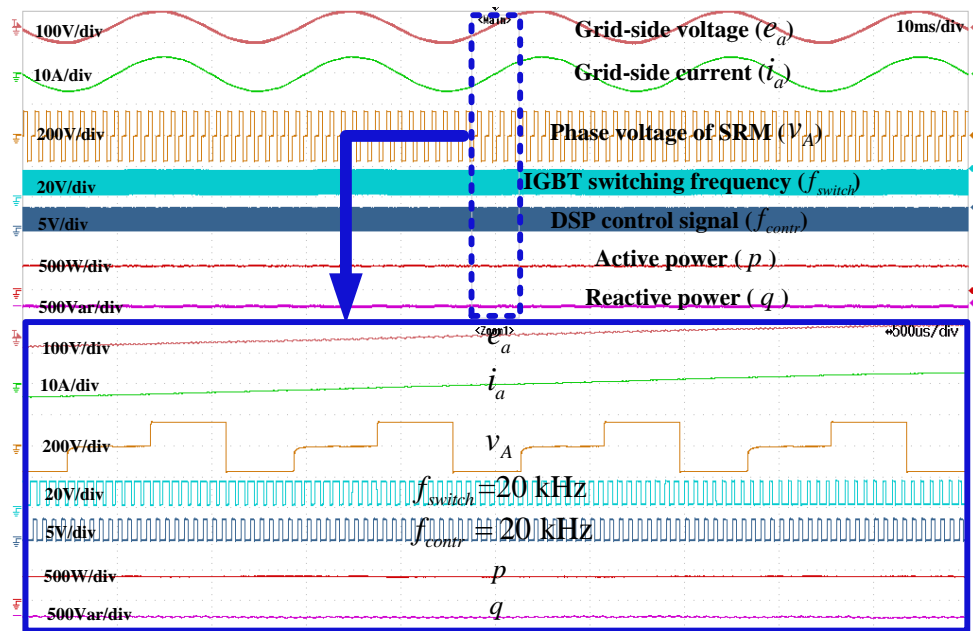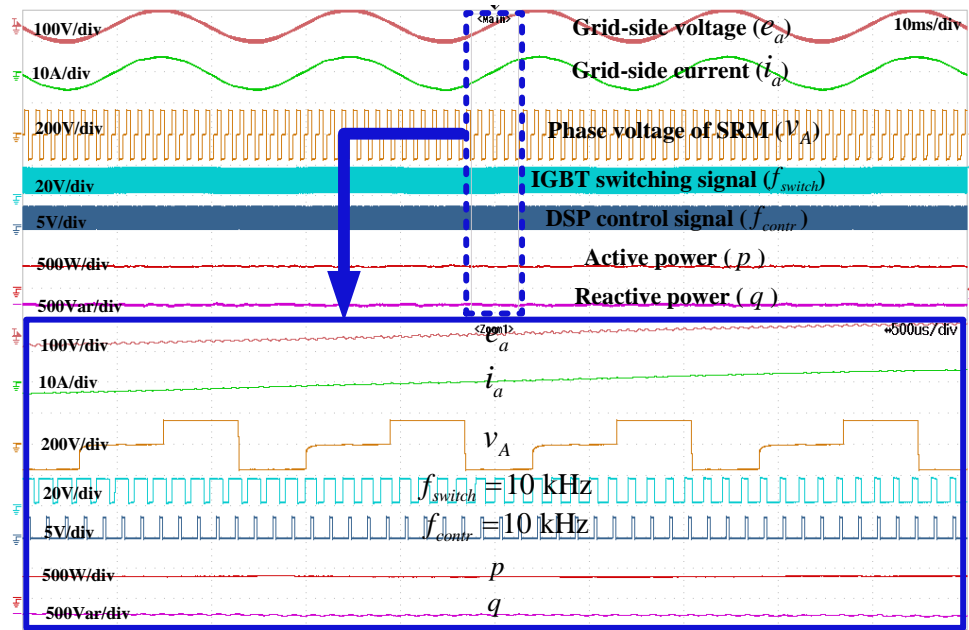
Figure 4.19: Experimental waveforms of C-SVPWM ($f_{\text{contr}}=f_{\text{switch}}=20$ kHz) in the rated operating condition (25000 r/min).
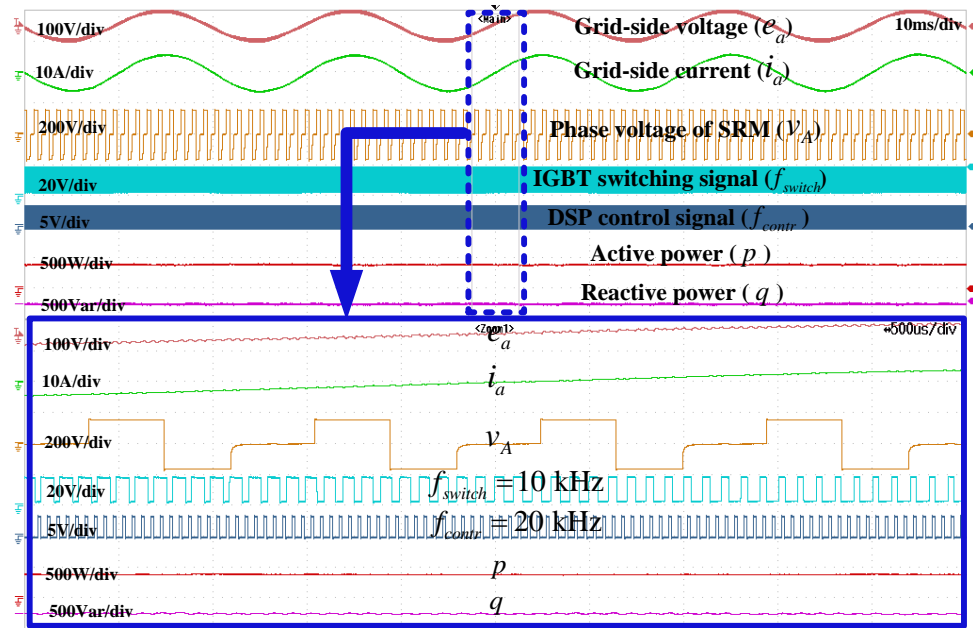

Figure 4.20: Experimental waveforms of A-SVPWM ($f_{\text{contr}}=20$ kHz, $f_{\text{switch}}=10$ kHz) in the rated operating condition (25000 r/min).

higher efficiency than the C-SVPWM.

PΣA	143.20 W	PΣA	168.81 W	PΣA	196.94 W	PΣA	227.26 W
QΣA	1.54 var	QΣA	1.38 var	QΣA	−2.90 var	QΣA	7.14 var
λΣA	0.9929	λΣA	0.9956	λΣA	0.9937	λΣA	0.9936
η1	94.500 %	η1	94.485 %	η1	93.096 %	η1	92.097 %
η2	86.652 %	η2	86.223 %	η2	86.323 %	η2	86.295 %
(a)		(b)		(c)		(d)	
PΣA	261.98 W	PΣA	301.19 W	PΣA	349.09 W	PΣA	400.04 W
QΣA	−12.15 var	QΣA	−17.35 var	QΣA	23.91 var	QΣA	29.97 var
λΣA	0.9915	λΣA	0.9898	λΣA	0.9872	λΣA	0.9917
η1	92.347 %	η1	91.896 %	η1	91.235 %	η1	90.452 %
η2	86.060 %	η2	86.108 %	η2	85.597 %	η2	85.585 %
(e)		(f)		(g)		(h)	

Figure 4.21: Screenshots of power analyzer in the proposed drive system with conventional C-SVPWM ($f_{contr} = f_{switch}$=20 kHz). (a)-(h) 18000 r/min-25000 r/min with the interval of 1000 r/min.

PΣA	143.57 W	PΣA	163.08 W	PΣA	190.50 W	PΣA	220.51 W
QΣA	2.39 var	QΣA	−2.49 var	QΣA	−1.32 var	QΣA	5.37 var
λΣA	0.9920	λΣA	0.9956	λΣA	0.9973	λΣA	0.9949
η1	95.040 %	η1	94.539 %	η1	94.999 %	η1	94.115 %
η2	88.742 %	η2	88.257 %	η2	88.130 %	η2	88.212 %
(a)		(b)		(c)		(d)	
PΣA	251.60 W	PΣA	291.48 W	PΣA	340.64 W	PΣA	390.59 W
QΣA	−9.92 var	QΣA	15.52 var	QΣA	−22.82 var	QΣA	30.02 var
λΣA	0.9939	λΣA	0.9919	λΣA	0.9893	λΣA	0.9914
η1	94.269 %	η1	93.671 %	η1	93.632 %	η1	92.871 %
η2	88.382 %	η2	88.105 %	η2	87.726 %	η2	87.728 %
(e)		(f)		(g)		(h)	
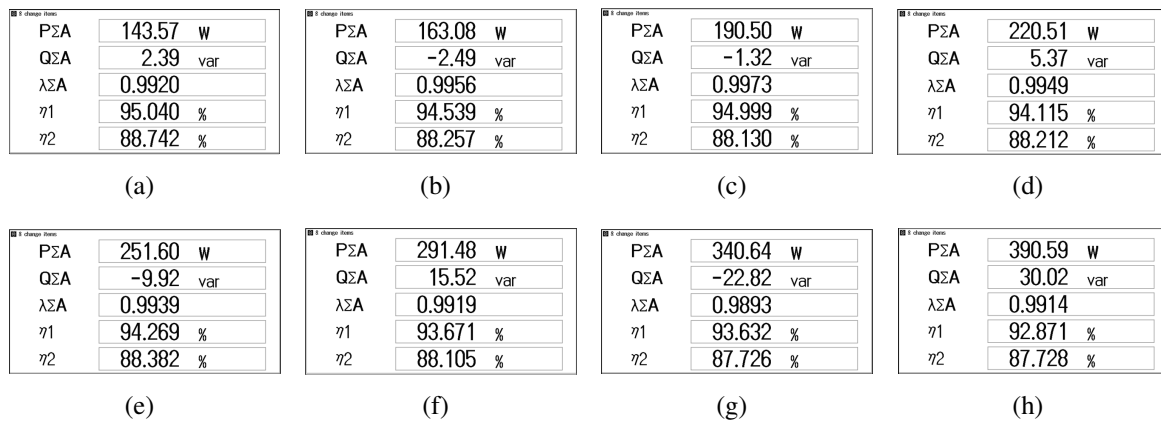
Figure 4.22: Screenshots of power analyzer in the proposed drive system with A-SVPWM (f_{contr}=20 kHz, f_{switch}=10 kHz). (a)-(h) 18000 r/min-25000 r/min with the interval of 1000 r/min.

4.7   Summary

Several drive systems with improved grid-side power quality function are proposed in recent years to drive the SRM. In these systems, the front-end converter and back-end SRM drive are separate modules with their respective control strategies. In these systems, the control strategy of the front-end converter regulates the grid-side power quality, and the control strategy of the SRM drive regulates the SRM speed. Nevertheless, the proposed drive system treats the front-end VSR and the back-end SRM as a whole. Specifically, the output of speed controller of the back-end SRM is torque reference T^*, and the active power reference P^* is obtained by multiplying T^* by the angular velocity ω_r. P^* is the desired active power required by the motor side, and it is directly provided by the front-end VSR through the instantaneous active power control of P-DBPC. In this way, a direct connection of power between the front-end VSR and

Figure 4.23: Experimental waveforms of C-SVPWM ($f_{contr}=f_{switch}=10$ kHz) at the rated operating condition (25000 r/min).
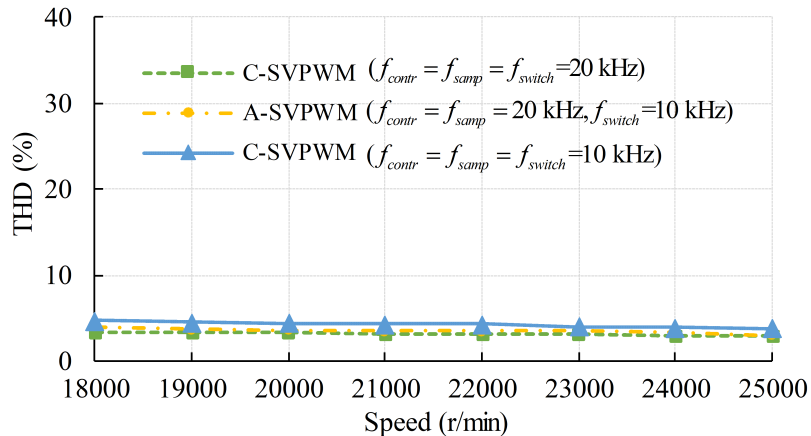
Figure 4.24: Grid-side current THDs.

back-end SRM is built, and the whole system can be controlled by manipulating the power flow. Besides, a real-time correction is implemented for the power expression to eliminate the steady-state bias in power control. Additionally, without causing additional computational burden on the controller, an A-SVPWM is proposed to reduce the switching loss by reducing the frequency of switching action, thereby improving the system efficiency.

Satisfying control performances have been obtained in the experiments. Stable SRM speed is fulfilled by controlling the active power in the system, and the speed tracking error is kept within ± 15 r/min at the rated operating condition of 25000 r/min. Enhanced grid-side power quality is achieved by directly reducing the reactive power. The grid-side power factor has been increased to near 1, and the current distortion has been reduced to below 5 %. At the rated

PΣA	141.36	W
QΣA	1.49	var
λΣA	0.9898	
η1	94.741	%
η2	88.819	%

(a)

PΣA	161.65	W
QΣA	5.14	var
λΣA	0.9895	
η1	94.417	%
η2	88.270	%

(b)

PΣA	190.03	W
QΣA	−4.80	var
λΣA	0.9927	
η1	94.338	%
η2	87.787	%

(c)

PΣA	220.41	W
QΣA	−13.74	var
λΣA	0.9874	
η1	94.037	%
η2	87.531	%

(d)

PΣA	254.06	W
QΣA	−13.03	var
λΣA	0.9909	
η1	93.595	%
η2	87.494	%

(e)

PΣA	294.93	W
QΣA	19.89	var
λΣA	0.9912	
η1	93.352	%
η2	87.536	%

(f)

PΣA	344.41	W
QΣA	26.11	var
λΣA	0.9906	
η1	92.893	%
η2	87.206	%

(g)

PΣA	393.06	W
QΣA	−35.65	var
λΣA	0.9900	
η1	93.100	%
η2	87.473	%

(h)

Figure 4.25: Screenshots of power analyzer in the proposed drive system with C-SVPWM ($f_{\text{contr}} = f_{\text{switch}}$ =10 kHz). (a)-(h) 18000 r/min-25000 r/min with the interval of 1000 r/min.

operating condition, there is an increase of 2.143 % in efficiency in the system using A-SVPWM compared with the system using C-SVPWM.

CHAPTER 5

Cascade-free MP-DPC strategy for grid-connected high-speed SRM system

5.1 Introduction

The double closed-loop control method based on PI controller is the most classical method to regulate the VSR and motor. In this scheme, an outer voltage PI controller is applied to generate power/current reference, and the inner feedforward decoupling controller is applied to achieve reference tracking [92]. However, this linear controller has a limited bandwidth, which tends to present a slow dynamic response. To improve the dynamics, direct power/torque control, which directly selects the optimal vector from a predefined switching table in an intuitive way, is developed in [93], [94] to replace the inner feedforward decoupling controller for reference tracking, but high power/torque ripple can be introduced into system.

Because of the fast dynamic response and flexible integration of various constraints, model predictive control (MPC) has been widely researched [95]. By making use of the inherent discrete nature of power converters, MPC evaluates the effect of each possible switching state on the concerned variables in a predefined criterion and selects the optimal one that can minimize the differences between the concerned variables and their references. In [96], a long-horizon MPC is developed to control the back-to-back PMSG wind turbine system. Since the associated computational burden increases exponentially with the length of the prediction horizon, sphere decoding is used to reduce the computational effort after linearizing the nonlinear equation. Although the increased prediction horizon helps enhance the steady-state control performance, solving the optimization problem is challenging and time-consuming. Thus, the prediction horizon of 1 is the most widely applied [97]. Instead of selecting a certain switching state, the scheme in [98] adopts the switching time in addition to the switching state to minimize the deviations from reference. Though an additional degree of freedom is enabled by choosing a variable switching point, the method complexity is also increased. In [99], a model predictive flux/power control is developed to reduce the computation burden by only evaluating

the switching states selected from the newly-designed switching tables. However, most MPCs in literature, including the references above, are developed as an inner loop of the outer PI controller, thereby forming the conventional PI controller-based model predictive control (PI-MPC). A DC-link voltage PI controller is always necessary to generate reference for MPC to control the back-to-back converter with PI-MPC [100]. It is a cascaded control structure since the inner MPC is nested within the outer voltage PI control loop [101], [102]. To further improve the dynamic response, a cascade-free method without the outer DC-link voltage control loop is developed in [103]. In this method, the power reference inside the cost function is directly obtained based on a power loss-less conversion assumption. Without considering the conduction loss, switching loss, etc., the grid-side active power reference is calculated by adding the estimated load power and capacitor power together, which makes the regulated DC-link voltage lower than its reference. In addition, the voltage control performance is limited by the predefined number of intervals to reach the reference. If a faster tracking response on DC-link voltage is desired, a small value should be chosen for that number, but it will lead to large steady-state voltage ripple and large capacitor current. The study in [104] extends the above concept into a back-to-back converter by developing a quasi-centralized model predictive control (QC-MPC) scheme in which the active power reference inside the cost function is estimated by assuming that the newly-updated voltage reference is reached at the next instant. However, voltage tracking error still exists due to the adoption of the power loss-less model. To solve this problem, the study in [105] compensates for the voltage offset by adding the accumulated error into the active power reference in a revised QC-MPC. The DC-link voltage is regulated by strictly following the specified trajectory of voltage reference and power reference of each instant. However, the response time of this scheme is subject to the reference prediction horizon. A small reference prediction horizon increases the DC-link currents and voltage fluctuation, but a large one prolongs the dynamic response time. In this chapter, a cascade-free MP-DPC is proposed to govern the multi-level converter-fed high-speed SRM drive system. The contributions are as follows:

1) Define a new cost function, thereby removing the conventional cascade control structure.

MPC in literature is generally developed as an inner controller of the outer PI control loop, which forms the conventional PI-MPC. To control the grid-connected SRM drive system with MPC, an outer speed PI controller is necessary to generate power setpoint for inner MPC in conventional control method. However, instead of adopting the cascade control structure, the proposed cascade-free MP-DPC strategy in this chapter directly regulates the speed and power flows within a newly-defined cost function. By evaluating the cost function, the strategy selects the vector which not only will generate a motor speed closer to the setpoint at instant $k+2$, but will generate an active power capable of further reducing that speed error for the future instant. In addition, the term for capacitor voltage balancing control, which is critical to the three-level VSR, is also added into the cost function. Consequently, well-regulated motor speed, balanced capacitor voltage, and controllable power flow can be achieved within one cost function simultaneously.

2) Compensate for errors caused by mismatched parameter.

The mathematical model for prediction is accurate when actual values of inductor and resistor are adopted. However, it is actually the nominal value that are involved in the prediction since the actual values are unknown, and it is also possible that the actual values change during the operation, which causes the steady-state error in the system.

To address this problem, the Kalman filter is added to the proposed strategy. The disturbances caused by mismatched parameters are estimated via Kalman filter and used to correct the power expressions, thus compensating for the steady-state power error.

5.2 Three-level VSR-based drive topology

The drive topology for high-speed SRM drive is depicted in Fig. 5.1, in which a three-level VSR is connected with the split-DC converter to drive the SRM. In the topology, the voltage, current, and converter voltage of the grid side are represented by e, i and u, respectively. The grid-side resistance, inductance, DC-link voltage, capacitor voltage of C_1 and C_2 are represented by R_g, L_g, v_{DC}, v_{c1} and v_{c2}, respectively.

5.2.1 Dynamic models

The operation mode of the VSR depends on the states of power switches. Supposing all power devices are ideal devices, the converter voltage u_i, $i \in a, b, c$ of each phase can be flexibly set to v_{c1}, 0 and $-v_{c2}$ (marked as {+, 0, -} for ease of description) by configuring the switching state s_i of each leg as follows

$$s_i = \begin{cases} +1 & s_{ip} = 1, s_{io} = 0, s_{in} = 0(v_{i1} = 1, v_{i2} = 1, v_{i3} = 0, v_{i4} = 0) \\ 0 & s_{ip} = 0, s_{io} = 1, s_{in} = 0(v_{i1} = 0, v_{i2} = 1, v_{i3} = 1, v_{i4} = 0) \quad i \in \{a, b, c\} \\ -1 & s_{ip} = 0, s_{io} = 0, s_{in} = 1(v_{i1} = 0, v_{i2} = 0, v_{i3} = 1, v_{i4} = 1) \end{cases} \quad (5.1)$$

where $s_i = s_{ip} - s_{in}$ and $s_{ip} + s_{io} + s_{in} = 1$. Hence, there are totally 27 switching states in this VSR, and they can be uniformly expressed as

$$\vec{s}_n = [s_a, s_b, s_c]^\mathrm{T}, n \in \{1, 2, \cdots, 27\} \tag{5.2}$$

As can be seen in Fig. 5.1, the expression below holds

$$\begin{cases} u_{ao} = s_{ap}v_{c1} - s_{an}v_{c2} \\ u_{bo} = s_{bp}v_{c1} - s_{bn}v_{c2} \\ u_{co} = s_{cp}v_{c1} - s_{cn}v_{c2} \end{cases} . \tag{5.3}$$

Based on Kirchhoff's voltage law, the voltage expression can be written as

$$\begin{cases} L_g \frac{di_a}{dt} + R_g i_a + u_{ao} + u_{oN} = e_a \\ L_g \frac{di_b}{dt} + R_g i_b + u_{bo} + u_{oN} = e_b \\ L_g \frac{di_c}{dt} + R_g i_c + u_{co} + u_{oN} = e_c \end{cases} . \tag{5.4}$$

u_{oN} can be obtained by bringing (5.3) into (5.4)

$$u_{oN} = \frac{\left(-s_{ap} - s_{bp} - s_c\right) v_{c1} + \left(s_{an} + s_{bn} + s_{cn}\right) v_{c2}}{3} \tag{5.5}$$
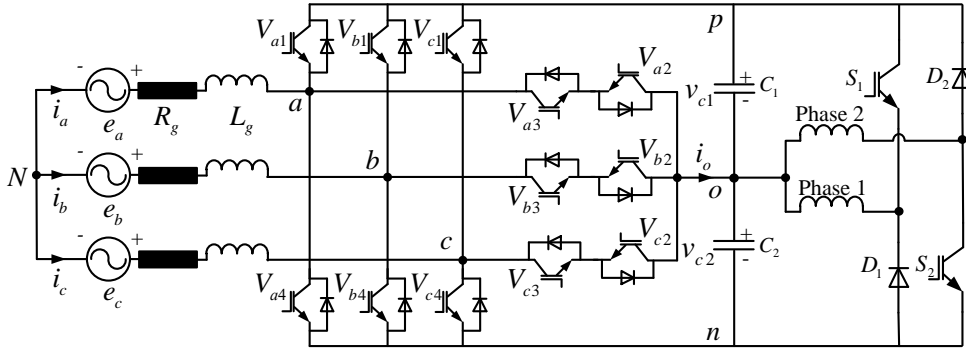
Figure 5.1: Three-level VSR-based high-speed SRM drive topology.
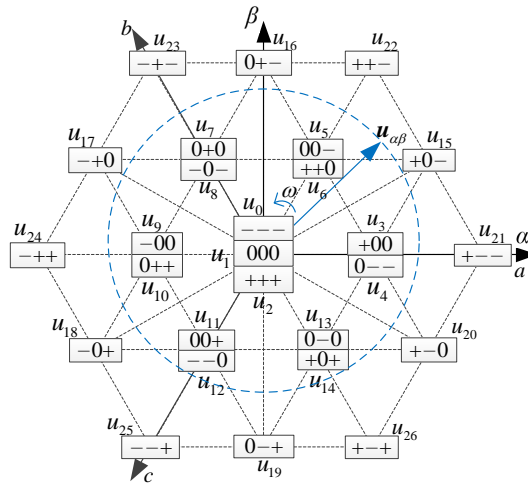
Figure 5.2: Definition of 27 switching states and corresponding voltage vectors.

Since the vector $\vec{\boldsymbol{\xi}}_{abc} = [\xi_a, \xi_b, \xi_c]^{\mathrm{T}}$ in abc-reference frame can be transformed to $\vec{\boldsymbol{\xi}}_{\alpha\beta} = [\xi_\alpha, \xi_\beta]^{\mathrm{T}}$ in two-phase stationary $\alpha\beta$-reference frame by $\vec{\boldsymbol{\xi}}_{\alpha\beta} = \boldsymbol{M}_{abc-\alpha\beta}\vec{\boldsymbol{\xi}}_{abc}$. The voltage expression in (5.4) can be transformed into (for great details, see [106])

$$\vec{\boldsymbol{e}}_{\alpha\beta}(t) = R_g\vec{\boldsymbol{i}}_{\alpha\beta}(t) + L_g\frac{d\vec{\boldsymbol{i}}_{\alpha\beta}}{dt} + \vec{\boldsymbol{u}}_{\alpha\beta}(t) \tag{5.6}$$

where $\vec{\boldsymbol{e}}_{\alpha\beta}$, $\vec{\boldsymbol{i}}_{\alpha\beta}$, and $\vec{\boldsymbol{u}}_{\alpha\beta}$ represent the voltage, current, and rectifier voltage of the grid side in the two-phase stationary $\alpha\beta$-reference frame. The rectifier voltage can be given by

$$\vec{\boldsymbol{u}}_{\alpha\beta} = \boldsymbol{M}_{abc-\alpha\beta} \times (v_{c1}\frac{|\vec{\boldsymbol{s}}_n| + \vec{\boldsymbol{s}}_n}{2} - v_{c2}\frac{|\vec{\boldsymbol{s}}_n| - \vec{\boldsymbol{s}}_n}{2}) \tag{5.7}$$

where $|\vec{\boldsymbol{s}}_n| = [|s_a|, |s_b|, |s_c|]^{\mathrm{T}}$. Suppose two capacitors are balanced, the voltage vectors that corresponds to those 27 switching states are shown in Fig. 5.2.

The angular velocity of the SRM is governed by the following first-order differential equation

$$\frac{d\omega_r(t)}{dt} = \frac{1}{J_m}(\tau_{e,m}(t) - \tau_l(t)) \tag{5.8}$$

where J_m, $\tau_{e,m}$, and τ_l represent motor inertia, electromagnetic torque, and load torque, respectively. (5.8) can also be transformed into the following form by multiplying ω_r on both sides of it

$$\frac{1}{2}J_m\frac{d\omega_r^2(t)}{dt} = p_{m,em}(t) - p_{m,l}(t) \tag{5.9}$$

where $p_{m,em}$ and $p_{m,l}$ represent the electromagnetic power and load power of SRM, respectively.

5.2.2 Voltage balance of capacitors

The current equation on DC link can be written as

$$\begin{cases} i_p = s_{ap}i_a + s_{bp}i_b + s_{cp}i_c \\ i_n = s_{an}i_a + s_{bn}i_b + s_{cn}i_c \\ i_o = s_{ao}i_a + s_{bo}i_b + s_{co}i_c \end{cases} . \tag{5.10}$$

Applying Kirchhoff's current law to midpoint on DC link gets

$$i_o + C_1\frac{dv_{c1}}{dt} - C_2\frac{dv_{c2}}{dt} = 0 \tag{5.11}$$

where $C_1 = C_2 = C$. Bringing (5.10) into (5.11) gets

$$s_{ao}i_a + s_{bo}i_b + s_{co}i_c + C\frac{dv_{c1}}{dt} - C\frac{dv_{c2}}{dt} = 0. \tag{5.12}$$

Since $s_{io} = 1 - s_{ip} - s_{in}$, the expression above can be transformed to

$$(-s_{ap} - s_{an})i_a + (-s_{bp} - s_{bn})i_b + (-s_{cp} - s_{cn})i_c + C\frac{dv_{c1}}{dt} - C\frac{dv_{c2}}{dt} = 0. \tag{5.13}$$

Then, the variation ratio of the deviation of neutral point voltage Δv, namely, the difference between v_{c1} and v_{c2}, can be obtained as

$$\frac{d\Delta v(t)}{dt} = \frac{1}{C}|\vec{s}_n(t)|^{\mathrm{T}} \cdot \vec{i}_{abc}(t) \tag{5.14}$$

where $|\vec{s}_n|^{\mathrm{T}} = [|s_a|, |s_b|, |s_c|]$.

5.2.3 Discrete models

As has been deduced in Chapter. 4, the differentiations of real and reactive power can be calculated by

$$\frac{d}{dt}\begin{pmatrix} p(t) \\ q(t) \end{pmatrix} = \frac{3}{2L_g}\begin{bmatrix} e_\alpha(t) & e_\beta(t) \\ e_\beta(t) & -e_\alpha(t) \end{bmatrix}\begin{pmatrix} e_\alpha(t) - u_\alpha(t) \\ e_\beta(t) - u_\beta(t) \end{pmatrix} + \begin{pmatrix} -\frac{R_g}{L_g}p(t) - \omega_g q(t) \\ -\frac{R_g}{L_g}q(t) + \omega_g p(t) \end{pmatrix}. \tag{5.15}$$

Applied with the Forward Euler discretization, (5.15) can be transformed into

$$
\begin{pmatrix} p[k+1] \\ q[k+1] \end{pmatrix} = \frac{3T_s}{2L_g} \begin{bmatrix} e_\alpha[k] & e_\beta[k] \\ e_\beta[k] & -e_\alpha[k] \end{bmatrix} \begin{pmatrix} e_\alpha[k] - u_\alpha[k] \\ e_\beta[k] - u_\beta[k] \end{pmatrix} \\
+ \begin{pmatrix} p[k] - \frac{T_s R_g}{L_g} p[k] - T_s \omega_g q[k] \\ q[k] - \frac{T_s R_g}{L_g} q[k] + T_s \omega_g p[k] \end{pmatrix}
\tag{5.16}
$$

where $\xi[k]$, $\xi[k+1]$, and T_s denote variable value at instant k and $k+1$, and control period, respectively.

Similarly, the discrete form of the variation of upper and lower DC-link capacitor voltages can be written as follows

$$
\Delta v[k+1] = \frac{T_s}{C} |\vec{s}_n[k]|^{\mathrm{T}} \cdot \vec{i}_{abc}[k] + \Delta v[k].
\tag{5.17}
$$

Since $\vec{u}_{\alpha\beta}$ of every switching states $\vec{s}_n$ can be obtained according to (5.7), the corresponding $p_n[k+1]$, $q_n[k+1]$ and $\Delta v_n[k+1]$ of every switching state can be predicted based on (5.16) and (5.17).

Based on (5.9), the discrete expression of SRM angular velocity can be written as

$$
\omega_r^2[k+1] = \frac{2T_s}{J_m} (p_{m,em}[k] - p_{m,l}[k]) + \omega_r^2[k].
\tag{5.18}
$$

5.3   MP-DPC principle and time delay compensation

The generalized form of the cost function of MPC is

$$
J = \|Y^*[k+1] - y[k+1]\|^2 + \zeta_x[k+1]
\tag{5.19}
$$

$$
\vec{s}^{opti}[k] = \arg \min_{\vec{s}^{opti} \in \vec{s}_n} J(\vec{s}_n[k])
\tag{5.20}
$$

where $\vec{s}_n[k]$ represents the possible converter switching state of instant k, $\vec{s}^{opti}[k]$ represents the optimal switching state of instant k, and Y^* represents the references of the concerned variables. $y(k+1) = f(\vec{s}_n[k])$ is predicted based on the possible converter switching state $\vec{s}_n[k]$ and the measured variables of instant k. The suppression factor ζ_x is introduced into the cost function to limit the concerned system variables within a safe range for constraint, and it is generally given by

$$
\zeta_x[k+1] = \begin{cases} 0, & \text{if } \|h_x(\vec{s}_n[k])\| \le \|h_x^{\max}\| \\ \infty, & \text{if } \|h_x(\vec{s}_n[k])\| > \|h_x^{\max}\| \end{cases}
\tag{5.21}
$$

where h_x denotes the mathematical expression of the concerned variables and $h_x^{\max}$ denotes the maximum of the concerned system variables. Based on the above, the active and reactive power inside the system can be limited by the ζ_{pq} below

$$
\zeta_{pq}[k+1] = \begin{cases} 0, & \text{if } \|p[k+1]\| \le \|p^{\max}\| \\ \infty, & \text{if } \|p[k+1]\| > \|p^{\max}\| \end{cases} + \begin{cases} 0, & \text{if } \|q[k+1]\| \le \|q^{\max}\| \\ \infty, & \text{if } \|q[k+1]\| > \|q^{\max}\| \end{cases}
\tag{5.22}
$$

Ideally, the optimal switching state $s_x^{opti}[k]$ should be computed within an infinitesimally short time in the interval of $[k, k+1]$, and it should be applied during the entire time interval of $[k, k+1]$. However, in a practical system, there is a time delay in digital implementation [107] caused by measurement delay, computation delay, actuation delay, etc., which makes $\vec{s}^{opti}[k]$ cannot be applied to power switches at instant k in time. To address this problem, time delay compensation is considered into MPC so that the optimal switching state $\vec{s}^{opti}[k]$ for $[k, k+1]$ can be calculated during $[k-1, k]$ and applied at instant k. The core of time delay compensation is to predict one more step in every control period, and correspondingly, the cost function with time delay compensation is modified into

$$J = \|Y^*[k+2] - y[k+2]\|_Q^2 + \zeta_x[k+2] \tag{5.23}$$

$$\vec{s}^{opti}[k+1] = \arg\min_{\vec{s}^{opti} \in \vec{s}_n} J\left(\vec{s}_n[k+1]\right) \tag{5.24}$$

where $y[k+2] = f\left(\vec{s}_n[k+1]\right)$ is predicted based on the possible switching state $\vec{s}_n[k+1]$ of instant $k+1$. The algorithm implementation process during $[k, k+1]$ for MPC with time delay compensation is as follows. At instant k, the optimal switching state $\vec{s}^{opti}[k]$ selected during $[k-1, k]$ should be implemented. Then the effect of $\vec{s}^{opti}[k]$ on the concerned variables at instant $k+1$ (i.e., $y[k+1]$) should be estimated based on the discrete model of instant $k+1$. Afterward, the effect of every $\vec{s}_n[k+1]$ on the concerned variables at instant $k+2$ (i.e., $y[k+2]$) can be predicted according to the discrete model of instant $k+2$. Finally, the optimal switching state $\vec{s}^{opti}[k+1]$ for instant $k+1$ can be determined by evaluating the cost function in (5.23), and it will be stored to be applied to power converters at the next sampling instant, i.e., instant $k+1$. It can be found that with the time delay compensation, the optimal switching state of each instant is calculated in the previous time interval and can be applied to converters at the exactly right instant, which improves the control accuracy.

5.4 Proposed cascade-free MP-DPC strategy

5.4.1 New cost function

Considering its unique advantages of controlling several control targets and constraints simultaneously via a single cost function, MPC is adopted to control the high-speed SRM drive system. Furthermore, a cascade-free MP-DPC control strategy that directly regulates the motor speed, power flows, and capacitor voltage balance within a newly-defined cost function is proposed. Instead of using the cascade control structure of conventional PI-MPC strategy, the proposed control strategy directly selects the optimal voltage vector by evaluating the cost function below

$$J_c = \underbrace{\|(\omega_r^* - \omega_r[k+2]) - \kappa\left(p[k+2] - p_{m,l}\right)\|^2}_{J_\omega} + \underbrace{\|\omega_r^* - \omega_r[k+2]\|^2}_{J_{lit\omega}}$$
$$+ \lambda_q \underbrace{\|Q^* - q[k+2]\|^2}_{J_q} + \lambda_c \underbrace{\left(\Delta v\,[k+2]\right)^2}_{J_{\Delta v}} + \zeta_{pq}[k+2] \tag{5.25}$$

where ω_r^* is the speed setpoint, $\kappa \in R_+$ is the coefficient for speed regulation, λ_q is the weighting factor for reactive power regulation, λ_c is the weighting factor for capacitor balancing control.

The angular velocity ω_r of instant $k + 2$ in the above expression is predicted according to

$$\omega_r[k + 2] = \sqrt{\frac{2T_s}{J_m}\left(p[k + 1] - p_{m,l}\right) + \omega_r^2[k + 1]} \qquad (5.26)$$

where the electromagnetic power $p_{m,em}$ in (5.18) is replaced by the grid-side input power p by assuming a loss-less power transfer from grid side to motor side. The estimated SRM output power $p_{m,l}$ in (5.25) and (5.26) equals $\tau_l\omega_r$, and τ_l is generally obtained by a load torque observer (See Appendix D). However, a fan is employed as the load in this high-speed SRM drive system. The load torque is proportional to the square of the speed for the fan-loaded system [108], and the coefficient can be easily obtained from experiment. Thus the load power can be simply calculated by

$$p_{m,l} = \delta\omega_r^3 \qquad (5.27)$$

where the coefficient δ depends on the structure of the fan.

MPC can regulate the terms in its cost function to approach zero to realize the tracking of setpoints, so suppose J_ω and $J_{lit\omega}$ equal zero in the following explanation. In (5.25), $J_{lit\omega}$ is conducive to choosing the vector that will generate an angular velocity closer to its setpoint at instant $k + 2$. If $\omega_r^* > \omega_r[k + 2]$ in $J_{lit\omega}$, the vector that will produce an active power larger than load power of SRM at instant $k + 2$ (i.e., $p[k + 2] > p_{m,l}$) will be selected in J_ω. It means the grid not only will supply the power to afford the load, but will supply additional power for motor acceleration, thereby increasing the angular velocity. If $\omega_r^* < \omega_r[k+2]$ in $J_{lit\omega}$, the vector that will produce a $p[k + 2]$ smaller than $p_{m,l}$ tend to be selected in J_ω. In this case, insufficient power is provided from grid to SRM load, thus reducing the angular velocity. When $\omega_r[k + 2]$ reaches ω_r^* in steady state, the power provided by grid exactly matches the power consumed by load, i.e., $p[k + 2] = p_{m,l}$, and the angular velocity will stay at the setpoint.

In SRM drive system, the power expression below holds

$$p = p_{m,em} + p_{m,cu} + \underbrace{p_{a,co} + p_{a,sw} + p_{m,co} + p_{m,sw}}_{\Sigma p_{con,loss}} + \ldots \qquad (5.28)$$

where copper loss $p_{m,cu}$ denotes the power consumed on resistor, and $\Sigma p_{con,loss}$ represents the conduction loss and switching loss of VSR and SRM converter. Therefore, when $\omega_r[k + 2]$ reaches ω_r^* in J_ω in steady state, it is the electromagnetic power $p_{m,em}$, not the grid-side input power p, that should be equal to $p_{m,l}$ to keep ω_r stay at its setpoint according to (5.9). Because of the power difference between p and $p_{m,em}$ in (5.28), less power can be actually obtained as $p_{m,em}$ when the grid-side input power p is assigned a value that should be assigned to $p_{m,em}$, which makes the regulated angular velocity lower than its setpoint. To eliminate the steady-state velocity error in the aforementioned two cases, the sum term $\sum_{k=1}^{\infty}(\omega_r^* - \omega_r[k + 2])$ is added into $p_{m,l}$ for compensation. Consequently, the velocity of SRM can be strictly controlled while achieving additional control requirements such as capacitor voltage balance and reactive power regulation.

The proposed control system based on cascade-free MP-DPC control strategy is presented in Fig. 5.3. The one-step delay in digital implementation [109] means the optimal switching state $\vec{s}^{opti}[k]$ selected in the interval of $[k, k + 1]$ can not be applied to the VSR until instant $k + 1$. Therefore, time delay compensation is added to the proposed cost function to enhance the control accuracy so that the optimal switching state $\vec{s}^{opti}[k]$ that should be applied at instant k can

be calculated in the interval of $[k-1, k]$. The implementation process of proposed control strategy with time delay compensation is shown in Fig. 5.4. At instant k, $\vec{s}^{opti}[k]$, which is selected in the interval of $[k-1, k]$, should be applied to the VSR, and its corresponding rectifier voltage $\vec{u}_{\alpha\beta}^{opti}[k]$ can be obtained based on (5.7). Then $p^{opti}[k+1]$, $q^{opti}[k+1]$, and $\Delta v^{opti}[k+1]$ can be estimated according to (5.16) and (5.17). $\omega_r[k+1]$ can be predicted through shifting backward by one control period (T_s) on (5.26). Afterward, $p_n[k+2]$, $q_n[k+2]$, and $\Delta v_n[k+2]$ of every switching state can be predicted through shifting forward by one control period on (5.16) and (5.17), and $\omega_r[k+2]$ is predicted according to (5.26). Finally, the optimal switching state $\vec{s}^{opti}[k+1]$ can be selected by evaluating (5.25), and it should be stored to be implemented at instant $k+1$.
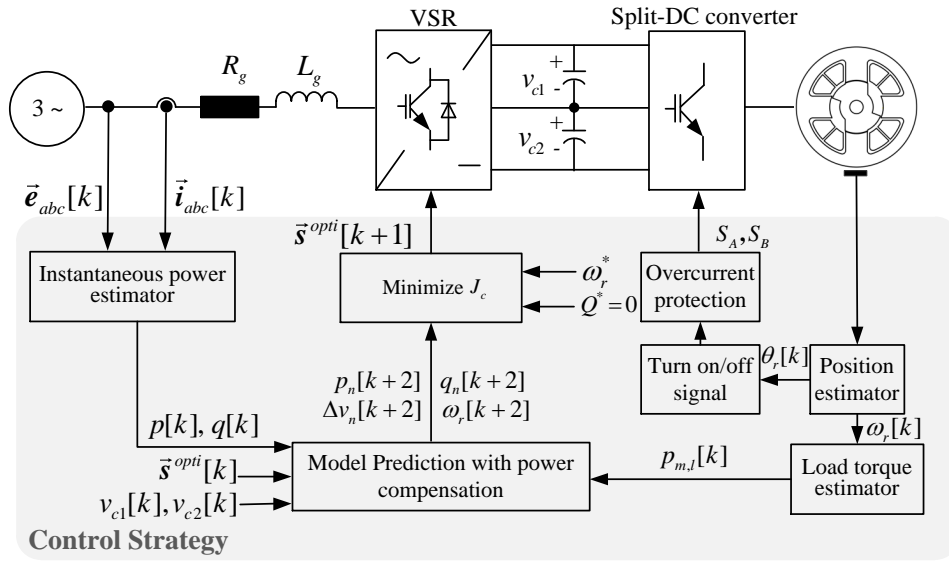
Figure 5.3: Proposed control system based on cascade-free MP-DPC strategy.
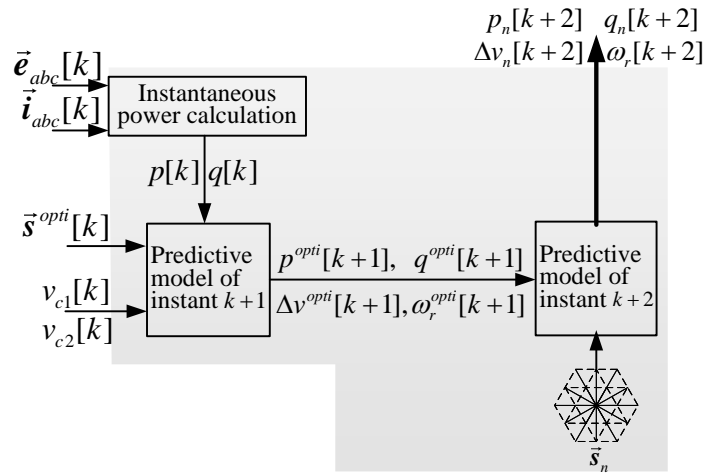
Figure 5.4: Model prediction with time delay compensation.

5.4.2 Power compensation

(5.16) holds only when the actual values of the inductor and resistor, i.e., L_g and R_g, are brought into it for prediction. However, it is actually the nominal values, i.e., $L_{g,no}$ and $R_{g,no}$, that are involved in the prediction since L_g and R_g are unknown, and it is also possible that the actual values L_g and R_g change during the operation, which causes the steady-state power error in system [90]. To address this problem, Kalman filter is added to the proposed strategy to compensate for the steady-state error by estimating the disturbances in power expression, and the aforementioned uncertainties can be regarded as the active power disturbances f_p and reactive power disturbances f_q for (5.16). Then the state space model of Kalman filter can be written as

$$\underbrace{\begin{pmatrix} p[k] \\ q[k] \\ f_p[k] \\ f_q[k] \end{pmatrix}}_{\boldsymbol{X_d}[k]} = \underbrace{\begin{bmatrix} \boldsymbol{C}_d & \boldsymbol{D}_d \\ \boldsymbol{0}_{2\times2} & \boldsymbol{I}_2 \end{bmatrix}}_{\boldsymbol{F}_d} \underbrace{\begin{pmatrix} p[k-1] \\ q[k-1] \\ f_p[k-1] \\ f_q[k-1] \end{pmatrix}}_{\boldsymbol{X_d}[k-1]} + \underbrace{\frac{T_s}{L_{g,no}} \begin{bmatrix} \boldsymbol{A}_c[k-1] \\ \boldsymbol{0}_{2\times2} \end{bmatrix}}_{\boldsymbol{G}_d[k-1]} \boldsymbol{B}_c[k-1] + \boldsymbol{W}_d[k]$$

$$\text{(5.29)}$$

$$\underbrace{\begin{pmatrix} p[k] \\ q[k] \end{pmatrix}}_{\boldsymbol{z}_d[k]} = \underbrace{\begin{bmatrix} \boldsymbol{I}_2 & \boldsymbol{0}_{2\times2} \end{bmatrix}}_{\boldsymbol{H}_d} \boldsymbol{X_d}[k] + \boldsymbol{V}_d[k] \tag{5.30}$$

where $\boldsymbol{A}_c[k-1] = \frac{3}{2} \times \begin{bmatrix} e_\alpha[k-1] & e_\beta[k-1] \\ e_\beta[k-1] & -e_\alpha[k-1] \end{bmatrix}$, $\boldsymbol{B}_c[k-1] = \begin{pmatrix} e_\alpha[k-1] - u_\alpha[k-1] \\ e_\beta[k-1] - u_\beta[k-1] \end{pmatrix}$, $\boldsymbol{C}_d = \begin{bmatrix} 1 - \frac{T_s R_{g,no}}{L_{g,no}} & -T_s\omega_g \\ \omega_g T_s & 1 - \frac{T_s R_{g,no}}{L_{g,no}} \end{bmatrix}$, $\boldsymbol{D}_d = \begin{bmatrix} \frac{-T_s}{L_{g,no}} & 0 \\ 0 & \frac{-T_s}{L_{g,no}} \end{bmatrix}$, $\boldsymbol{W}_d[k]$ is the process noise with the covariance matrix $\boldsymbol{Q}_d$: $\boldsymbol{W}_d[k] \sim N(0, \boldsymbol{Q}_d)$, and $\boldsymbol{V}_d[k]$ is measurement noise with the covariance matrix $\boldsymbol{R}_d$: $\boldsymbol{V}_d[k] \sim N(0, \boldsymbol{R}_d)$. Then the predicted (a priori) estimate of state vector can be obtained as below based on the mathematical model

$$\hat{\boldsymbol{X}}_d^-[k] = \boldsymbol{F}_d\hat{\boldsymbol{X}}_d[k-1] + \boldsymbol{G}_d[k-1]\boldsymbol{B}_c[k-1] \tag{5.31}$$

where $\hat{\boldsymbol{X}}_d^-[k]$ represents the priori estimate of state vector $\boldsymbol{X}_d$, and $\hat{\boldsymbol{X}}_d[k-1]$ represents the posteriori estimate of state vector calculated within interval $[k-1,k)$. The accuracy covariance of the priori estimate of state vector is defined, i.e., $\boldsymbol{P}_d^-[k] = E[(\boldsymbol{X}_d[k] - \hat{\boldsymbol{X}}_d^-[k])(\boldsymbol{X}_d[k] - \hat{\boldsymbol{X}}_d^-[k])^T]$ and it can be calculated by

$$\boldsymbol{P}_d^-[k] = \boldsymbol{F}_d\boldsymbol{P}_d[k-1]\boldsymbol{F}_d^T + \boldsymbol{Q}_d \tag{5.32}$$

where $\boldsymbol{P}_d[k-1]$ is the accuracy covariance of the posteriori estimate of state vector obtained in $[k-1,k)$. Then in the correction stage, Kalman gain $\boldsymbol{K}_d[k]$ and the posteriori estimate of state vector $\hat{\boldsymbol{X}}_d[k]$ can be calculated by

$$\boldsymbol{K}_d[k] = \frac{\boldsymbol{P}_d^-[k]\boldsymbol{H}_d^T}{\boldsymbol{H}_d\boldsymbol{P}_d^-[k]\boldsymbol{H}_d^T + \boldsymbol{R}_d} \tag{5.33}$$

$$\hat{\boldsymbol{X}}_d[k] = \hat{\boldsymbol{X}}_d^-[k] + \boldsymbol{K}_d[k](\boldsymbol{Z}_d[k] - \boldsymbol{H}_d\hat{\boldsymbol{X}}_d^-[k]) \tag{5.34}$$

$$\boldsymbol{P}_d[k] = (\boldsymbol{I} - \boldsymbol{K}_d[k]\boldsymbol{H}_d)\boldsymbol{P}_d^-[k] \tag{5.35}$$

where $\boldsymbol{P}_d[k]$ is updated to be used in the next sampling period. Through this process, $f_p[k]$ and $f_q[k]$ are estimated and used to correct the expressions for power prediction.

5.5 Experimental evaluation

5.5.1 Experimental parameters and pseudocode

In order to verify the feasibility of the proposed high-speed SRM drive system, an idea-proofed testbench is constructed. The hardware configuration and experimental paramters of the testbench are shown in Table 5.1 and Table 5.2, respectively.

To clarify and to ease the implementation of the proposed control strategy, the necessary steps for the computation/estimation are listed as quasi-code as follows:

1: **function** Proposed control strategy ($\vec{e}_{abc}[k]$, $\vec{i}_{abc}[k]$, $v_{c1}[k]$, $v_{c2}[k]$, $\theta_r[k]$, $\vec{s}_n^{opti}[k]$, k)

2:      Apply $\vec{s}_n^{opti}[k]$
3:      **if** $\theta_{m,on} \le \theta_r[k] \le \theta_{m,off}, m \in \{A, B\}$ **then**
4:      Set $S_m = 1$
5:      **else**
6:      Set $S_m = 0$
7:      **end if**
8:      Compute $\omega_r[k]$
9:      Compute $p_{m,l}[k]$
10:     Compute $p[k]$, $q[k]$, and $\Delta v[k]$
11:     Estimate $f_p[k]$ and $f_q[k]$
12:     Estimate $p^{opti}[k+1]$, $q^{opti}[k+1]$, $\Delta v^{opti}[k+1]$ and $\omega_r^{opti}[k+1]$ with $\vec{s}_n^{opti}[k]$
13:     **for** n = 1 to 27
14:     Predict $p_n[k+2]$, $q_n[k+2]$, $\Delta v_n[k+2]$, and $\omega_r[k+2]$ with $\vec{s}_n$
15:     Evaluate the cost function in (5.25)
16:     **end for**

17:     Store $\vec{s}_n^{opti}[k+1]$
18:     **end function**

5.5.2 Experimental results

5.5.2.1 Steady-state performances

Fig. 5.5, Fig. 5.6, and Fig. 5.7 present the obtained test results when the SRM operates at 15000 r/min, 20000 r/min, and 25000 r/min, respectively. In Fig. 5.5, the grid-side current shows

Table 5.1: Hardware configuration of the high-speed SRM drive system based on cascade-free MP-DPC

Function	Producer	Type
DSP	TEXAS INSTRUMENTS	TMS320F28335
Muti-level converter	INFINEON	F3L75R12W1H3
IGBT	IXYS	IXGH60N60
Fast recovery diodes	IXYS	DSEI60-06A
High-speed incremental encoder	HEIDENHAIN	ERO1420

Table 5.2: Experimental parameters of the high-speed SRM drive system based on cascade-free MP-DPC

Description	Parameter	Value
Frequency of AC-side voltage	ω_r	100π
AC-side line voltage	$e_{gl}(\,\mathrm{V})$	58
AC-side filter resistance	$R_g(\Omega)$	0.03
AC-side filter inductance	$L_g(\mathrm{mH})$	12
DC-link capacitors	$C_1, C_2(\mu\mathrm{F})$	1360
Control period	$T_s(\mu\mathrm{s})$	50
Rated torque of the high-speed SRM	$T_{\mathrm{em}}(\mathrm{N}\cdot\mathrm{m})$	0.12
Rated speed of the high-speed SRM	$n_r(\mathrm{r/min})$	25000

an undistorted sinusoidal waveform, and its phase varies together with the phase of grid-side voltage. The voltage curves of the upper and lower capacitors on DC link coincide with each other. A digital-to-analog converter with two channels is used to illustrate real and reactive power. The short lines on the left of the curve of active power and curve of reactive power indicate 0 W and 0 Var, respectively. In Fig. 5.6, the active power is regulated to 180 W to run the motor at 20000 r/min while the reactive power of the system can be maintained within $\pm$ 10 Var for grid-side power quality improvement. In Fig. 5.7, v_{c1} and v_{c2} are still well balanced when the motor operates at 25000 r/min. Considering the increased mechanical output, the active power has been adjusted to approximately 360 W to supply the motor with sufficient energy, and accordingly, the DC-link voltage is increased to roughly 270 V. The reactive power has been regulated within $\pm$ 20 Var, and the sine-shaped grid-side current is obtained, although the pulsating current flows on DC-bus.

5.5.2.2 Transient-state performances

Fig. 5.8 shows system test results when the SRM starts from standstill to rated speed. The motor has been successfully started up to 25000 r/min under the proposed cascade-free control strat-
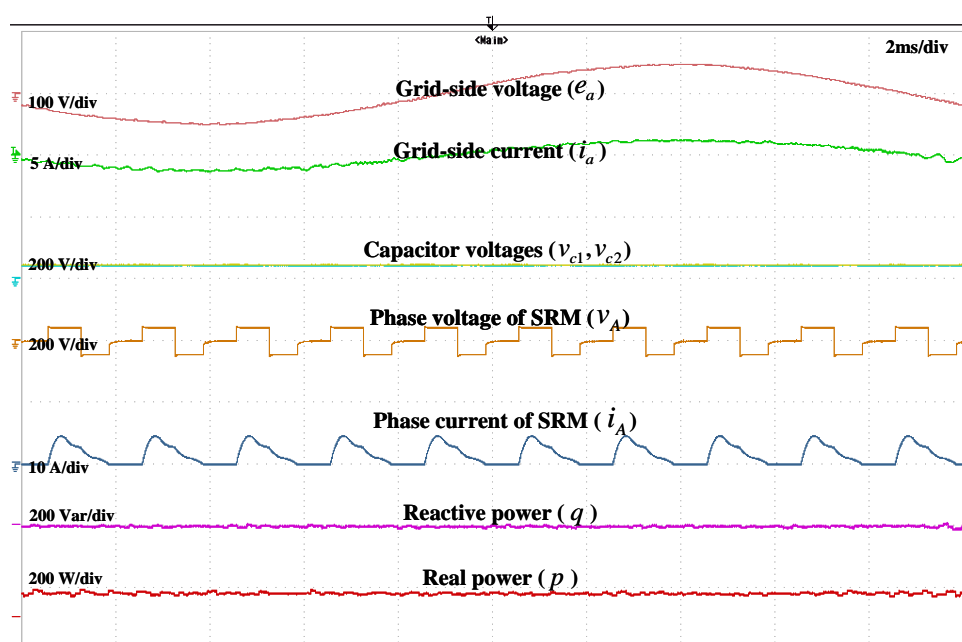
Figure 5.5: System test results when SRM runs at 15000 r/min.
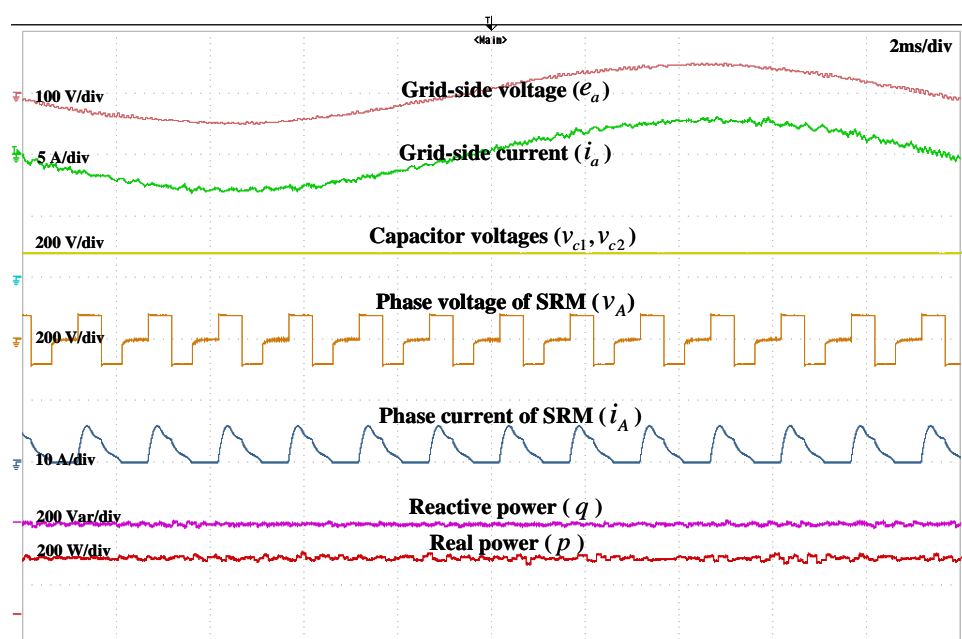
Figure 5.6: Dynamic test results when SRM runs at 20000 r/min.

egy. Due to the increased rotational speed, the voltages of the upper and lower capacitors are not balanced at first. However, through the regulation of capacitor voltage in the cost function of MP-DPC, the voltage difference between the two capacitors has been continuously narrowed. By choosing an optimal switching state for the VSR, the capacitor voltages restore to the state of equilibrium after about four electrical periods. The phase of grid-side current is identical with that of the grid-side voltage from the beginning. The phase current of SRM reaches the
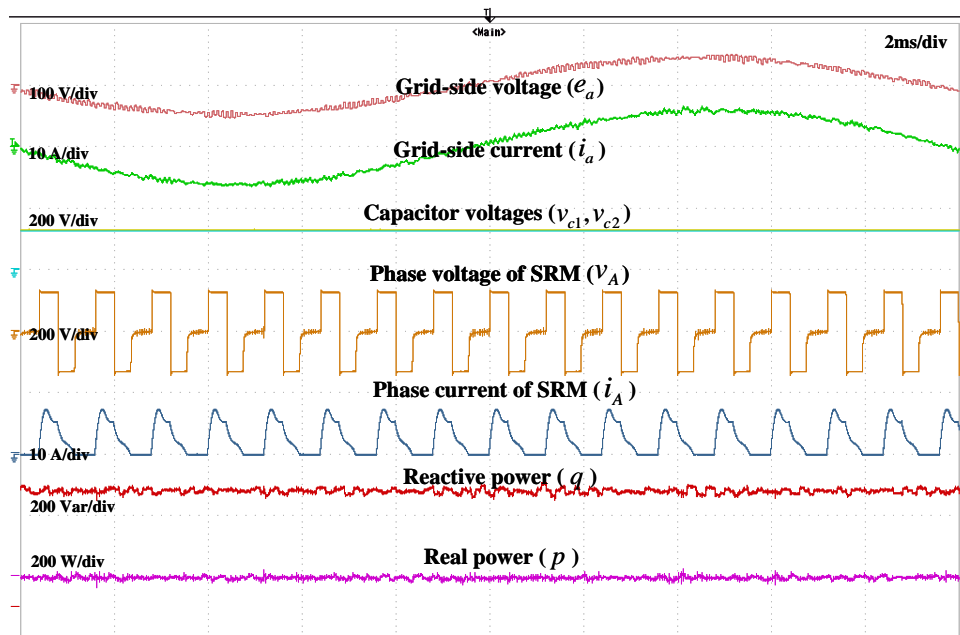
Figure 5.7: System test results when SRM runs at 25000 r/min.
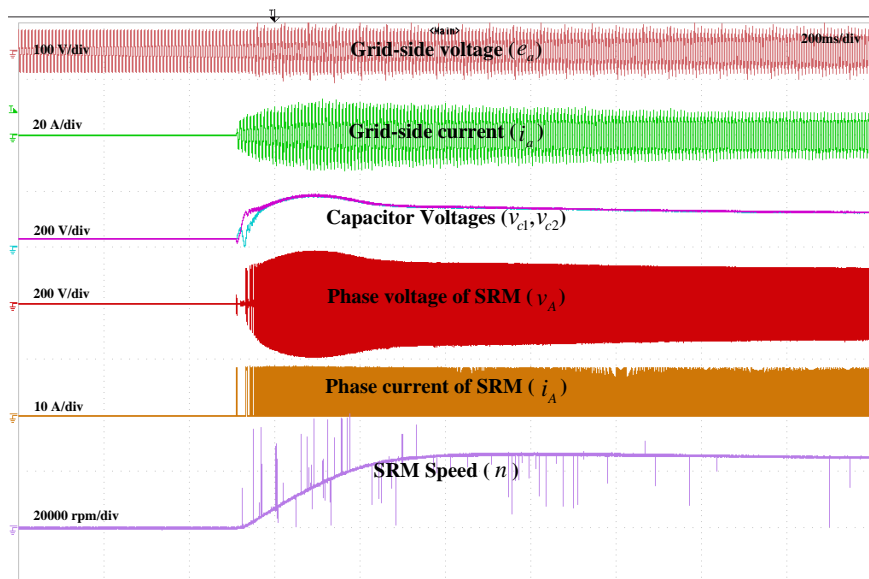
Figure 5.8: Dynamic test results when the SRM starts from standstill to 25000 r/min.

preset maximum current in the first several electrical periods of starting, so hardware current
chopping [110] is implemented to prevent the current from being over the limit. The sudden
increases appearing on the speed curve of DAC output are just noises since none of other curves
shows corresponding alterations.

Fig. 5.9 and Fig. 5.10 present the acceleration and deacceleration curves of the proposed
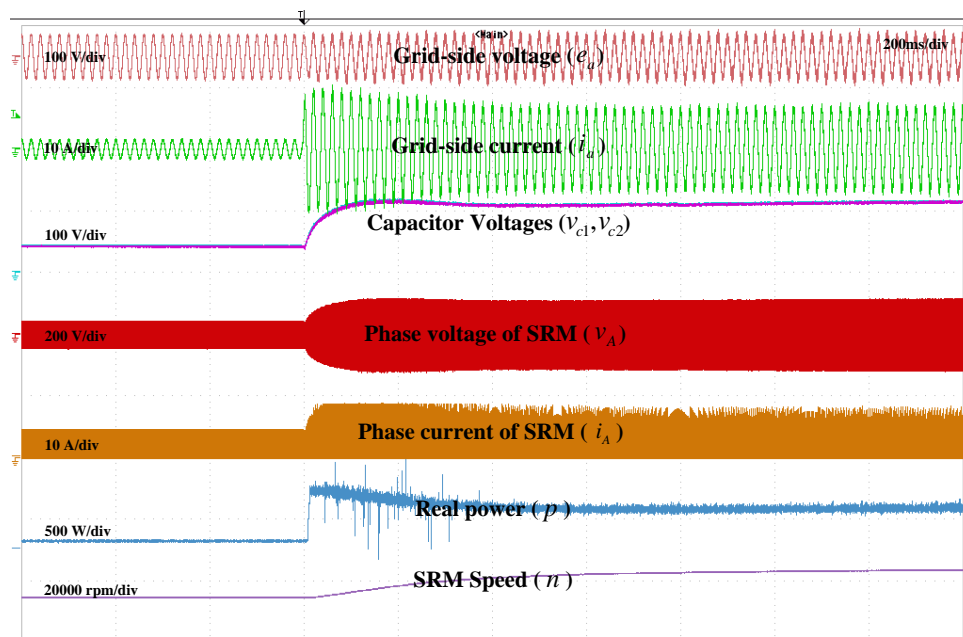
Figure 5.9: Dynamic test results when speed increases from 15000 r/min to 25000 r/min.
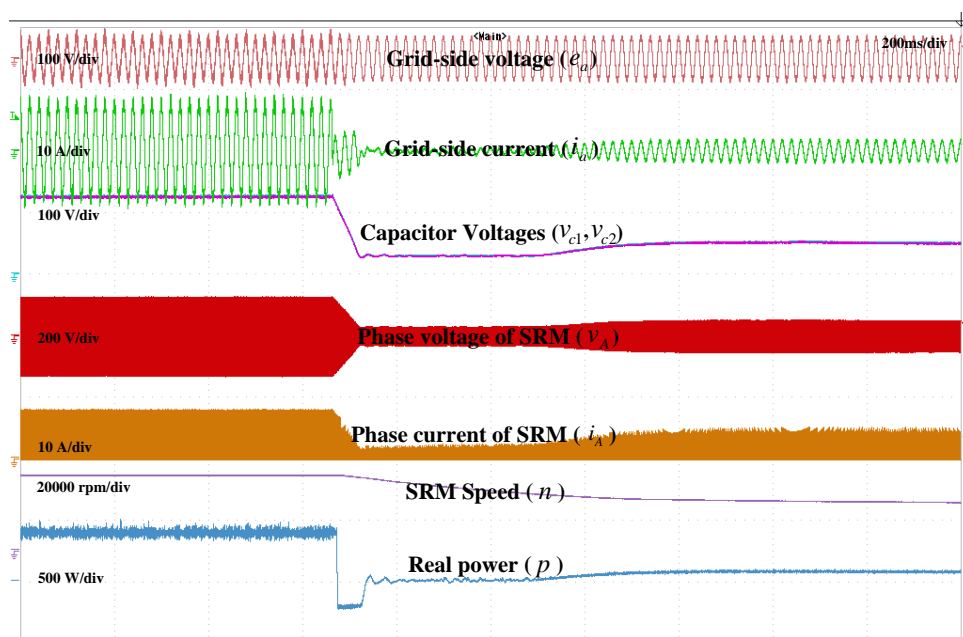
Figure 5.10: Dynamic test results when speed decreases from 25000 r/min to 15000 pm.

drive system, respectively. In Fig. 5.9, when the speed rises from 15000 r/min to 25000 r/min, active power increases to supply enough power for the SRM, and as a result, the DC-link voltage is increased due to the continuous injection of active power. Balanced capacitor voltages and sinusoidal grid-side current being in phase with voltage can be obtained throughout these dynamic regulations. When the speed command is reduced from 25000 r/min to 15000 r/min in Fig. 5.10, the direction of grid-side current is instantly reversed under power control to make

the active power flow back to grid. In consequence, the motor speed is rapidly reduced by transferring the excess energy back to the grid. Still, the reactive power can be well controlled to around zero.
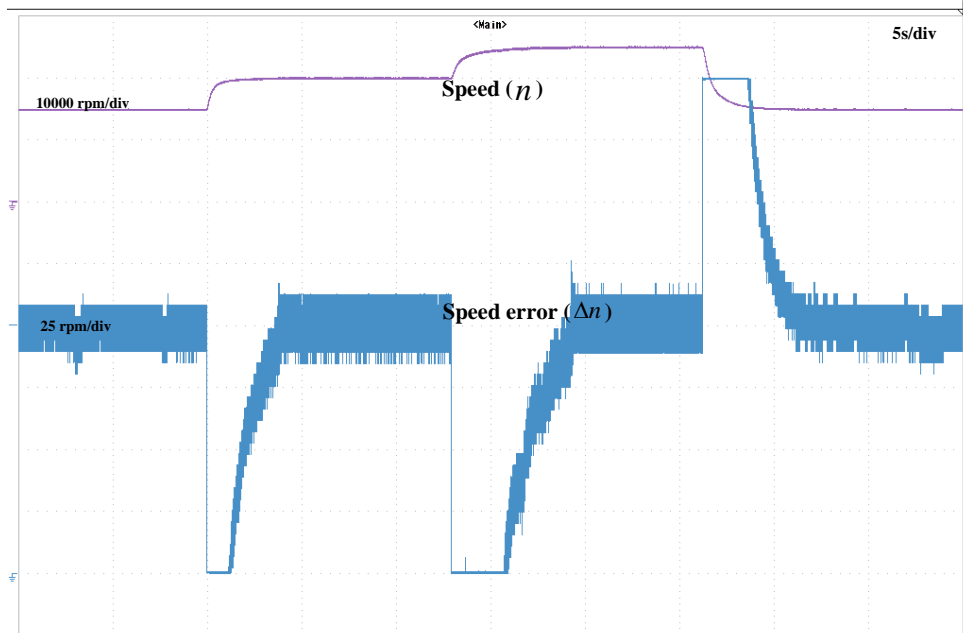
Figure 5.11: Speed and speed error.

The speed and speed error curves in the dynamic regulation (speed changes from 0 r/min to 20000 r/min to 25000 r/min to 15000 r/min) are shown in Fig. 5.11. Because of the upper-lower limit of DAC output and the conversion ratio in the program, the maximal and minimal speed that can be displayed are $\pm$ 100 r/min. The speed can be well regulated since the steady-state speed errors are governed within $\pm$ 15 r/min in the proposed system.

5.5.2.3 THDs and power factors

The grid-side current THDs and power factors are collected in Fig. 5.12. As can be seen from the curves, the proposed system can control the grid-side current THDs to around 2.8% and the power factor to around 0.995 at the rated operating condition.

5.6 Summary

In this chapter, a cascade-free MP-DPC strategy is proposed for the three-level VSR-fed high-speed SRM system. In the proposed strategy, the angular velocity regulation term, power regulation terms, and capacitor voltage balancing term are merged into a newly-defined cost function, thereby eliminating the conventional cascade control structure. The strategy selects the voltage vector that not only will generate an angular velocity closer to the setpoint at instant $k + 2$, but will generate an active power that can further reduce that velocity error for the future instant. Considering the inaccurate nominal values and the changed real values of inductors and
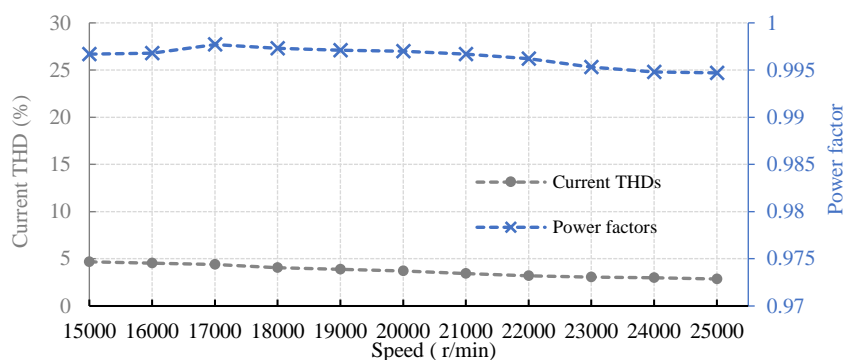
Figure 5.12: Grid-side power factors and current THDs.

resistors, Kalman filter is adopted to estimate the power disturbances caused by the mismatched parameters, thus eliminating the steady-state error by correcting the power expressions. In the experimental validation, stable speed is obtained, and the speed error can be maintained within $\pm$ 15 r/min at 25000 r/min. At the same time, the upper and lower capacitors on DC link have been well balanced. Besides, grid-side power quality is controlled by regulating the active power to be constant and reducing the reactive power to near zero. Near-unity grid-side power factor and sine-shaped grid-side current with the THDs less than 5% are obtained in the experiments.

CHAPTER 6

Conclusion

This dissertation focuses on the control of grid-connected high-speed SRM drive system, and satisfying current THDs, controllable reactive power, and well-regulated SRM are the main control goals. Conventionally, DBR is adopted to drive the SRM converter. As has been presented in Chapter 2, although the adoption of DBR reduces system cost, a large amount of reactive power and current harmonics, which have severe damage to power quality, will be induced into the grid, and the reactive power can be even comparable to active power. Additionally, in the existing SRM drive systems with improved grid-side power quality, the front-end converter and back-end SRM drive are separate control units with their respective control schemes.

In chapter 3, a drive topology composed of a T-type single-phase three-level VSR and a 4-level SRM converter is proposed to drive the high-speed SRM while improving the power quality. Compared with the conventional split-DC converter, the 4-level SRM converter of the proposed drive topology adopts one more switch and one more diode for each phase, but two more conduction modes are formed. With the double-voltage demagnetization mode of the 4-level SRM converter, the tailing time of demagnetization current is significantly reduced, which increases the utilization of inductance increasing region. All the conduction modes of this converter can be implemented successfully, even in the multi-phase excitation region. Besides, a current control scheme based on virtual orthogonal system is proposed, which regulates the SRM and power factor by the d-axis and q-axis component of grid-side current, respectively.

In chapter 4, a centralized P-DBPC which controls the whole system by manipulating the power flow is proposed. It treats the front-end converter and the SRM converter as a whole, and the speed of SRM is controlled by manipulating the active power flowing inside the system. Specifically, the output of the speed controller of the back-end SRM is torque reference T^*, and the active power reference P^* is obtained by multiplying T^* by the angular velocity ω_r. P^* is the desired active power required by the motor side, and it is directly provided by the front-end VSR through the instantaneous active power control of P-DBPC. In this way, a direct connection of power between the front-end VSR and back-end SRM is built and one control scheme is enough to realize SRM regulation, grid-side power factor correction, and current har-

monics restraint simultaneously. Therefore, the proposed drive system is more simplified than the aforementioned SRM systems with separate control units. Besides, the energy feedback, which is beneficial to the motor drive system, can be realized in the proposed drive system so that the excess active power can be transferred back to the grid. Additionally, without causing burden on the controller, the A-SVPWM reduces the switching loss by reducing the frequency of switching action, thereby improving the system efficiency.

In chapter 5, a cascade-free MP-DPC strategy is proposed to further remove the conventional cascade control structure from the SRM drive system. Considering the fast dynamic response and flexible integration of various constraints, MPC is adopted to remove the outer speed controller. However, since the conventional MPC is generally adopted as an inner controller of the outer PI control loop, a new cost function is designed in the proposed strategy to eliminate the outer PI control loop. By evaluating the new cost function, the proposed strategy selects the vector which not only will generate a motor speed closer to the setpoint at instant k+2, but will generate an active power capable of further reducing that speed error for the future instant. Consequently, well-regulated motor speed, balanced capacitor voltage, and controllable power flow can be achieved within one cost function simultaneously. Besides, to increase the robustness of the proposed strategy, the disturbances caused by mismatched parameters are estimated via Kalman filter and used to correct the power expressions, thus compensating for the steady-state power error.

The effectiveness of the proposed control strategies have been verified on the testbench, and satisfying control performances have been obtained. In experiments, stable SRM speed can be obtained, the grid-side power factor has been increased to near 1, and the current distortion has been reduced.

For future work, more research regarding the four-quadrant control of SRM can be done further to improve the system's performance with advanced control algorithms. Besides, to enhance the reliability and availability level of the whole system, more research can be done toward making fault diagnosis and realizing the post-fault operation once the short- or open-circuited switch fault is detected in the grid-side rectifier and SRM converter.

APPENDIX A

List of publications

A.1 Journal papers

- **Y. Tang**, Y. He, F. Wang and R. Kennel, "Voltage-sourced Converter fed High-speed SRM Drive System with Energy Feedback and Near-Unity Power Factor", *Industrial Electronics, IEEE Transactions on*, vol. 69, no. 4, pp. 3460–3470, Apr. 2022.

- **Y. Tang**, Y. He, F. Wang, H. Xie, J. Rodriguez and R. Kennel, "A Drive Topology for High-speed SRM with Bidirectional Energy Flow and Fast Demagnetization Voltage", *Industrial Electronics, IEEE Transactions on*, vol. 68, no. 10, pp. 9242–9253, Oct. 2021.

- **Y. Tang**, F. Wang, G. Lin, J. Rodriguez and R. Kennel, "A Centralized Control Strategy for Grid-connected High-speed Switched Reluctance Motor Drive System with Power Factor Correction", *Energy conversion, IEEE Transactions on*, vol. 36, no. 3, pp. 2163–2171, Sep. 2021.

- **Y. Tang**, Y. He, F. Wang, D. Lee, J. Ahn, and R. Kennel, " Back-EMF-based Sensorless Control System of Hybrid SRM for High-speed Operation", *IET Elect. Power Appl*, vol. 12, no. 6, pp. 867–873, Jul. 2018.

- Y. He, **Y. Tang**, X. Gao, H. Xie, F. Wang, J. Rodriguez, and R. Kennel, " Direct Predictive Voltage Control for Grid-Connected Permanent Magnet Synchronous Generator System", *Industrial Electronics, IEEE Transactions on*, vol. 70, no. 11, pp. 10860-10870, Nov. 2023.

- Y. He, **Y. Tang**, X. Gao, H. Xie, F. Wang, J. Rodriguez, and R. Kennel, " A Cascade-Free Model Predictive Control Scheme for Back-to-Back Converter-Fed PMSM Drive System", *Power Electronics, IEEE Transactions on*, vol. 39, no. 4, pp. 4590-4600, Apr. 2024.

- Y. He,**Y. Tang**, H. Xie, F. Wang, J. Rodriguez, and R. Kennel, " Single-phase H-bridge Rectifier fed High-speed SRM System based on Integrated Power Control", *Energy conversion, IEEE Transactions on*, vol. 38, no. 1, pp. 519 - 529, Mar. 2023.

A.2   Conference papers

- Y. He,**Y. Tang**, Q. Chen, F. Wang, and R. Kennel, "Deadbeat direct power control of voltage- sourced rectifier with reduced switching frequency", in *proc. IEEE ICEMS*, Hamamatsu, Japan, Dec. 2020, pp. 1511-1515.

- Y. He,**Y. Tang**, H. Xie, D. Ke, and F. Wang, "Rotor optimization for two-phase high-speed switched reluctance motor", in *proc. IEEE ECCE Asia*, Singapore, May 2021, pp. 2100-2103.

- Y. He, **Y. Tang**, H. Xie, D. Ke, F. Wang, and R. Kennel, "Power quality improvement for grid-connected high-speed switched reluctance drive system", in *proc. IEEE ECCE Asia*, Singapore, May 2021, pp. 2406-2409.

- Y. He, **Y. Tang**, H. Xie, F. Wang, and R. Kennel, "Weighting-factor-less model predictive direct power control for three-level NPC rectifier", in *proc. IEEE ICEMS*, Hamamatsu, Japan, Dec. 2020, pp. 581-586.

- Y. He, **Y. Tang**, H. Xie, F. Wang, J. Rodriguez, and R. Kennel, "Performance evaluation for an optimized 4/2 high-speed SRM fed by active front-end rectifier", in *proc. IEEE ICEM*, Gothenburg, Sweden, Dec. 2020, pp. 1192-1198.

- Q. Chen, **Y. Tang**, Y. He, P. Stolze, and R. Kennel, "An assessment of finite control set predictive current control with concept of variable switching point or parallel cost function for induction motor", in *proc. IEEE ECCE Europe*, Ghent, Belgium, Oct. 2021, pp. 1-6.

- H. Xie, F. Wang, Y. He,**Y. Tang**, J. Rodriguez, and R. Kennel, "Extended kalman filter based encoderless predictive current control for induction machine drives", in *proc. IEEE ECCE Asia*, Singapore, Jul. 2021, pp. 865-868.

- H. Xie, Q. Chen, **Y. Tang**, R. Kennel, F. Wang, A. Xia, Z. Zhang, and J. Rodriguez, "Sliding-mode MRAS based encoderless predictive torque control for induction machine", in *proc. IEEE ICEMS*, Harbin, China, Aug. 2019, pp. 1-6.

- H. Xie, Q. Xun, **Y. Tang**, F. Wang, J. Rodriguez, and R. Kennel, "Robust parallel predictive torque control with model reference adaptive estimator for IM drives", in *proc. IEEE ICEM*, Gothenburg, Sweden, Dec. 2020, pp. 1219-1224.

- H. Xie, F. Wang, Y. He,**Y. Tang**, J. Rodriguez, and R. Kennel, "Sliding-mode disturbance observer based parallel predictive torque controller for induction machine drives", in *proc. IEEE ECCE Asia*, Singapore, Jul. 2021, pp. 1511-1514.

APPENDIX B

List of symbols and abbreviations

B.1   List of symbols

Motor-side symbols:

i_m	Phase current
r_m	Phase resistor
v_m	Phase voltage
ψ_m	Phase flux linkage
$\psi_{m,ini}$	Pre-existed flux linkage
$\tau_{e,m}$	Electromagnetic torque
$p_{m,em}$	Electromagnetic power
W'_e	Magnetic co-energy
ω_r	Mechanical angular velocity
θ_r	Rotor position
$\theta_{m,on}$	Turn-on position
$\theta_{m,off}$	Turn-off position
$\theta_{m,zero}$	Position when winding current drops to zero
τ_{avg}	Average torque
L_m	Phase inductance
θ_a	Aligned position
θ_u	Unaligned position
$P_{m,w}$	Windage loss
N_s	Number of stator poles

N_r	Number of rotor poles
τ_l	Load torque
J_m	Rotor inertia
B_m	Friction coefficient
$p_{m,em}$	Electromagnetic power
$p_{m,l}$	Load power

Grid-side symbols:

v_{dc}	DC-link voltage
ω_g	Frequency of AC side voltage
R_g	Actual value of grid-side filter resistance
e_g	Grid-side voltage
L_g	Actual value of grid-side filter inductance
$L_{g,no}$	Nominal value of grid-side filter inductance
$R_{g,no}$	Nominal value of grid-side filter resistance
C_1	Upper DC-link capacitor
C_2	Lower DC link capacitor
v_{c1}	Voltage on upper DC-link capacitor
v_{c2}	Voltage on lower DC-link capacitor
Δv	Deviation of neutral voltage
T_s	Control period
p	Instantaneous active power
q	Instantaneous reactive power
i_d	d-axis component of grid-side current
i_q	q-axis component of grid-side current
i_α	α-axis component of grid-side current
i_β	β-axis component of grid-side current
e_α	α-axis component of grid-side voltage
e_β	β-axis component of grid-side voltage
u_α	α-axis component of converter voltage
u_β	β-axis component of converter voltage
$\vec{s}^{opti}$	Optimal switching state
$\vec{s}_n$	nth switching state
P^*	Active power reference
Q^*	Reactive power reference

B.2   List of abbreviations

AC	Alternating Current
AFE	Active Front End
ASHB	Asymmetrical Half-Bridge
Back-EMF	Back-Electromotive Force
CFD	Computational Fluid Dynamics
DAC	Digital-to-Analog Converter
DBR	Diode Bridge Rectifier
DC	Direct Current
DSP	Digital Signal Processor
FEM	Finite Element Method
IGBT	Insulated Gate Bipolar Transistor
IPM	Intelligent Power Module
MPC	Model Predictive Control
MP-DPC	Model Predictive Direct Power Control
P-DBPC	Predictive Deadbeat Power Control
PI	Proportional Integral
PMSM	Permanent Magnet Sychronous Machine
RMS	Root Mean Square
THD	Total Harmonic Distortion
3D	Three-dimension
SPC	Single Pulse Control
SRM	Switched Reluctance Motor
SVPWM	Space Vector Pulse Width Modulation
VSR	Voltage-Sourced Rectifier

APPENDIX C

Specifications of the high-speed SRM

The specifications of the target high-speed SRM are presented in Table C.1.

Table C.1: Specifications of the high-speed SRM

Parameters	Value
Rated torque $(\mathrm{N} \cdot \mathrm{m})$	0.12
Rated speed $(\mathrm{r/min})$	25000
Number of Poles	4 / 2
Stator outer diameter (mm)	70
Stator yoke thickness	6.5
Stator inner diameter (mm)	32
Bore diameter (mm)	31.46
Air-gap (mm)	0.27 / 0.42 / 0.53
Shaft diameter (mm)	8
Stack length (mm)	30
Stator pole arc $(°)$	48
Rotor pole arc $(°)$	100
Number of turns per pole	102
Copper wire diameter (mm)	0.6
Number of parallel branches	2
Phase resistance (Ω)	0.4

APPENDIX D

Load torque observer

The load torque observer based on Kalman filter is described as follows. It can also compensate for other disturbances, such as friction, so that the zero steady-state error of the rotor speed can be guaranteed [111]. The discrete form of motor angular velocity can be written as

$$\omega_r[k] = \frac{T_s}{J_m}(\tau_{e,m}[k-1] - \tau_l[k-1]) + \omega_r[k-1] \tag{D.1}$$

Therefore, the state space model of Kalman filter can be written as

$$\underbrace{\begin{pmatrix} \omega_r[k] \\ \tau_l[k] \end{pmatrix}}_{\boldsymbol{X}_d[k]} = \underbrace{\begin{bmatrix} 1 & -\frac{T_s}{J_m} \\ 0 & 1 \end{bmatrix}}_{\boldsymbol{F}_d} \underbrace{\begin{pmatrix} \omega_r[k-1] \\ \tau_l[k-1] \end{pmatrix}}_{\boldsymbol{X}_d[k-1]} + \underbrace{\begin{bmatrix} \tau_{e,m}[k-1] \\ 0 \end{bmatrix}}_{\boldsymbol{G}_d[k-1]} \underbrace{\frac{T_s}{J_m}}_{\boldsymbol{B}_c[k-1]} + \boldsymbol{W}_d[k] \tag{D.2}$$

$$\underbrace{\omega_r[k]}_{\boldsymbol{Z}_d[k]} = \underbrace{\begin{bmatrix} 1 & 0 \end{bmatrix}}_{\boldsymbol{H}_d} \boldsymbol{X}_d[k] + \boldsymbol{V}_d[k] \tag{D.3}$$

where $\boldsymbol{W}_d[k]$ is the process noise with the covariance matrix $\boldsymbol{Q}_d$: $\boldsymbol{W}_d[k] \sim N(0, \boldsymbol{Q}_d)$, and $\boldsymbol{V}_d[k]$ is measurement noise with the covariance matrix $\boldsymbol{R}_d$: $\boldsymbol{V}_d[k] \sim N(0, \boldsymbol{R}_d)$. Then the predicted (a priori) estimate of state vector can be obtained as below based on the mathematical model

$$\hat{\boldsymbol{X}}_d^-[k] = \boldsymbol{F}_d\hat{\boldsymbol{X}}_d[k-1] + \boldsymbol{G}_d[k-1]\boldsymbol{B}_c[k-1] \tag{D.4}$$

where $\hat{\boldsymbol{X}}_d^-[k]$ represents the priori estimate of state vector $\boldsymbol{X}_d$, and $\hat{\boldsymbol{X}}_d[k-1]$ represents the posteriori estimate of state vector calculated within interval $[k-1, k)$. The accuracy covariance of the priori estimate of state vector is defined, i.e., $\boldsymbol{P}_d^-[k] = E[(\boldsymbol{X}_d[k] - \hat{\boldsymbol{X}}_d^-[k])(\boldsymbol{X}_d[k] - \hat{\boldsymbol{X}}_d^-[k])^T]$ and it can be calculated by

$$\boldsymbol{P}_d^-[k] = \boldsymbol{F}_d\boldsymbol{P}_d[k-1]\boldsymbol{F}_d^T + \boldsymbol{Q}_d \tag{D.5}$$

where $\boldsymbol{P}_d[k-1]$ is the accuracy covariance of the posteriori estimate of state vector obtained in $[k-1, k)$. Then in the correction stage, Kalman gain $\boldsymbol{K}_d[k]$ and the posteriori estimate of state vector $\hat{\boldsymbol{X}}_d[k]$ can be calculated by

$$\boldsymbol{K}_d[k] = \frac{\boldsymbol{P}_d^-[k]\boldsymbol{H}_d^T}{\boldsymbol{H}_d\boldsymbol{P}_d^-[k]\boldsymbol{H}_d^T + \boldsymbol{R}_d} \tag{D.6}$$

$$\hat{\boldsymbol{X}}_d[k] = \hat{\boldsymbol{X}}_d^-[k] + \boldsymbol{K}_d[k](\boldsymbol{Z}_d[k] - \boldsymbol{H}_d\hat{\boldsymbol{X}}_d^-[k]) \tag{D.7}$$

$$\boldsymbol{P}_d[k] = (\boldsymbol{I} - \boldsymbol{K}_d[k]\boldsymbol{H}_a)\boldsymbol{P}_d^-[k] \tag{D.8}$$

where $\boldsymbol{P}_d[k]$ is updated to be used in the next sampling period. Through this process, τ_l can be estimated.

List of Figures

List of Tables

Bibliography

[1] B. Bilgin, J. W. Jiang, and A. Emadi, "Electric motor industry and switched reluctance machines," in *Switched reluctance motor drives*, 1st ed. Boca Raton, FL, USA: CRC, ch. 1, pp. 1-31, 2019.

[2] B. Bilgin, J. Liang, M. V. Terzic, J. Dong, R. Rodriguez, E. Trickett, and A. Emadi, "Modeling and analysis of electric motors: State-of-the-art review," *IEEE Trans. Transp. Electr.*, vol. 5, no. 3, pp. 602–617, Jan. 2019.

[3] A. K. Rana and A. V. R. Teja, "Fast discharging (n+1) switch converter with regenerative flyback operation for n-phase srm drives," *IEEE Trans. Power Electron.*, vol. 37, no. 7, pp. 8359–8368, Feb. 2022.

[4] F. Momen, K. Rahman, and Y. Son, "Electrical propulsion system design of chevrolet bolt battery electric vehicle," *IEEE Trans. Ind. Appl.*, vol. 55, no. 1, pp. 376–384, Jan. 2019.

[5] Z. Song, Z. Dong, W. Wang, S. Liu, and C. Liu, "A novel modulation strategy for asymmetrical six-phase series-winding pmsm based on predictive controller," *IEEE Trans. Ind. Electron.*, vol. 70, no. 6, pp. 5592–5603, Aug. 2023.

[6] B. Bilgin and A. Emadi, "Electric motors in electrified transportation: A step toward achieving a sustainable and highly efficient transportation system," *IEEE Power Electron. Mag.*, vol. 1, no. 2, pp. 10–17, Jun. 2014.

[7] B. Bilgin and A. Sathyan, "Fundamentals of electric machines," in *Advanced Electric Drive Vehicles*, 1st ed. Boca Raton, FL: CRC Press, ch. 5, pp. 107-186, 2014.

[8] A. K. Rana and A. V. Ravi Teja, "A fault-tolerant power converter with multi-switch fault diagnosis and repair capability for 4-phase 8/6 srm drives," *IEEE Trans. Transp. Electr.*, vol. 8, no. 3, pp. 3896–3906, Mar. 2022.

[9] B. Bilgin, P. Magne, P. Malysz, Y. Yang, V. Pantelic, M. Preindl, A. Korobkine, W. Jiang, M. Lawford, and A. Emadi, "Making the case for electrified transportation," *IEEE Trans. Transp. Electr.*, vol. 1, no. 1, pp. 4–17, Jun. 2015.

[10] Y. Yang, B. Bilgin, M. Kasprzak, S. Nalakath, H. Sadek, M. Preindl, J. Cotton, N. Schofield, and A. Emadi, "Thermal management of electric machines," *IET Electr. Sys. in Transp.*, vol. 7, no. 2, pp. 104–116, Jun. 2017.

[11] R. W. Erickson and D. Marksimovic, "Line-commutated rectifiers," in *Fundamentals of Power Electronics*, 1st ed.   NY, USA: Kluwer Academic, ch. 17, pp. 609-632, 2004.

[12] D.-H. Lee, Z.-G. Lee, J. Liang, and J.-W. Ahn, "Single-phase SRM drive with torque ripple reduction and power factor correction," *IEEE Trans. Ind. Appl.*, vol. 43, no. 6, pp. 1578–1587, Nov. 2007.

[13] J. Baek, J.-K. Kim, J.-B. Lee, M.-H. Park, and G.-W. Moon, "A new standby structure integrated with boost pfc converter for server power supply," *IEEE Trans. Power Electron.*, vol. 34, no. 6, pp. 5283–5293, Jun. 2019.

[14] R. P. Torrico-Bascopé, D. S. Oliveira, C. G. C. Branco, and F. L. M. Antunes, "A ups with 110-v/220-v input voltage and high-frequency transformer isolation," *IEEE Trans. Ind. Electron.*, vol. 55, no. 8, pp. 2984–2996, Aug. 2008.

[15] H. Wu, S.-C. Wong, C. K. Tse, and Q. Chen, "A pfc single-coupled-inductor multiple-output led driver without electrolytic capacitor," *IEEE Trans. Power Electron.*, vol. 34, no. 2, pp. 1709–1725, Feb. 2019.

[16] X. Lin, J. Luo, and S. Ding, "New single-phase bridgeless high-voltage-gain sepic pfc converters with improved efficiency," in *Proc. IEEE ICCS*, Chengdu, China, Feb. 2021, pp. 225–230.

[17] R. Pandey and B. Singh, "A power-factor-corrected llc resonant converter for electric vehicle charger using cuk converter," *IEEE Trans. Ind. Appl.*, vol. 55, no. 6, pp. 6278–6286, Aug. 2019.

[18] M. Mohamadi, A. Rashidi, S. M. S. Nejad, and M. Ebrahimi, "A switched reluctance motor drive based on quasi Z-source converter with voltage regulation and power factor correction," *IEEE Trans. Ind. Electron.*, vol. 65, no. 10, pp. 8330–8339, Oct. 2018.

[19] M. Rajesh and B. Singh, "Analysis, design and control of single-phase three-level power factor correction rectifier fed switched reluctance motor drive," *IET power Electron.*, vol. 7, no. 6, pp. 1499–1508, Feb. 2014.

[20] J.-Y. Chai and C.-M. Liaw, "Development of a switched-reluctance motor drive with PFC front end," *IEEE Trans. Energy Convers.*, vol. 24, no. 1, pp. 30–42, Mar. 2009.

[21] B. Singh, B. Singh, A. Chandra, K. Al-Haddad, A. Pandey, and D. Kothari, "A review of three-phase improved power quality ac-dc converters," *IEEE Trans. Ind. Electron.*, vol. 51, no. 3, pp. 641–660, Jun. 2004.

[22] R. L. Alves and I. Barbi, "Analysis and implementation of a hybrid high-power-factor three-phase unidirectional rectifier," *IEEE Trans. Power Electron.*, vol. 24, no. 3, pp. 632–640, Mar. 2009.

[23] D. V. Ghodke, K. Chatterjee, and B. G. Fernandes, "Three-phase three level, soft switched, phase shifted pwm dc–dc converter for high power applications," *IEEE Trans. Power Electron.*, vol. 23, no. 3, pp. 1214–1227, May 2008.

[24] A. Prasad, P. Ziogas, and S. Manias, "An active power factor correction technique for three-phase diode rectifiers," *IEEE Trans. Power Electron.*, vol. 6, no. 1, pp. 83–92, Jan. 1991.

[25] J.-Y. Chai, Y.-C. Chang, and C.-M. Liaw, "On the switched-reluctance motor drive with three-phase single-switch switch-mode rectifier front-end," *IEEE Trans. Power Electron.*, vol. 25, no. 5, pp. 1135–1148, May 2010.

[26] A. Anand and B. Singh, "Pfc based bridgeless cuk converter for srm drive," in *Proc. IEEMA Engineer Infinite Conference*, New Delhi, India, Jun. 2018, pp. 1–8.

[27] A. Anand and B. Singh, "Modified dual output cuk converter-fed switched reluctance motor drive with power factor correction," *IEEE Trans. Power Electron.*, vol. 34, no. 1, pp. 624–635, Jan. 2019.

[28] A. Anand and B. Singh, "Power factor correction in cuk–sepic-based dual-output-converter-fed srm drive," *IEEE Trans. Ind. Electron.*, vol. 65, no. 2, pp. 1117–1127, Feb. 2018.

[29] M. Changizian, S. Rezazade, A. Saleki, and M. T. Bina, "Application of Vienna converter to a double-driven SRMs under one PFC compensator," in *Proc. IEEE PEDSTC*, Tehran, Iran, Feb. 2018, pp. 294–299.

[30] E. Şehirli, F. E. Kuyumcu, and B. Çakır, "Current controlled srm fed by three-phase voltage source converter," in *Proc. IEEE UPEC*, Stoke on Trent, UK, Dec. 2015, pp. 1–6.

[31] V. Sharma, B. Singh, and S. Murthy, "Performance analysis of unity power factor converter-inverter fed switched reluctance motor drive," in *Proc. IEEE Int. Electr. Mach. Drives Conf.*, Milwaukee, USA, Aug. 1997, pp. WA1/5.1–WA1/5.3.

[32] B. Bilgin, J. W. Jiang, and A. Emadi, "Operational principles and modeling of switched reluctance machines," in *Switched reluctance motor drives*, 1st ed.   Boca Raton, FL, USA: CRC, ch. 4, pp. 124-181, 2019.

[33] A. Jain and N. Mohan, "Srm power converter for operation with high demagnetization voltage," *IEEE Trans. Ind. Appl.*, vol. 41, no. 5, pp. 1224–1231, Sep. 2005.

[34] F. Peng, J. Ye, and A. Emadi, "An asymmetric three-level neutral point diode clamped converter for switched reluctance motor drives," *IEEE Trans. Power Electron.*, vol. 32, no. 11, pp. 8618–8631, Nov. 2017.

[35] B. Bilgin, J. W. Jiang, and A. Emadi, "Control of switched reluctance machines," in *Switched reluctance motor drives*, 1st ed.   Boca Raton, FL, USA: CRC, ch. 9, pp. 371-424, 2019.

[36] J.-Y. Lim, Y.-C. Jung, S.-Y. Kim, and J.-C. Kim, "Single phase switched reluctance motor for vacuum cleaner," in *Proc. IEEE ISIE*, Pusan, South Korea, Jun. 2001, pp. 1393–1400.

[37] S. Xu, D. Li, G. Deng, and G. Chen, "A single-phase switched reluctance motor drive system," in *Proc. IEEE PEAC*, Wuhan, China, Jan. 2012, pp. 264–267.

[38] J. Oyama, T. Higuchi, T. Abe, and K. Tanaka, "The fundamental characteristics of novel switched reluctance motor with segment core embedded in aluminum rotor block," in *Proc. Int. Conf. Electr. Mach. Sys.*, Nanjing, China, Sep. 2005, pp. 515–519.

[39] J. D. Widmer and B. C. Mecrow, "Optimized segmental rotor switched reluctance machines with a greater number of rotor segments than stator slots," *IEEE Trans. Ind. Appl.*, vol. 49, no. 4, pp. 1491–1498, Jul. 2013.

[40] Z. Xu, D.-H. Lee, and J.-W. Ahn, "Design and operation characteristics of a novel switched reluctance motor with a segmental rotor," *IEEE Trans. Ind. Appl.*, vol. 52, no. 3, pp. 2564–2572, May 2016.

[41] S. R. Mousavi-Aghdam, M. R. Feyzi, N. Bianchi, and M. Morandin, "Design and analysis of a novel high-torque stator-segmented srm," *IEEE Trans. Ind. Electron.*, vol. 63, no. 3, pp. 1458–1466, Mar. 2016.

[42] P. Trung Hieu, D.-H. Lee, and J.-W. Ahn, "Design and control of a high speed segmental stator 4/3 switched reluctane motor," in *Proc. IEEE ITEC Asia-Pacific*, Busan, South Korea, Jun. 2016, pp. 767–772.

[43] Z. Xu, D.-H. Lee, and J.-W. Ahn, "Characteristics analysis of a novel two-phase srm with t-type rotor pole surface," in *Proc. IEEE ICIT*, Busan, Korea, Mar. 2014, pp. 853–857.

[44] P. T. Hieu, D.-H. Lee, and J.-W. Ahn, "Design of a high speed 4/2 switched reluctance motor for blender application," in *Proc. IEEE ITEC Asia-Pacific*, Harbin, China, Aug. 2017, pp. 1–5.

[45] D.-H. Lee, T. H. Pham, and J.-W. Ahn, "Design and operation characteristics of four-two pole high-speed SRM for torque ripple reduction," *IEEE Trans. Ind. Electron.*, vol. 60, no. 9, pp. 3637–3643, Sep. 2013.

[46] S. H. Won, J. Choi, and J. Lee, "Windage loss reduction of high-speed SRM using rotor magnetic saturation," *IEEE Trans. Magn.*, vol. 44, no. 11, pp. 4147–4150, Nov. 2008.

[47] J. Dang, J. Rhett Mayor, S. A. Semidey, R. G. Harley, T. G. Habetler, and J. A. Restrepo, "Practical considerations for the design and construction of a high-speed srm with a flux-bridge rotor," *IEEE Trans. Ind. Appl.*, vol. 51, no. 6, pp. 4515–4520, Nov. 2015.

[48] C. Gong, S. Li, and T. Habetler, "High-strength rotor design for ultra-high speed switched reluctance machines," *IEEE Trans. Ind. Appl.*, vol. 56, no. 2, pp. 1432–1442, Mar. 2020.

[49] R. Hamdy, J. Fletcher, B. Williams, and S. Finney, "High-speed performance improvements of a two-phase switched reluctance machine utilizing rotor-conducting screens," *IEEE Trans. Energy Convers.*, vol. 17, no. 4, pp. 500–506, Dec. 2002.

[50] K. Kiyota, T. Kakishima, and A. Chiba, "Estimation and comparison of the windage loss of a 60 kw switched reluctance motor for hybrid electric vehicles," in *Proc. IEEE ECCE ASIA)*, Hiroshima, Japan, May 2014, pp. 3513–3518.

[51] K. Kiyota, T. Kakishima, A. Chiba, and M. A. Rahman, "Cylindrical rotor design for acoustic noise and windage loss reduction in switched reluctance motor for hev applications," *IEEE Trans. Ind. Appl.*, vol. 52, no. 1, pp. 154–162, Jan. 2016.

[52] S. Calverley, G. Jewell, and R. Saunders, "Aerodynamic losses in switched reluctance machines," *IET Electr. Power Appl.*, vol. 147, no. 6, pp. 443–448, Nov. 2000.

[53] T. Wildi, "Harmonic," in *Electrical machines, drives and power systems*, 5th ed.   Upper Saddle River, NJ, USA: Prentice Hall, ch. 30, pp. 799-808, 2002.

[54] T. Wildi, "Fundamental elements of power electronics," in *Electrical machines, drives and power systems*, 5th ed.   Upper Saddle River, NJ, USA: Prentice Hall, ch. 7, pp. 134-144, 2002.

[55] R. Krishnan, S.-Y. Park, and K. Ha, "Theory and operation of a four-quadrant switched reluctance motor drive with a single controllable switch-the lowest cost four-quadrant brushless motor drive," *IEEE Trans. Ind. Appl.*, vol. 41, no. 4, pp. 1047–1055, Jul. 2005.

[56] J. Kim, K. Ha, and R. Krishnan, "Single-controllable-switch-based switched reluctance motor drive for low cost, variable-speed applications," *IEEE Trans. Power Electron.*, vol. 27, no. 1, pp. 379–387, Jan. 2012.

[57] Y. Hu, T. Wang, and W. Ding, "Performance evaluation on a novel power converter with minimum number of switches for a six-phase switched reluctance motor," *IEEE Trans. Ind. Electron.*, vol. 66, no. 3, pp. 1693–1702, Mar. 2019.

[58] M. Abd Elmutalab, A. Elrayyah, T. Husain, and Y. Sozer, "Extending the speed range of a switched reluctance motor using a fast demagnetizing technique," *IEEE Trans. Ind. Applicat.*, vol. 54, no. 4, pp. 3294–3304, Jul. 2018.

[59] V. F. Pires, A. Cordeiro, A. J. Pires, J. F. Martins, and H. Chen, "A multilevel topology based on the t-type converter for srm drives," in *Proc. IEEE BEC*, Tallinn, Estonia, Oct. 2018, pp. 1–4.

[60] D.-H. Lee and J.-W. Ahn, "A novel four-level converter and instantaneous switching angle detector for high speed srm drive," *IEEE Trans. Power Electron.*, vol. 22, no. 5, pp. 2034–2041, Sep. 2007.

[61] Y. Dessouky, B. Williams, and J. Fletcher, "A novel power converter with voltage-boosting capacitors for a four-phase srm drive," *IEEE Trans. Ind. Electron.*, vol. 45, no. 5, pp. 815–823, Oct. 1998.

[62] J. Liang, D.-H. Lee, G. Xu, and J.-W. Ahn, "Analysis of passive boost power converter for three-phase sr drive," *IEEE Trans. Ind. Electron.*, vol. 57, no. 9, pp. 2961–2971, Sep. 2010.

[63] A. Yalavarthi and B. Singh, "A single-phase grid interfaced srm driven irrigation pump using vienna rectifier for power quality improvement," in *Proc. IEEE SeFeT*, Hyderabad, India, Aug. 2022, pp. 1–6.

[64] P. Verdelho and G. D. Marques, "DC voltage control and stability analysis of PWM-voltage-type reversible rectifiers," *IEEE Trans. Ind. Electron.*, vol. 45, no. 2, pp. 263–273, Apr. 1998.

[65] W. Hofmann, J. Schlabbach, and W. Just, "Basics of reactive power," in *Reactive power compensation: A practical guide*, 1st ed.   Chichester, West Sussex, U.K.: Wiley, ch. 1, pp. 1-13, 2012.

[66] R. Krishnan, "Principle of operation of the switched reluctance motor," in *Switched reluctance motor drives: modeling, simulation, analysis, design, and applications*, 1st ed. Boca Raton, FL, USA: CRC, ch. 1, pp. 229-294, 2001.

[67] W. Leonhard, "Control of a separately excited DC machine," in *Control of electrical drives*, 3rd ed.   Broadway Frnt, NY, USA: Springer, ch. 7, pp. 77-96, 2001.

[68] J. Cai and Z. Liu, "An unsaturated inductance reconstruction based universal sensorless starting control scheme for SRM drives," *IEEE Trans. Ind. Electron.*, vol. 67, no. 11, pp. 9083–9092, Nov. 2020.

[69] L. Ge, I. Ralev, A. Klein-Hessling, S. Song, and R. W. De Doncker, "A simple reluctance calibration strategy to obtain the flux-linkage characteristics of switched reluctance machines," *IEEE Trans. Power Electron.*, vol. 35, no. 3, pp. 2787–2798, Mar. 2020.

[70] T. Wildi, "Active, reactive, and apparent power," in *Electrical machines, drives and power systems*, 5th ed.   Upper Saddle River, NJ, USA: Prentice Hall, ch. 7, pp. 134-144, 2002.

[71] H.-C. Chang and C.-M. Liaw, "On the front-end converter and its control for a battery powered switched-reluctance motor drive," *IEEE Trans. Power Electron.*, vol. 23, no. 4, pp. 2143–2156, Jul. 2008.

[72] H. Chang and C. Liaw, "Development of a compact switched-reluctance motor drive for ev propulsion with voltage-boosting and pfc charging capabilities," *IEEE Trans. Veh. Technol.*, vol. 58, no. 7, pp. 3198–3215, Sep. 2009.

[73] H.-C. Chang and C.-M. Liaw, "An integrated driving/charging switched reluctance motor drive using three-phase power module," *IEEE Trans. Ind. Electron.*, vol. 58, no. 5, pp. 1763–1775, May 2011.

[74] F. Meng, Z. Yu, Y. Chen, C. Gan, and R. Qu, "Development of switched reluctance motor drives with power factor correction charging function for electric vehicle application," in *Proc. IEEE ICEMS*, Harbin, China, Aug. 2019, pp. 1–6.

[75] Y. Tang, Y. He, F. Wang, G. Lin, J. Rodríguez, and R. Kennel, "A centralized control strategy for grid-connected high-speed switched reluctance motor drive system with power factor correction," *IEEE Trans. Energy Convers.*, vol. 36, no. 3, pp. 2163–2172, Jan. 2021.

[76] A. Aniket and S. Bhim, "Cuk-SEPIC based bridgeless PFC dual output converter fed SRM drive," in *Proc. IEEE IICPE*, Jaipur, India, Oct. 2018, pp. 1–7.

[77] J. Jacob, M. M, and V. V, "Comparison between voltage and current control methods for power factor correction in modified dual output cuk converter-fed switched reluctance motor drive," in *Proc. IEEE PEREA*, Kannur, India, Nov. 2020, pp. 1–6.

[78] Y. Tang, Y. He, F. Wang, H. Xie, J. Rodriguez, and R. Kennel, "A drive topology for high-speed SRM with bidirectional energy flow and fast demagnetization voltage," *IEEE Trans. Ind. Electron.*, pp. 9242 – 9253, Oct. 2020.

[79] R. P. Burgos and E. P. Wiechmann, "Extended voltage swell ride-through capability for PWM voltage-source rectifiers," *IEEE Trans. Ind. Electron.*, vol. 52, no. 4, pp. 1086–1098, Aug. 2005.

[80] F. Peng and J. Lai, "Generalized instantaneous reactive power theory for three-phase power systems," *IEEE Trans. Instrum. Meas.*, vol. 45, no. 1, pp. 293–297, Feb. 1996.

[81] H. Akagi, Y. Kanazawa, and A. Nabae, "Instantaneous reactive power compensators comprising switching devices without energy storage components," *IEEE Trans on Ind. Appl.*, vol. IA-20, no. 3, pp. 625–630, May 1984.

[82] A. Yazdani and R. Iravani, "Space phasors and two-dimensional frames," in *Voltage-sourced converters in power systems: modeling, control, and applications*, 1st ed. Hoboken, NJ, USA: Wiley-IEEE Press, ch. 4, pp. 69-107, 2010.

[83] K.-J. Lee, B.-G. Park, R.-Y. Kim, and D.-S. Hyun, "Robust predictive current controller based on a disturbance estimator in a three-phase grid-connected inverter," *IEEE Trans. Power Electron.*, vol. 27, no. 1, pp. 276–283, Jan. 2012.

[84] A. Nikoobin and R. Haghighi, "Lyapunov-based nonlinear disturbance observer for serial n-link robot manipulators," *J Intell. Robot. Syst.*, vol. 55, no. 2-3, pp. 135–153, 2009.

[85] C. Xia, M. Wang, Z. Song, and T. Liu, "Robust model predictive current control of three-phase voltage source PWM rectifier with online disturbance observation," *IEEE Trans. Ind. Inf.*, vol. 8, no. 3, pp. 459–471, Aug. 2012.

[86] L. Yan, F. Wang, M. Dou, Z. Zhang, R. Kennel, and J. Rodriguez, "Active disturbance-rejection-based speed control in model predictive control for induction machines," *IEEE Trans. Ind. Electron.*, vol. 67, no. 4, pp. 2574–2584, Apr. 2020.

[87] L. Harnefors, S. E. Saarakkala, and M. Hinkkanen, "Speed control of electrical drives using classical control methods," *IEEE Trans. Ind. Appl.*, vol. 49, no. 2, pp. 889–898, Mar. 2013.

[88] X. Wang, K. Huang, S. Yan, and B. Xu, "Simulation of three-phase voltage source PWM rectifier based on the space vector modulation," in *Proc. IEEE CCDC*, Shandong, China, Jul. 2008, pp. 1881–1884.

[89] B. Chandra, M. Marta, J. A. Suul, and T. M. Undeland, "Understanding of tuning techniques of converter controllers for VSC-HVDC," in *Proc. Nordic Workshop on Power and Ind. Electron.*, Helsinki, Finland, Jun. 2008, pp. 1–8.

[90] M. Norambuena, P. Lezana, and J. Rodriguez, "A method to eliminate steady-state error of model predictive control in power electronics," *IEEE J. Emerg. Sel. Topics Power Electron.*, vol. 7, no. 4, pp. 2525–2530, Dec. 2019.

[91] M. Siami, D. A. Khaburi, A. Abbaszadeh, and J. Rodriguez, "Robustness improvement of predictive current control using prediction error correction for permanent-magnet synchronous machines," *IEEE Trans. Ind. Electron.*, vol. 63, no. 6, pp. 3458–3466, Jun. 2016.

[92] A. Yazdani and R. Iravani, "Back-to-back hvdc conversion system," in *Voltage-sourced converters in power systems: modeling, control, and applications*, 1st ed.   Hoboken, NJ, USA: Wiley-IEEE Press, ch. 12, pp. 69-107, 2010.

[93] I. Jlassi and A. J. M. Cardoso, "Fault-tolerant back-to-back converter for direct-drive PMSG wind turbines using direct torque and power control techniques," *IEEE Trans. Power Electron.*, vol. 34, no. 11, pp. 11 215–11 227, Nov. 2019.

[94] S. Vazquez, J. A. Sanchez, J. M. Carrasco, J. I. Leon, and E. Galvan, "A model-based direct power control for three-phase power converters," *IEEE Trans. Ind. Electron.*, vol. 55, no. 4, pp. 1647–1657, Apr. 2008.

[95] V. Yaramasu and B. Wu, "Basics of wind energy conversion systems," in *Model predictive control of wind energy conversion systems*, 1st ed.   Hoboken, NJ, USA: Wiley-IEEE Press, ch. 1, pp. 3-58, 2017.

[96] F. Grimm, Z. Zhang, and R. Kennel, "Sphere decoding based long-horizon predictive control of three-level npc back-to-back pmsg wind turbine systems," in *proc. IEEE ECCE-Asia*, Niigata, Japan, May 2018, pp. 2895–2900.

[97] T. Geyer, "Predictive control with long horizons," in *Model predictive control of high power converters and industrial drives*, 1st ed.   Chichester, West Sussex, UK: Wiley & Sons, ch. 5, pp. 195-216, 2016.

[98] F. Grimm, P. Kolahian, R. Bucknall, and M. Baghdadi, "Variable switching point model predictive control for dc-link voltage regulation of back-to-back converters," *IEEE Trans. Ind. Applicat.*, vol. 58, no. 2, pp. 2301–2311, Mar. 2022.

[99] I. Jlassi and A. J. Marques Cardoso, "Enhanced and computationally efficient model predictive flux and power control of PMSG drives for wind turbine applications," *IEEE Trans. Ind. Electron.*, vol. 68, no. 8, pp. 6574–6583, Aug. 2021.

[100] J. Rodriguez, J. Pontt, P. Correa, P. Lezana, and P. Cortes, "Predictive power control of an ac/dc/ac converter," in *Proc. IEEE Fourtieth IAS Annual Meeting*, Hong Kong, China, Oct. 2005, pp. 934–939.

[101] X. Liu, D. Wang, and Z. Peng, "Cascade-free fuzzy finite-control-set model predictive control for nested neutral point-clamped converters with low switching frequency," *IEEE Trans. Contr. Sys. Technol.*, vol. 27, no. 5, pp. 2237–2244, Sep. 2019.

[102] M. Liu, K. W. Chan, J. Hu, W. Xu, and J. Rodriguez, "Model predictive direct speed control with torque oscillation reduction for PMSG drives," *IEEE Trans. Ind. Inform.*, vol. 15, no. 9, pp. 4944–4956, Sep. 2019.

[103] D. E. Quevedo, R. P. Aguilera, M. A. Perez, P. Cortes, and R. Lizana, "Model predictive control of an afe rectifier with dynamic references," *IEEE Trans. Power Electron.*, vol. 27, no. 7, pp. 3128–3136, Jul. 2012.

[104] Z. Zhang, F. Wang, T. Sun, J. Rodríguez, and R. Kennel, "Fpga-based experimental investigation of a quasi-centralized model predictive control for back-to-back converters," *IEEE Trans. Power Electron.*, vol. 31, no. 1, pp. 662–674, Jan. 2016.

[105] J.-Z. Zhang, T. Sun, F. Wang, J. Rodríguez, and R. Kennel, "A computationally efficient quasi-centralized DMPC for back-to-back converter PMSG wind turbine systems without DC-link tracking errors," *IEEE Trans. Ind. Electron.*, vol. 63, no. 10, pp. 6160–6171, Oct. 2016.

[106] D. G. Holmes and T. A. Lipo, "Zero space vector placement modulation strategies," in *Pulse Width Modulation for Power Converters: Principles and Practice*, 1st ed. NJ, USA: Wiley-IEEE Press, ch. 6, pp. 259–270, 2012.

[107] J. Rodríguez and P. C. Estay, "Delay compensation," in *Predictive control of power converters and electrical drives*, 1st ed. Chichester, West Sussex, UK: Wiley-IEEE Press, ch. 12, pp. 166-167, 2012.

[108] T. Wildi, "Electronic control of alternating current motors," in *Electrical machines, drives and power systems*, 5th ed. Upper Saddle River, NJ, USA: Prentice Hall, ch. 23, pp. 134-144, 2002.

[109] J. Rodríguez, R. M. Kennel, J. R. Espinoza, M. Trincado, C. A. Silva, and C. A. Rojas, "High-performance control strategies for electrical drives: An experimental assessment," *IEEE Trans. Ind. Electron.*, vol. 59, no. 2, pp. 812–820, Feb. 2012.

[110] T. J. Miller, "Applications," in *Electronic control of switched reluctance machines*, 1st ed. Oxford, UK: Newnes: Clarendon Press, ch. 9, pp. 201-226, 2001.

[111] Z. Zheng, Y. Li, F. Maurice, and X. Xiao, "A rotor speed and load torque observer for pmsm based on extended kalman filter," in *Proc. IEEE ICIT*, Mumbai, India, Dec. 2006, pp. 233–238.